

VOLUME 12

NUMBER 1

2021

ISSN 2218-7987  
eISSN 2409-5508

International Journal of  
**Mathematics**  
and **Physics**



Al-Farabi Kazakh National University

---

The International Journal of Mathematics and Physics is a peer-reviewed international journal covering all branches of mathematics and physics. The Journal welcomes papers on modern problems of mathematics and physics, in particular, Applied Mathematics, Algebra, Mathematical Analysis, Differential Equations, Mechanics, Informatics, Mathematical Modeling, Applied Physics, Radio Physics, Thermophysics, Nuclear Physics, Nanotechnology, and etc.

---

International Journal of Mathematics and Physics is published twice a year by al-Farabi Kazakh National University, 71 al-Farabi ave., 050040, Almaty, Kazakhstan  
website: <http://ijmph.kaznu.kz/>

Any inquiry for subscriptions should be send to:  
Prof. Tlekkabul Ramazanov, al-Farabi Kazakh National University  
71 al-Farabi ave., 050040, Almaty, Kazakhstan  
e-mail: [Tlekkabul.Ramazanov@kaznu.kz](mailto:Tlekkabul.Ramazanov@kaznu.kz)

For non-compliance with the principles of scientific ethics retracted from:  
● Volume 11, issue 1, p.51-57 (2020) - article of M. Gorokhovski, «Application of overfire air technology for reduction of harmful emissions».

## EDITORIAL

The most significant scientific achievements are attained through joint efforts of different sciences, mathematics and physics are among them. Therefore, publication of the Journal, which shows results of current investigations in the field of mathematics and physics, will allow wider exhibition of scientific problems, tasks and discoveries. One of the basic goals of the Journal is to promote extensive exchange of information between scientists from all over the world. We propose publishing service for original papers and materials of Mathematical and Physical Conferences (by selection) held in different countries and in the Republic of Kazakhstan. Creation of the special International Journal of Mathematics and Physics is of great importance because a vast amount of scientists is willing to publish their articles and it will help to widen the geography of future dissemination. We will also be glad to publish papers of scientists from all the continents.

The Journal will publish experimental and theoretical investigations on Mathematics, Physical Technology and Physics. Among the subject emphasized are modern problems of Applied Mathematics, Algebra, Mathematical Analysis, Differential Equations, Mechanics, Informatics, Mathematical Modeling, Astronomy, Space Research, Theoretical Physics, Plasma Physics, Chemical Physics, Radio Physics, Thermophysics, Nuclear Physics, Nanotechnology, etc.

The Journal is issued on the base of al-Farabi Kazakh National University. Leading scientists from different countries of the world agreed to join the Editorial Board of the Journal. The Journal is published twice a year by al-Farabi Kazakh National University. We hope to receive papers from many laboratories, which are interested in applications of the scientific principles of mathematics and physics and are carrying out researches on such subjects as production of new materials or technological problems.

This issue of the journal is dedicated to the 70th anniversary of the birth and 45th anniversary of the scientific and pedagogical activity of the famous scientist, teacher, organizer of science and education of the Republic of Kazakhstan, doctor of physical and mathematical sciences, professor, member of the National Engineering Academy of the Republic of Kazakhstan, corresponding member of the International Engineering Academy Kaltaev Aydarkhan Zhusipbekovich. The direction of his scientific activity is the mechanics of liquid and gas, physicochemical fluid dynamics, namely, the study of the regularities of the propagation of subsonic flame in complex areas, the study of the mechanism of the transition from conventional combustion to detonation, modeling of hydrogen combustion in a supersonic flow. He and his students also conduct research on the development of methods for calculating turbulent reacting currents, on the receipt and storage of solar thermal energy, and on the development of digital technologies for managing uranium mining using the underground leaching method. Most of his research was carried out in close collaboration with foreign professors - Payman Givi (University of Pittsburgh, USA), A. Wojtanowicz (Louisiana State University, USA), Nagy S. (AGH-University of Science and Technology, Krakow), M. Panfilov and Jean-Jacques Royer (University of Lorraine, Nancy), C. Josserand (University of Marie and Pierre Curie, Paris), K.Ng (National University of Singapore), S. Jayaraj (National Institute of Technology Calicut, India), M. Mohanraji (Hindusthan College of Engineering and Technology), B. Saha (Kyushu University, Japan).

Scientific conference-seminar «Applied Mathematics and Mechanics» dedicated to the 70-th anniversary of professor Kaltaev Aydarkhan took place on December 18, 2020. The issue of the journal contains selected scientific reports of this scientific conference-seminar like the reports of Professor Peyman Givi from the University of Pittsburgh (USA) and Professor Jayaraj Simon from the National Institute of Technology Calicut (India).

Peyman Givi

Mechanical and Petroleum Engineering  
Center for Research Computing  
University of Pittsburgh  
Pittsburgh, PA 15261, USA,  
e-mail: peg10@pitt.edu

### Computational turbulent combustion in the age of artificial intelligence and quantum information

**Abstract.** The impact of high-performance computing on the society has been enormous, but it is easy to be taken for granted. In today's world, it is virtually impossible to imagine system design or major decision making not aided via predictive modeling and simulation. Now that we are experiencing the *Data Revolution* and the emergence of the *Second Quantum Revolution*, it is wise to consider both of these elements in computational science and engineering. Data-driven modeling approaches and demonstrated speed-ups of quantum algorithms have the potential to transform scientific discovery. This will affect the fabrics of industrialized societies in diverse disciplines. A research arena which can substantially benefit from these technologies is combustion. This field has been the subject of heavy computational research for many decades now. In this review, some examples taken from the previous works of the author are presented to demonstrate how the field of computational turbulent combustion is benefiting from modern developments in machine learning (ML) and quantum computing (QC).

**Key words:** computational turbulent combustion, computational science and engineering, speed-ups of quantum algorithms, machine learning, quantum computing.

#### Introduction

Computer modeling and numerical simulation have been rapidly growing in importance throughout the sciences, engineering, medicine as well as in most other disciplines. We are now in an era where, increasingly, experimental and computational researchers are teaming up to tackle grand challenge problems. For over two decades the case has been made for recognizing computational science and engineering (CSE) as a priority interdisciplinary area for funding agencies, and to expand and strengthen the education in its related disciplines [1–3]. We are also in the midst of experiencing both the *Big Data Revolution* [4], and the emergence of the *Second Quantum Revolution* [5]. The amount of data available is doubling yearly, and artificial intelligence (AI), in particular machine learning (ML) methods are playing an increasingly important role in analyzing this data and using it to deduce new models of processes. Moreover, quantum mechanical phenomena have evolved into many core technologies and are expected to be responsible for many of the key advances of the future. Quantum computing (QC), in particular, has the potential to revolutionize computer modeling and simulation. The importance of these fields to the global economy

and security are well recognized, promoting an even more rapid growth of the related technologies in the upcoming decades. This growth is fueled by large investments by many governments and leading industries. An arena in which both QC and AI are promoted to play a more significant role is CSE [2, 3, 6, 7]. Since the early 1980s, computational simulations have been known as the *3rd pillar of science* [8, 9], and are now being augmented by this *4th paradigm* because of the big data revolution [10].

In the arena of computation, now there are some doubts about the longevity of Moore's law [11] which has largely held true for over five decades [12]. As silicon-based processors shrink to smaller and smaller sizes, physical limitations start to play an important role. As a result, the expense and effort required to continue the increase in performance of supercomputers are now much greater than ever before. In order to provide new disruptive means to perform computations with increased complexity, the CSE community will need a radical departure from the conventional classical computing platforms. Quantum computing is a particularly promising candidate to be this disruptive technology for many computational problems [13–23].

The rate of progress in QC technology is very promising. In fact, the rapid development of this

technology has led to what is now known as the “Neven’s law,” stating that: “quantum computers are gaining computational power relative to classical ones at a doubly exponential rate.” The QC community as a whole has an overarching goal to build a general purpose, universal quantum computers [24]. Google, IBM, Intel, Microsoft, and a large and growing number of start-ups in the US and abroad are developing such machines [23]. Quantum computers are increasingly available on the cloud, with commercial offerings from IBM, Microsoft, and Amazon recently being announced. There is also increasing momentum and excitement in the field, with rapid progress in building non-corrected, so called *noisy intermediate scale quantum* (NISQ) computers [19], and the promise of error-corrected machines in the not-too-distant future.

### Applications in Turbulent Combustion

Despite all of the dedicated efforts towards the development of alternative and/or sustainable energy resources, combustion still provides a large portion of the energy needs worldwide, a situation that will likely remain the same within the foreseeable future. Associated with combustion is air pollution and the greenhouse effect; thus the need for the reduction of CO<sub>2</sub> emissions while maintaining high combustion efficiency. These concerns, along with stringent demands to reduce petroleum consumption, are putting a high priority on combustion research. In most cases, combustion is accompanied by turbulence where the latter provides the means of enhanced fuel-air mixing. The physics of turbulent reactive flows is notoriously difficult due to the intricacies of the interactions between chemistry and turbulence. The phenomenon of mixing at both micro and macro scales and its role and capability (or lack thereof) to provide a suitable environment for combustion, and the subsequent effects of combustion on hydrodynamics, have been at the heart of turbulent combustion research for over half a century now [25–27].

Researchers in computational turbulence and combustion are well versed in advanced numerical algorithms, and how to use them effectively in parallel numerical simulations. For over 40 years, the fields of computational turbulent combustion have been one of the most intense fields of CSE [28]. Statistical methods continue to constitute the most practical means of turbulent combustion predictions. These methods involve stochastic representation of the transport equations, augmented with closures to

account for the effects of unresolved scales. Among the variety of stochastic tools developed within the past century, the probability density function (PDF) methods have proven to be particularly effective [29]. This is due to the fundamental property of PDF as it accounts for all of the statistical variations of the transport variable [30–32]. This feature is particularly appealing for modeling of chemically reactive flows, as it accounts for the effects of chemical reactions in an *exact* manner [33–35].

A major challenge in utilizing PDF is associated with its modeling and computational simulations. Combustion engineers have been trying to deal with this issue [36], and there is a continuing need to make use of advanced computational methodologies for turbulent combustion research. In this article, two examples are presented to demonstrate how ML/DL and QC can be useful in this regard. These examples are taken from this previous publications in which this reviewer is a co-author.

#### a. Deep-Learning of Turbulent Scalar Mixing

In this example, detailed in Ref. [37], we consider the problem of mixing of a Fickian passive scalar  $\psi = (t, \mathbf{x})$  ( $t$  denotes time and  $\mathbf{x}$  is the position vector), with diffusion coefficient  $\Gamma$  from an initially symmetric binary state within the bounds  $-1 \leq \psi \leq +1$ . Therefore, the single-point PDF of  $\psi$  at the initial time is  $P_L(0, \psi) = \frac{1}{2}[\delta(\psi - 1) + \delta(\psi + 1)]$ . In homogeneous turbulence, the PDF is governed by [33]  $\frac{\partial P_L}{\partial t} + \frac{\partial(DP_L)}{\partial \psi} = 0$ , where  $D$  denotes the conditional expected diffusion of the scalar field. The closure problem in the PDF transport is associated with this diffusion, and modeling of this term has been a stumbling block since the early days of PDF modeling [33, 34, 38].

Modern ML techniques have the potential to be utilized for PDF model developments [39, 40]. Given data  $\{t^n, \psi^n, P_L^n\}_{n=1}^N$  on time and the PDF, we approximate the functions  $P_L$  and  $D$  by two deep neural networks to obtain the physics-informed neural network  $R := \frac{\partial P_L}{\partial t} + \frac{\partial(DP_L)}{\partial \psi}$  as illustrated in Fig. 1. We obtain the required derivatives to compute the residual network  $R(t, \psi)$  via automatic differentiation [41]. This allows accurate evaluation of derivatives at machine precision with ideal asymptotic efficiency. To assess the performance of this deep learning algorithm, we considered the PDF model obtained by the amplitude mapping closure (AMC) [42–44]. The AMC captures many of the

basic features of the binary mixing problem. Namely, the inverse diffusion of the PDF in the composition domain from a double delta distribution to an asymptotic approximate Gaussian distribution, as the variance goes to zero. Figure 2 depicts the exact [44] and the learned conditional expected diffusion  $D(t, \psi)$ . As demonstrated the agreement is excellent even though the algorithm has seen no data whatsoever on the conditional expected diffusion.

### b. Quantum Computing for Combustion

In this example, detailed in Ref. [45], we demonstrate some potentials of QC for turbulent combustion simulations. We consider the transport of two initially segregated reactants  $F(\mathbf{x}, t)$  and  $O(\mathbf{x}, t)$ , where  $\mathbf{x}-t$  denote the (homogeneous) space-time. An idealized irreversible binary reaction of the type  $F + rO \rightarrow (1+r)Product$  is considered, and turbulent mixing is modelled by the coalescence/dispersion (C/D) closure of Curl [38, 46, 47]. Subsequently, all of the pertinent single-point statistics of the reacting field are determined. The most important of these statistics are the mean rates of reactant conversion, denoted by  $Z(t)$ .

A Monte Carlo (MC) methodology is used for the stochastic simulation of the C/D model. The quantum algorithm is based on quantum phase estimation [48]. Figure 3 shows classical simulations of the quantum algorithm for estimating the rate of mean fuel conversion  $Z_{MC}(t)$ . The increasing behavior of  $Z_{MC}(t)$  as a function of  $t$  is demonstrated in Fig. 3 (a). The results of the quantum algorithm are in agreement with the highly accurate results via classical MC calculations obtained with  $N_r = 2^{20} \times 60$  runs, allowing to obtain estimates  $\tilde{Z}_{MC}(t)$  that are very close to the actual value of  $Z_{MC}(t)$ . The estimated rates of reactant conversion from the quantum algorithm relative to  $\tilde{Z}_{MC}(t)$ , for two values of MC samples ( $N_r$ ), are shown in Fig. 3 (b). The relative errors decrease as a function of time because the  $Z(t)$  approaches 1 as  $t$  increases. Figure 4 shows comparisons of estimation errors from classical MC methods ( $\epsilon_C$ ) and the quantum algorithm ( $\epsilon_Q$ ) as functions of the total number of computational elements ( $N_r$ ). It is observed that  $\epsilon_C$  decreases as  $1/\sqrt{N_r}$  while  $\epsilon_Q$  decreases as  $1/N_r$ , demonstrating a quadratic quantum speedup of the quantum algorithm with respect to the classical methodology. The advantages of the quantum algorithm are more obvious for values of  $N_r$  for which  $\epsilon_Q \leq \epsilon_C$ . However, the genuine advantage is in the different

scaling of the algorithm. This example has substantial applications in practical engineering combustion systems. In the near future, it is expected that the current classical turbulent combustion simulations [49, 50], exemplified by Fig. 5 can benefit from quantum speed-up.

### Concluding Remarks

The emergence and increased importance of massive data sets in many disciplines, coupled with the emergence of ML/DL to analyze these data sets is already transforming the world, and QC has the potential to revolutionize CSE. Data-driven modeling approaches, and demonstrated speed-ups of quantum algorithms have the potential to transform scientific discovery. This will affect the fabrics of industrialized societies in diverse disciplines far beyond science and engineering. The paradigm of scientific discovery offers an elegant path to generalization and enables computing with probability distributions rather than solely relying on deterministic thinking. We have also been witnessing demonstration of quantum speed-up. With emergence of quantum simulators, quantum annealers and analog quantum machines [51–53], and the arrival of universal quantum computers with 50+ qubits, we are now in the era where *quantum supremacy* exists both as a theoretical proposal [54, 55] and experimental realization [56].

Machine learning is currently one of the most popular areas in almost all disciplines. Significant efforts are being devoted to this field, not just in its basic developments, but also in numerous diverse applications. However, it is to be emphasized that ML is not *magic*! It consists of four basic elements: linear algebra, optimization, probability & statistics and algorithms. Machine learning's broad popularity has been, in part, motivated by production of excellent software such as Tensorflow [57]. While ML will surely remain as a powerful research tool, it must be utilized in the context of a very strong physical & mathematical modeling. It is also clear that the era of QC is here and the community is moving towards developments that could potentially have a profound impact on CSE. The challenge lies in understanding the new technology, and identifying the highest-impact applications. As the Nobel Laureate Bill Phillips said: "...Quantum information is a radical departure in information technology, more fundamentally different from current technology than the digital computer is from the abacus..." The computational combustion

community needs to recognize that this is not a short-term endeavor. There is a need to build infrastructure and expertise in this technological frontier of the 21st century.

**Acknowledgements**

I am honored to participate at this meeting in honor of Professor Aidarkhan Kaltayev of Satbayev

University, and I am grateful to him for many technical discussions on the subject matters covered in this review. I am also grateful to my co-authors of previous publications which have been cited here. Our current related work is sponsored by NSF under Grant CBET2042918, and the NASA Transformational Tools and Technologies (TTT) Project under Grant 80NSSC18M0150.

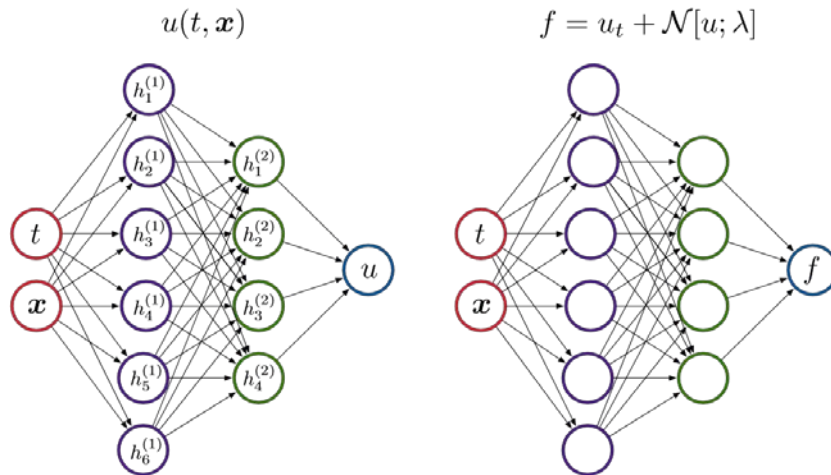


**Figure 1**– *Physics-Informed Neural Network*: The residual neural network  $f$  is obtained by approximating the unknown solution  $u$  by a deep neural network and by taking the required spatial and temporal derivatives using automatic differentiation. Taken from Ref. [37]

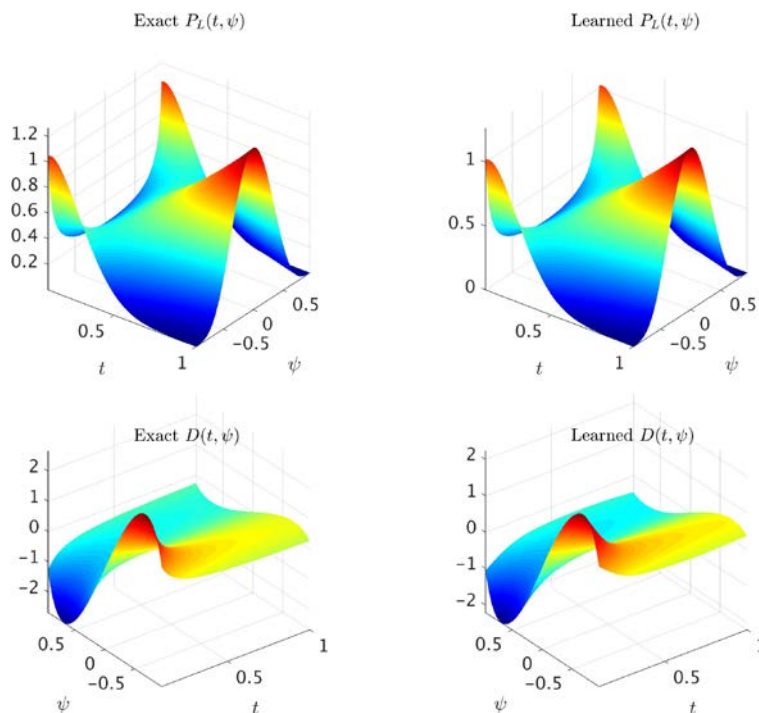


**Figure 2** – The exact  $P_L$  via the exact model and the learned one are on the top, while the exact and learned  $D$ s are in the bottom panels. Taken from Ref. [37].

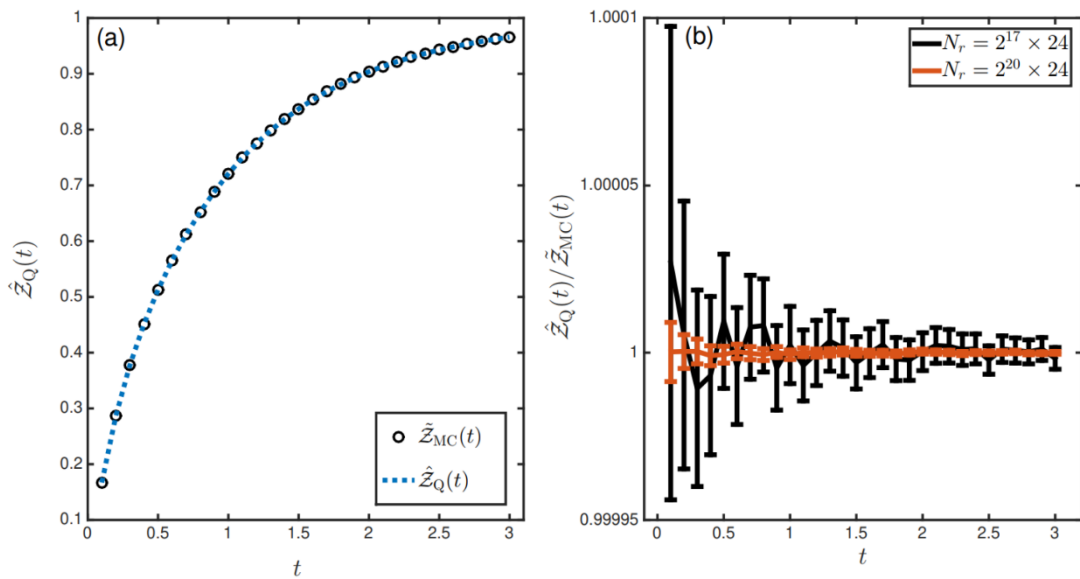


**Figure 3** – Estimates of the rate of reactant conversion obtained from classical simulations of the quantum-algorithm that would solve a reacting flow process using Curl’s model [46].  
 (a) Growth of the estimated rate of reactant conversion as a function of time.  
 (b) Comparison of two estimated rates of reactant conversion for  $N_r = 2^{17} \times 24$  (black line) and  $N_r = 2^{20} \times 24$  (red line), given by the quantum algorithm, with  $\tilde{Z}_{MC}(t)$ . Taken from Ref. [45].

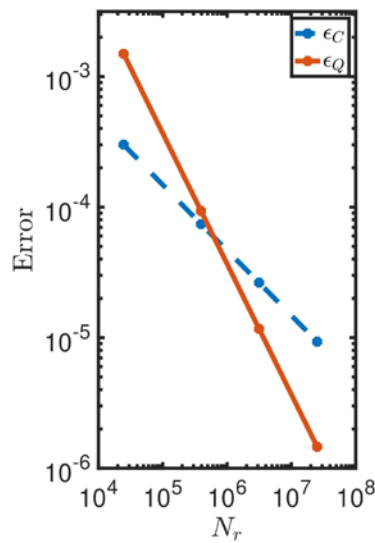


**Figure 4** – Comparisons of errors output by the Classical MC method ( $\epsilon_C$ ) and the Quantum MC algorithm ( $\epsilon_Q$ ). Taken from Ref. [45].

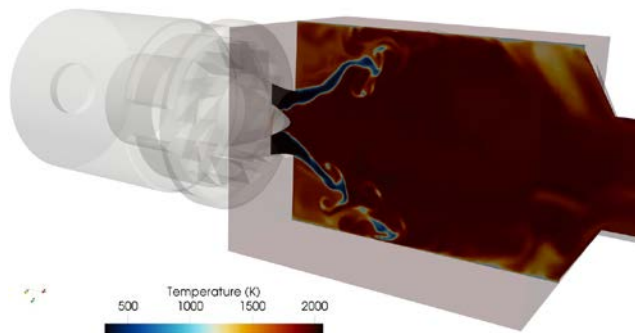


**Figure 5** – Simulation results of the reactor in experiments of Ref. [58].

## References

- 1 SIAM Working Group on CSE Education. "Graduate education in computational science and engineering." *SIAM Review*, 43(1) (2001): 163–177.
- 2 U.S. Department of Energy Advanced Scientific Computing Advisory Committee. ASCAC workforce subcommittee letter. <http://www.netlib.org>, 2014.
- 3 Rude, U., Willcox, K., McInnes, L. C., and Sterck, H. D. "Research and Education in Computational Science and Engineering." *SIAM Review*, 60(3) (2018): 707–754.
- 4 McComb, D. *The Data-Centric Revolution: Restoring Sanity to Enterprise Information Systems*. Technics Publication, Basking Ridge, NJ, 2019.
- 5 Jaeger, L. *The Second Quantum Revolution: From Entanglement to Quantum Computing and Other Super-Technologies*. Springer, Cham, Switzerland, 2019.
- 6 Cramer, C. Quantum testbed stakeholder workshop. Slides [online], [https://science.energy.gov/~/media/ascr/ascac/pdf/meetings/201704/ASCAC\\_QT\\_SW.pdf](https://science.energy.gov/~/media/ascr/ascac/pdf/meetings/201704/ASCAC_QT_SW.pdf), 2017.
- 7 Cho, A. "DOE pushes for useful quantum computing." *Science*, 359(6372) (2018): 141–142.
- 8 Port, O. "Superfast Computers: You ain't seen nothin' yet." *Business Week*, 26:91, 1985.
- 9 Keyes, D. E., McInnes, L. C., Woodward, C., Gropp, W., Myra, E., Pernice, M., Bell, J., Brown, J., Clo, A., Connors, J., Constantinescu, E., Estep, D., Evans, K., Farhat, C., Hakim, A., Hammond, G., Hansen, G., Hill, J., Isaac, T., Jiao, X., Jordan, K., Kaushik, D., Kaxiras, E., Koniges, A., Lee, K., Lott, A., Lu, Q., Magerlein, J., Maxwell, R., McCourt, M., Mehl, M., Pawlowski, R., Randles, A. P., Reynolds, D., Riviere, B., Rude, U., Scheibe, T., Shadid, J., Sheehan, B., Shephard, M., Siegel, A., Smith, B., Tang, X., Wilson, C., and Wohlmuth, B. "Multiphysics simulations: Challenges and opportunities." *The International Journal of High Performance Computing Applications*, 27(1) (2013): 4–83.
- 10 Hey, T., Tansley, S., and Tolle, K. *The Fourth Paradigm: Data-Intensive Scientific Discovery*. Microsoft Research, 2009. ISBN 978-0-9825442-0-4.
- 11 Moore, G. E. "Cramming more components onto integrated circuits." *Electronics*, 38(8) (1965): 1–4.
- 12 Simonite, T. Moore's law is dead. Now what? MIT Technology Review [online], <https://www.technologyreview.com/s/601441/moore-s-law-is-dead-now-what/>, 2016.
- 13 Siegelmann, H. T. "Computation Beyond the Turing Limit." *Science*, 268(5210) (1995): 545–548.
- 14 Lloyd, S. "Universal Quantum Simulators." *Science*, 273(5278):1073–1078, 1996. ISSN 00368075, 10959203. URL <http://www.jstor.org/stable/2899535>.
- 15 Simon, D. R. "On the Power of Quantum Computation." *SIAM J. Computing*, 26(5) (1997): 1474–1483.
- 16 Milburn, G. "Quantum computation: Not the next step, but a whole new journey." *Computing in Science and Engineering*, 3(6) (2001): 87–93.
- 17 Dowling, J. P. and Milburn, G. J. "Quantum technology: the second quantum revolution." *Philosophical Transactions of the Royal Society A: Mathematical, Physical and Engineering Sciences*, 361(1809) (2003): 1655–1674.
- 18 Georgescu, I. M., Ashhab, S., and Nori, F. "Quantum Simulation." *Reviews of Modern Physics*, 86(1) (2014): 153–185.
- 19 Preskill, J. "Quantum Computing in the NISQ era and beyond." *Quantum*, 2:79, 2018. ISSN 2521-327X.
- 20 Albash, T. and Lidar, D. A. "Adiabatic quantum computation." *Reviews of Modern Physics*, 90(1):015002, 2018.
- 21 National Academies of Sciences, Engineering, and Medicine. *Quantum Computing: Progress and Prospects*. The National Academies Press, Washington, DC, 2019. ISBN 978-0-309-47969-1. URL <https://www.nap.edu/catalog/25196/quantum-computing-progress-and-prospects>.
- 22 Martonosi, M. and Roetteler, M. Next steps in quantum computing: Computer science's role. arXiv preprint arXiv:10541, 2019. URL <http://arxiv.org/abs/1903.10541>.
- 23 Givi, P., Daley, A. J., Mavriplis, D., and Malik, M. "Quantum Speedup for Aerospace and Engineering." *AIAA J.*, 58(8):3715–3727, 2020. URL <https://doi.org/10.2514/1.J059183>.
- 24 Mohseni, M., Read, P., Neven, H., Boixo, S., Denchev, V., Babbush, R., Fowler, A., Smelyanskiy, V., and Martinis, J. "Commercialize Quantum Technologies in Five Years." *Nature*, 543(7644) (2017):171–174.
- 25 Hawthorne, W. R., Weddell, D. S., and Hottel, H. C. "Mixing and Combustion in Turbulent Gas Jets." *Third Symposium on Combustion and Flame and Explosion Phenomena*, 3(1) (1948): 266–288.

- 26 Kuo, K. K. and Acharya, R. *Fundamentals of Turbulent and Multiphase Combustion*. John Wiley and Sons Inc., Hoboken, NJ, 2012.
- 27 Pope, S. B. "Small Scales, Many Species and the Manifold Challenges of Turbulent Combustion." *Proc. Combust. Inst.*, 34(1) (2013):1–31. ISSN 1540-7489.
- 28 Givi, P. "Model-Free Simulations of Turbulent Reactive Flows." *Prog. Energ. Combust.*, 15(1) (1989):1–107.
- 29 Lumley, J. L. *Stochastic Tools in Turbulence*. Academic Press, New York, NY, 1970.
- 30 Stratonovich, R. L. *Introduction to the Theory of Random Noise*. Gordon and Breach, New York, NY, 1963.
- 31 Lundgren, T. S. "Distribution Functions in the Statistical Theory of Turbulence." *Phys. Fluids*, 10(5) (1967): 969–975.
- 32 Monin, A. S. and Yaglom, A. M. *Statistical Fluid Mechanics, Vol. 2*. MIT Press, 1975.
- 33 O'Brien, E. E. The Probability Density Function (PDF) Approach to Reacting Turbulent Flows. In Libby, P. and Williams, F., editors, *Turbulent Reacting Flows*, volume 44 of *Topics in Applied Physics*, chapter 5, pages 185–218. Springer Berlin / Heidelberg, Heidelberg, 1980.
- 34 Pope, S. B. "PDF Methods for Turbulent Reactive Flows." *Prog. Energ. Combust.*, 11(2) (1985): 119–192.
- 35 Givi, P. "Filtered Density Function for Subgrid Scale Modeling of Turbulent Combustion." *AIAA J.*, 44 (1) (2006):16–23.
- 36 Sammak, S., Ren, Z., and Givi, P. Modern developments in filtered density function. In Livescu, D., Nouri, A. G., Battaglia, F., and Givi, P., editors, *Modeling and Simulation of Turbulent Mixing and Reaction: For Power, Energy and Flight 8* (2020): 181–200.
- 37 Raissi, M., Babae, H., and Givi, P. "Deep learning of turbulent scalar mixing." *Phys. Rev. Fluids*, 4: 124501, 2019.
- 38 Kosaly, G. and Givi, P. "Modeling of Turbulent Molecular Mixing." *Combust. Flame*, 70(1) (1987): 101–118.
- 39 Raissi, M. and Karniadakis, G. E. "Hidden physics models: Machine learning of nonlinear partial differential equations." *J. Comp. Phys.*, 357 (2018): 125–141.
- 40 Raissi, M., Perdikaris, P., and Karniadakis, G. E. "Numerical Gaussian Processes for Time-Dependent and Nonlinear Partial Differential Equations." *SIAM J. Sci. Computing*, 40(1) (2018): A172–A198.
- 41 Baydin, A. G., Pearlmutter, B. A., Radul, A. A., and Siskind, J. M. Automatic differentiation in machine learning: a survey. arXiv preprint arXiv:1502.05767, 2015.
- 42 Kraichnan, R. H. "Closures for Probability Distributions." *Bull. Amer. Phys. Soc.*, 34:2298, 1989.
- 43 Chen, H., Chen, S., and Kraichnan, R. H. "Probability Distribution of a Stochastically Advected Scalar Field." *Phys. Rev.*, 63(24) (1989): 2657–2660.
- 44 Miller, R. S., Frankel, S. H., Madnia, C. K., and Givi, P. "Johnson-Edgeworth Translation for Probability Modeling of Binary Scalar Mixing in Turbulent Flows." *Combust. Sci. Technol.*, 91 (1993): 21–52.
- 45 Xu, G., Daley, A. J., Givi, P., and Somma, R. D. "Quantum Algorithm for the Computation of the Reactant Conversion Rate in Homogeneous Turbulence." *Combust. Theory & Modelling*, 53(6) (2019): 1090–1104.
- 46 Curl, R. L. "Dispersed Phase Mixing: I. Theory and Effects in Simple Reactors." *AIChE J.*, 9(2) (1963):175–181.
- 47 Pope, S. B. "An Improved Turbulent Mixing Model." *Combust. Sci. Technol.*, 28(3–4) (1982):131–145.
- 48 Knill, E., Ortiz, G., and Somma, R. "Optimal Quantum Measurements of Expectation Values of Observables." *Phys. Rev. A*, 75:012328, 2007.
- 49 Ansari, N., Strakey, P. A., Goldin, G. M., and Givi, P. "Filtered Density Function Simulation of a Realistic Swirled Combustor." *Proc. Combust. Inst.*, 35(2) (2015): 1433–1442.
- 50 Inkarbekov, M., Aitzhan, A., Kaltayev, A., and Sammak, S. "A GPU-Accelerated Filtered Density Function Simulator of Turbulent Reacting Flows." *Int. J. Comp. Fluid Dyn.* 34(6) (2020): 381–396.
- 51 Cirac, J. I. and Zoller, P. "Goals and Opportunities in Quantum Simulation." *Nature Physics*, 8(4) (2012): 264–266.
- 52 Ronnow, T. F., Wang, Z., Job, J., Boixo, S., Isakov, S. V., Wecker, D., Martinis, J. M., Lidar, D. A., and Troyer, M. "Defining and Detecting Quantum Speedup." *Science*, 345 (2014): 420–424.
- 53 Biswas, R., Jiang, Z., Kechezhi, K., Knysh, S., Mandr'a, S., O'Gorman, B., Perdomo-Ortiz, A., Petukhov, A., Realpe-Gomez, J., Rieffel, E., Venturelli, D., Vasko, F., and Wang, Z. "A NASA perspective on quantum computing: Opportunities and challenges." *Parallel Computing*, 64:81–98, 2017. ISSN 01678191. URL

<https://www.sciencedirect.com/science/article/pii/S0167819116301326>. High-End Computing for Next-Generation Scientific Discovery.

54 Preskill, J. Quantum computing and the entanglement frontier. arXiv preprint arXiv:1203.5813v3, 2012.

55 Papageorgiou, A. and Traub, J. F. "Measures of quantum computing speedup." *Physical Review A*, 88(2): 022316, 2013.

56 Arute, F., Arya, K., Babbush, R., Bacon, D., Bardin, J. C., Barends, R., Biswas, R., Boixo, S., Brandao, F. G. S. L., Buell, D. A., Burkett, B., Chen, Y., Chen, Z., Chiaro, B., Collins, R., Courtney, W., Dunsworth, A., Farhi, E., Foxen, B., Fowler, A., Gidney, C., Giustina, M., Graff, R., Guerin, K., Habegger, S., Harrigan, M. P., Hartmann, M. J., Ho, A., Hoffmann, M., Huang, T., Humble, T. S., Isakov, S. V., Jeffrey, E., Jiang, Z., Kafri, D., Kechedzhi, K., Kelly, J., Klimov, P. V., Knysh, S., Korotkov, A., Kostritsa, F., Landhuis, D., Lindmark, M., Lucero, E., Lyakh, D., Mandr'a, S., McClean, J. R., McEwen,

M., Megrant, A., Mi, X., Michielsen, K., Mohseni, M., Mutus, J., Naaman, O., Neeley, M., Neill, C., Niu, M. Y., Ostby, E., Petukhov, A., Platt, J. C., Quintana, C., Rieffel, E. G., Roushan, P., Rubin, N. C., Sank, D., Satzinger, K. J., Smelyanskiy, V., Sung, K. J., Trevithick, M. D., Vainsencher, A., Villalonga, B., White, T., Yao, Z. J., Yeh, P., Zalcman, A., Neven, H., and Martinis, J. M. "Quantum supremacy using a programmable superconducting processor." *Nature*, 574(7779):505–510, 2019. ISSN 1476-4687. URL <https://doi.org/10.1038/s41586-019-1666-5>.

57 Abadi, M., Agarwal, A., Barham, P., Brevdo, E., Chen, Z., Citro, C., Corrado, G. S., Davis, A., Dean, J., Devin, M., et al. "Tensorflow: Large-scale machine learning on heterogeneous distributed systems." *arXiv preprint arXiv:1603.04467*, 2016.

58 Meier, W., Weigand, P., Duan, X. R., and Giezendanner-Thoben, R. "Detailed Characterization of the Dynamics of Thermoacoustic Pulsations in a Lean Premixed Swirl Flame." *Combust. Flame*, 150(1–2) (2007): 2–26.

S. Jayaraj<sup>1\*</sup> , A. James<sup>1</sup>, M. Srinivas<sup>1</sup> and M. Mohanraj<sup>2</sup> 

<sup>1</sup> National Institute of Technology, Kerala, India

<sup>2</sup> Hindustan College of Engineering and Technology, Tamil Nadu, India

\*e-mail: [sjayaraj@nitc.ac.in](mailto:sjayaraj@nitc.ac.in)

## Energy-Efficient Operation of PV-T Solar Collectors with Heat Pump based Water Heaters Suitable for Domestic Applications

**Abstract.** A photovoltaic-thermal (PV-T) hybrid collector evaporator was designed and developed to produce electrical energy and extract thermal energy simultaneously from the panel using the refrigerant circulated the evaporator tubes. The refrigerant absorbs the heat from photovoltaic panels during its phase change from liquid to vapour. The PV-T evaporators deliver both electricity and heat outputs. An R-32 refrigerant-based solar-assisted heat pump water heating system with a rated heat output of 4 kW was developed and tested its performance for producing 150-200 litres of hot water at an average temperature of 60°C. The R-32 refrigerant is selected because it does not have any ozone depletion potential (ODP), and possess very low global warming potential (GWP). The heat pump evaporator was designed to absorb 3.25 kW heat from the panel and maintains the panel below 30°C. The average PV electricity output was 6 kWh, and the requirement was 3.5 kWh. The average excess power of 2.5 kWh has been supplied to the grid, and the average coefficient of performance (COP) of the system was 6.3. For a life span of 25 years, the total equivalent warming impact analysis (TEWI) resulted in a CO<sub>2</sub> value of 15,543 kg, which is very much lower than that of conventional systems. The economic analysis performed was reported, and the system is found to be quite suitable for domestic applications and also economically feasible with a payback period of 2.5 years.

**Key words:** Solar PV-T Collectors, VFD Compressor, Domestic Water Heating.

### Introduction

The present renewable energy market is experiencing a rapid development owing to the sophisticated technologies emerging with higher overall system efficiencies. The widely used renewable energy capturing technology is the solar photovoltaic (PV) cells. But, the commercially available solar PV cells have only a low range of conversion efficiency. In the range of 15-20% and the remaining is getting wasted and contributing to cell temperature increase, conversion efficiency decreases. So, it would be beneficial to the conversion efficiency if we can absorb some portion of the wasted energy through some other technology. The PV technology gained more attention during the last three decades as more and more governmental as well as global environmental policies were evolved and instructed the usage of various renewable energy technologies. Solar PV technology is

considered to be widely infamous because of the smaller conversion efficiency involved. The commercial conversion efficiency range of 15-20% is further reduced, if the panel is intended to work where the ambient temperature is above 25°C. The reduction in cell efficiency is so rapid concerning the temperature increase above this optimum value. The major part of the incoming radiation that is escaping in the form of thermal energy can be extracted for the purpose of drying and water or space heating. This thought paved the way to the invention of such hybrid photovoltaic-thermal (PV-T) collectors. The first PV-T collector technology was introduced in the year 1978 by Kern and Russel [1]. It succeeded in providing a combined output of electrical energy and thermal energy with the space requirement of one system.

Further, the initial theoretical model of air-based and liquid-based PV-T hybrid collectors was developed [2] based on the extended Hottel-

Whillier-Bliss model [3] by considering the PV conversion efficiency as a linear function of PV cell operating temperature. The design considerations of monocrystalline Silicon cell-based PV-T collectors were formulated. The correlation between various design parameters was identified, especially in the effect of glazing and its transmissivity and emissivity values [4]. During the next decade, several studies were reported in combined collectors, and most of them are of hybrid PV-T air collector arrangements. A novel PV-T collector configuration that can spectrally split the incoming radiation using some radiation beam splitters was proposed and performed simulation study with various operating conditions [5]. The electrical output from such a collector system is found reduced than the conventional system, and that reduction is compensated in the thermal output generated. The PV-T hybrid collector technology was developed further using different and more efficient heat transferring fluids and methods. The various configurations can be categorized into six major categories, i.e., air-based PV-T collectors, liquid-based PV-T collectors, nanofluid based PV-T collectors, heat pipe assisted PV-T collectors, phase change material (PCM) based PV-T collectors, and refrigerant-based heat pump PV-T collectors. Numerous significant studies [6]-[19] were reported in the last two decades explaining the developments in these six configurations for overall system efficiency improvement.

As the refrigerant-based heat pump PV-T collector systems have comparatively higher overall system efficiency than the other configurations, most of the further PV-T collector investigations report in that domain [6]-[8]. In the present work, the R-32 refrigerant-based heat pump PV-T collector is working as the evaporator section. The refrigerant flowing through the copper tubes attached to the bottom of the PV panel and extracting the waste heat available after the photoelectric conversion of the incoming radiation and by this extraction the operating temperature of the PV cells reduces efficiency improves. The heat pump rejects the extracted thermal energy at the condenser to the water in the surrounding tank, and thereby the hot water

becomes available for domestic applications. The novelty of this work is the use of a variable frequency drive (VFD) compressor (which works by following the load available at the evaporator exit). The VFD compressor operates in place of a conventional compressor, and thereby increase in energy efficiency is obtained.

### Experimental Setup

Investigations were performed under the meteorological conditions of Calicut (11.25° N, 75.78° E), India. Three 330 W<sub>c</sub> polycrystalline panels were used as the base plant, and a heat pump circuit was designed to absorb 3 kW heat from the PV panels. The R-32 refrigerant is selected as the working fluid since it has no ozone depletion potential (ODP) and the global warming potential is only 650 (it is around 1/3<sup>rd</sup> of R-22). Experiments were performed from 08:00 hrs to 18:00 hrs, and clear sky days were only considered for the analysis.

The schematic representation of the VFD compressor heat pump assisted PV-T hybrid collector-based water heating system is shown in Fig. 1. The heat pump circuit of the experimental system is made up of 3/8" copper tubes, and evaporator circuits are arranged in parallel through the bottom of the three panels. The temperature of the refrigerant available at the evaporator exit is continuously monitoring, and the frequency of the compressor is varying in accordance with that load values. The compressor runs continuously for a few minutes, in the beginning, to develop enough pressure in the refrigerant circuit and then become idle and work only according to the feedback signal. The photograph of the heat pump-based PV-T hybrid collector water heating system installed at the Solar Energy Centre (SEC), National Institute of Technology, Calicut, is shown in Fig. 2.

The temperature and pressure values from the various locations of the heat pump circuit and water tank were continuously monitored using a data logger. The theoretical analyses based on the first and second laws of thermodynamics were performed based on the experimental data obtained for the different testing days [9].

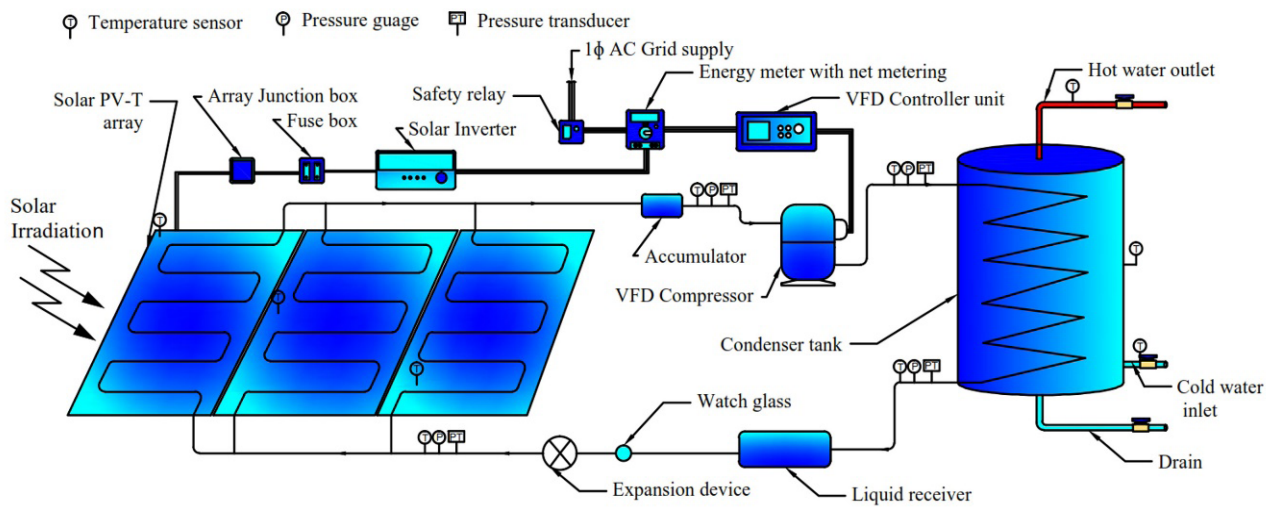


Figure 1 – Schematic representation of the heat pump-based PV-T water heating setup



Figure 2 – Photographic view of the heat pump-based PV-T water heater system installed at the SEC

## Results and Discussions

During the testing days, the solar irradiations varied from  $140 \text{ W/m}^2$  in the morning to the maximum irradiation value of  $770 \text{ W/m}^2$  by noon. Even though it reached  $2 \text{ W/m}^2$  at 17:45 hrs, the variation was almost entirely in a pattern without significant fluctuations.

The ambient temperature and the PV panel temperature are found to vary in accordance with the solar irradiation changes. Ambient temperature variation was from  $28^\circ\text{C}$  to  $34^\circ\text{C}$ . The PV panel temperature of the standard panel kept without cooling is varied from  $30^\circ\text{C}$  to  $65^\circ\text{C}$ , whereas that of panel cooled using heat pump showed a maximum temperature value of

45°C only. The characteristics of the variation of PV temperature with and without cooling according to the variations of solar irradiation and ambient temperature are shown in Fig. 3. The operating temperature of the

PV panel showed a near-linear pattern variation since the waste heat generated is efficiently getting removed by the heat pump circuit integrated to the bottom of the panels.

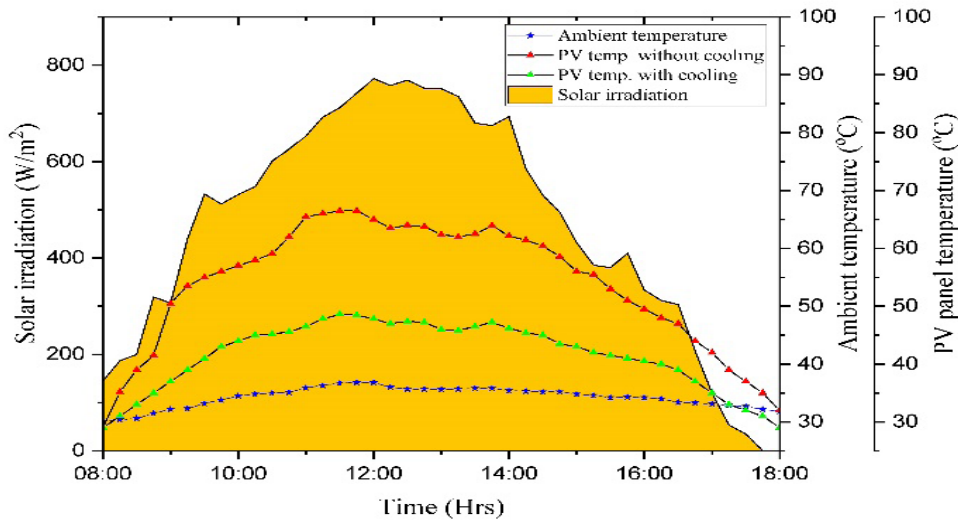


**Figure 3** – Characteristics of PV temperature variation with solar irradiation and ambient temperature

In the case of the electrical power output from the PV panels, the panels integrated with heat pump cooling produce an average of 7.5 kWh of electricity during a clear sky day, and that is around 1 kWh higher than what was available from the standard panel kept without cooling for comparison purpose. That is happened because of the improved conversion efficiency of the PV cells achieved through heat pump-based cooling. The variation in the current and the voltage with and without cooling are shown in Figs. 4 and 5. The current output from the cooled PV panels showed significant improvement than the current made available from the reference PV panel kept without cooling. The voltage values are also showed substantial improvement with heat pump-based cooling. The voltage from the cooling panels is found to be varied from 55 V to 72 V without cooling, and that varied from 58 V to 79 V with the application of the cooling.

Since the operating temperature of the PV cells was able to be kept without much increase, the conversion efficiency of the PV cells also gets increased than that of the reference panel and which results in a significant hike in the electrical power output available from the PV panels. The

characteristics of the electrical power output with and without cooling are shown in Fig. 6. An average improvement of 15% is observed in the total power output. Simultaneously, the input power requirement of the VFD compressor is comparatively lesser than that of the conventional compressor. Thus, the power consumption for the system reduces significantly. So, the VFD compressor integrated heat pump-based cooling contributes enough to the net power output from the system.

The COP of the system was found to be varied between 1.5 and 9 and reported an average value of 6.2 with the refrigerant R-32. The electrical PV efficiency and thermal energy efficiency are increased significantly and reached maximum values of 17% and 80% at some instants of the total experiment duration. The 17% electrical PV efficiency is very nearer to the standard conversion efficiency of the selected PV polycrystalline PV panel. The economic analysis performed also resulted in a payback period of 2.5 years, which is very much lower than that of PV-T water heating systems with conventional compressors. Thus, the developed heat pump cooled hybrid PV-T collector-based water heater is found feasible performance-wise and cost-wise.

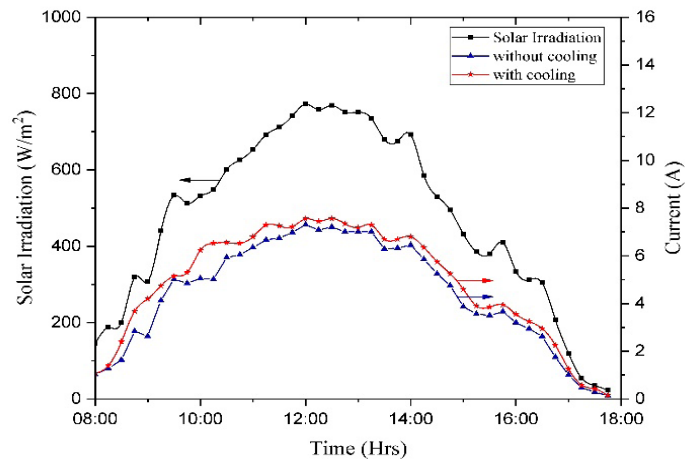


Figure 4 – Variation of current output with and without cooling

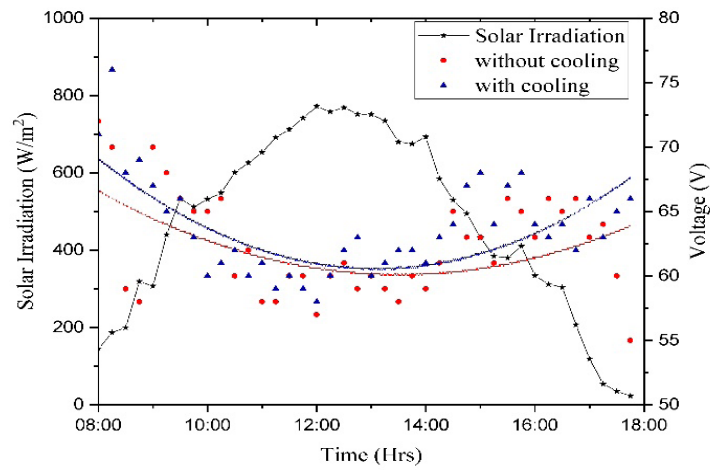


Figure 5 – Variation in the output voltage with and without cooling

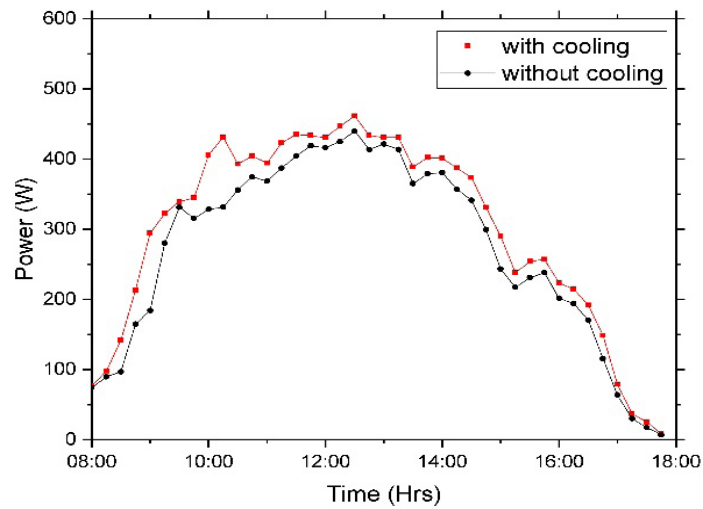


Figure 6 – Characteristics of the electrical power output from the panels with and without cooling

## Prototype Development

The prototype of an ambient source heat pump water heater of 100 l capacity was developed and tested for its performance for residential water heating applications. The ambient source heat pump water heater consists of essential components such as a hermetically sealed compressor of rated power input of 1 kW, immersion type condenser, capillary tube expansion device, and forced convection finned tube evaporator. The ambient source heat pump was charged with R134a. The refrigerant

R134a has a high critical temperature of 106°C. Hence, it is possible to operate the heat pump water heaters using R134a up to 75°C. The photograph of the condenser tank, compressor and other control devices of the prototype developed are shown in Fig. 7. This heat pump water heater consumes 2-3 kWh of electricity to produce 150 liters of hot water at 55°C, which is significantly lower than conventional resistance water heating systems. The payback of the heat pump water heaters is around two years when compared to the electrical resistance water heating systems.



Figure 7 – Photographic view of prototype ambient source heat pump water heater

## Conclusions

The VFD compressor integrated heat pump-based PV-T water heating system was experimented with respect to its electrical, thermal, and overall system efficiency. The integration of a VFD compressor instead of the conventional compressor has reduced the compressor power requirement of the PV-T heat pump water heater system. The average operating temperature of the PV panels is reduced around 22% with heat pump cooling and which contributed to an output power enhancement of 15%. The instantaneous thermal energy efficiency and PV efficiency are improved with cooling by 12% and 28%, respectively. The thermal performance of the system improved

with cooling and reported an average COP of 6.3 for the developed heat pump system with the integration of the VFD compressor. The average PV electricity output was 6 kWh, and the input power requirement for the compressor was 3.5 kWh. Thus, on an average about 2.5 kWh can be supplied back to the utility on a daily basis. If we are developing it as a stand-alone system, with a 1 kW solar power plant and integrated heat pump water heating system, it is technically possible to generate around 3 kWh of PV electricity and around 200 litres of hot water without grid-connected electricity. The system performance can be further improved using zeotropic refrigerant mixtures, as their non-linear behaviour will provide more uniform cooling to the panels. The economic analysis per-

formed, and the system is found to be economically feasible with a payback period of 2.5 years.

### Acknowledgement

This work is part of a Department of Science and Technology, Government of India funded research project titled “Development, testing and standardization of heat pump water heaters using solar photovoltaic-thermal hybrid evaporators” (Ref. No.: DST/TMD/CERI/C47(G)).

### References

- 1 E. C. Kern and M. C. Russell, “221 Makifr, Conf- 7806/7--,” *13th IEEE Photovolt. Spec. Conf.*, no. June, 1978.
- 2 S. D. Hendrie, “Evaluation of combined photovoltaic/thermal collectors,” 1979, no. June, pp. 790541–54.
- 3 L. W. Ft, “Extension of the Hottel-Whillier model to the analysis of combined photovoltaic/thermal flat plate collectors,” 22 (1979): 361–366.
- 4 C. H. Cox and P. Raghuraman, “Design considerations for flat-plate-photovoltaic/thermal collectors,” *Sol. Energy*, vol. 35, no. 3 (1985): 227–241, doi: 10.1016/0038-092X(85)90102-1.
- 5 M. A. Hamdy, F. Luttmann, and D. Osborn, “Model of a spectrally selective decoupled photovoltaic/thermal concentrating system,” *Appl. Energy*, vol. 30, no. 3 ( 1988): 209–225, doi: 10.1016/0306-2619(88)90046-3.
- 6 G. Pei, J. Ji, T. T. Chow, H. He, K. Liu, and H. Yi, “Performance of the photovoltaic solar-assisted heat pump system with and without glass cover in winter: a comparative analysis,” *Proc. Inst. Mech. Eng. Part A J. Power Energy*, vol. 222, no. 2 (2008): 179–187, doi: 10.1243/09576509JPE431.
- 7 J. Ji *et al.*, “Experimental study of photovoltaic solar assisted heat pump system,” *Sol. Energy*, vol. 82, no. 1 (2008): 43–52, doi: 10.1016/j.solener.2007.04.006.
- 8 H. Hu, R. Wang, and G. Fang, “Dynamic characteristics modeling of a hybrid photovoltaic-thermal heat pump system,” *Int. J. Green Energy*, vol. 7, no. 5 (2010): 537–551, doi: 10.1080/15435075.2010.515446.
- 9 S. Jayaraj, A. James, M. Srinivas, and M. Mohanraj, “Experiments on a PVT based hybrid solar collector operated heat pump suitable for space heating in energy efficient buildings,” *ASHRAE 4th International Conference on Efficient Building Design*. October 2020.

B. Elma<sup>1</sup> , E. Misirli<sup>1\*</sup> 

Ege University, İzmir, Turkey  
e-mail: berfin-elma@hotmail.com

## On the physical behaviours of the conformable fractional modified Camassa – Holm equation using two efficient methods

**Abstract.** In recent years, many authors have researched about fractional partial differential equations. Physical phenomena, which arise in engineering and applied science, can be defined more accurately by using FPDEs. Thus, obtaining exact solutions of the FPDEs equations have become more important to understand physical problems. In this article, we have reached the new traveling wave solutions of the conformable fractional modified Camassa – Holm equation via two efficient methods such as first integral method and the functional variable method. The wave transformation and conformable fractional derivative have been used to convert FPDE to the ordinary differential equation. The Camassa – Holm equation is physical model of shallow water waves with non-hydrostatic pressure. Thanks to these powerful methods, some comparisons, such as type of solutions and physical behaviours, have been made. Additionally, mathematica program have been used with the aim of checking of solutions. Investigating results of the fractional differential equations can help understanding complex phenomena in applied mathematics and physics.

**Key words:** Fractional modified Camassa–Holm equation; traveling wave solutions; conformable derivative; the first integral method; the functional variable method.

### Introduction

Fractional derivative models can describe many complex problems in physics and engineering more correctly. Recently, fractional derivatives have been used on applications in many area such as signal processing, nonlinear optics, water wave modeling, control theory and etc [1-3]. There are various derivative definitions such as the Riemann – Liouville derivative [3], the Caputo derivative [4], Jumarie’s modified Riemann – Liouville derivative [5] and the Atangana – Baleanu derivative [6] in literature.

Numerous methods have been applied to obtain different solutions of fractional partial differential equations. Some of them are; the functional variable method [7], the extended tanh function method [8], the first integral method [9], the extended direct algebraic method [10], the modified simple equation method [11], the modified trial equation method [12], the  $(G'/G)$  – expansion method [13], the extended trial equation method [14], the kudryashov method [15] and so on [16-25].

In this article, first integral method [26] and functional variable method [27] have been applied to reach the exact solutions of the conformable fractional modified Camassa – Holm equation arising in fluid dynamics. The time-fractional modified Camassa – Holm equation of the following form [28]:

$$D_t^\alpha u + 2\sigma u_x - u_{xxt} + \beta u^2 u_x = 0 \quad \sigma \in R, \text{ and } 0 < \alpha \leq 1 \quad (1)$$

$D_t^\alpha u$  is express of the conformable fractional derivative of  $u$  with respect to  $t$  of order  $\alpha$  and  $\sigma, \beta$  are non-zero constants.

The rest of article is given as follows: Some definitions and properties of conformable derivative are defined in section 2. In section 3, the proposed methods are applied to the fractional modified Camassa-Holm equation for obtaining some new exact solutions in section 4. In section 5, a discussion of the results is clarified. In final section, includes a conclusion which contains all outputs in this article.

### Conformable Fractional Derivative

Khalil et al. defined the below theorem for the fractional derivatives [29]:

Let  $h: [0, \infty) \rightarrow R$  be a function and its fractional conformable derivative of  $h$  order  $\alpha$  is,

$$D_t^\alpha (h)(x) = \lim_{\varepsilon \rightarrow 0} \frac{h(x + \varepsilon x^{1-\alpha}) - h(x)}{\varepsilon}, \quad (2)$$

$\alpha \in (0, 1) \forall x > 0$ . Some of important properties of conformable derivative as follows:

Suppose  $\alpha \in (0, 1]$  and  $g, h$  be  $\alpha$ -differentiable at a point  $t > 0$ . Then,

$$T_\alpha(ag + bh) = aT_\alpha(g) + bT_\alpha(h) \quad \forall a, b \in R.$$

$$T_\alpha(k^p) = pk^{p-1} \quad \forall p \in R.$$

$$T_\alpha(\beta) = 0, \text{ for all constant functions } g(t) = \beta.$$

$$T_\alpha(gh) = gT_\alpha(h) + hT_\alpha(g).$$

$$T_\alpha\left(\frac{g}{h}\right) = \frac{hT_\alpha(g) - gT_\alpha(h)}{g^2}.$$

$$\text{If } g \text{ is differentiable, } T_\alpha(g)(t) = t^{1-\alpha} \frac{dg}{dt}(t).$$

### First Integral Method

Introducing the wave transformation:

$$u(x, t) = U(\xi), \quad \xi = x - k \frac{t^\alpha}{\Gamma(1+\alpha)} \quad (3)$$

Eqn. (1) reduce the form of eqn.(4) an ODE:

$$\frac{dQ}{d\xi} = \frac{dQ}{dX} \frac{dX}{d\xi} + \frac{dQ}{dY} \frac{dY}{d\xi} = (g(X) + h(X)Y) \sum_{i=0}^m a_i(X) Y^i. \quad (7)$$

Assume that  $m = 1$  then coefficients of  $Y^i$  ( $i = 0, 1$ ) in eqn.(40), we get:

$$a_1(X) = a_1(X) \cdot h(X) \quad (8)$$

$$a_0(X) = a_0(X) \cdot h(X) + a_1(X) \cdot g(X) \quad (9)$$

$$a_1(X) \cdot \left( \frac{k-2\sigma}{k} X - \frac{\beta}{3k} X^3 \right) = a_0(X) \cdot g(X). \quad (10)$$

Since  $a_i(X)$  are polynomials,  $a_1(X)$  is constant and  $h(X) = 0$  from eqn.(41)

Take  $a_1(X) = 1$  and for the equilibrium of  $a_0(X)$  and  $g(X)$ ,  $\deg(g(X)) = 1$ .

Let  $(X) = A_0 + A_1 X$ , then

$$a_0(X) = A_0 X + \frac{1}{2} A_1 X^2 + B_0, \quad (11)$$

$A_2$  is integration constant. A nonlinear system of algebraic equations are obtained from  $a_0(X)$ ,  $g(X)$  and eqn.(10).

$$kU''(\xi) + (2\sigma - k)U(\xi) + \frac{\beta}{3}U^3(\xi) = 0 \quad (4)$$

and then we can write two dimensional autonomous system

$$\frac{dX}{d\xi} = Y(\xi)$$

$$\frac{dY}{d\xi} = \frac{k-2\sigma}{k}X(\xi) - \frac{\beta}{3k}X^3(\xi) \quad (5)$$

According to first integral method,  $X$  and  $Y$  be a non-trivial solutions of the eqn.(5). Also, irreducible polynomial  $Q(X, Y) = \sum_{i=0}^m a_i(X)Y^i$  is exist in  $\mathbb{C}[X, Y]$  such that

$$Q(X(\xi), Y(\xi)) = \sum_{i=0}^m a_i(X(\xi))Y^i(\xi) = 0 \quad (6)$$

where  $a_m(X) \neq 0$  and  $i = 0, 1, \dots, m$ . By division theorem  $\exists$  a polyn.  $g(X) + h(X)Y$  such that

$$A_1 = \sqrt{\frac{-2\beta}{3k}}, B_0 = \frac{k-2\sigma}{k} \sqrt{\frac{3k}{-2\beta}}, A_0 = 0 \quad (12)$$

$$A_1 = -\sqrt{\frac{-2\beta}{3k}}, B_0 = -\frac{(k-2\sigma)}{k} \sqrt{\frac{3k}{-2\beta}}, A_0 = 0 \quad (13)$$

under the conditions given by eqs. (12) and (13) in eq. (6), we have;

$$Y(\xi) = \pm \left( \frac{k-2\sigma}{k} \sqrt{\frac{3k}{-2\beta}} + \frac{1}{2} \sqrt{\frac{-2\beta}{3k}} X^2(\xi) \right) \quad (14)$$

using eq.(14) and eq. (5), eqn.(14) is converted to following Ricatti equation:

$$U'(\xi) = \pm \left( \frac{k-2\sigma}{k} \sqrt{\frac{3k}{-2\beta}} + \frac{1}{2} \sqrt{\frac{-2\beta}{3k}} U^2(\xi) \right) \quad (15)$$

the solutions of the modified fractional Camassa – Holm equation is obtained as:

$$u_1(x, t) = \sqrt{\frac{3k-6\sigma}{\beta}} \tanh\left(\sqrt{\frac{2\sigma-k}{2k}} \left(x - k \frac{t^\alpha}{\Gamma(1+\alpha)} + \xi_0\right)\right) \quad (16)$$

$$u_2(x, t) = -\sqrt{\frac{3k-6\sigma}{\beta}} \tanh\left(\sqrt{\frac{2\sigma-k}{2k}} \left(x - k \frac{t^\alpha}{\Gamma(1+\alpha)} + \xi_0\right)\right) \tag{17}$$

$$u_3(x, t) = \sqrt{\frac{3k-6\sigma}{\beta}} \coth\left(\sqrt{\frac{2\sigma-k}{2k}} \left(x - k \frac{t^\alpha}{\Gamma(1+\alpha)} + \xi_0\right)\right) \tag{18}$$

$$u_4(x, t) = -\sqrt{\frac{3k-6\sigma}{\beta}} \coth\left(\sqrt{\frac{2\sigma-k}{2k}} \left(x - k \frac{t^\alpha}{\Gamma(1+\alpha)} + \xi_0\right)\right) \tag{19}$$

$$u_5(x, t) = \sqrt{\frac{-3k+6\sigma}{\beta}} \tanh\left(\sqrt{\frac{k-2\sigma}{2k}} \left(x - k \frac{t^\alpha}{\Gamma(1+\alpha)} + \xi_0\right)\right) \tag{20}$$

$$u_6(x, t) = -\sqrt{\frac{-3k+6\sigma}{\beta}} \tanh\left(\sqrt{\frac{k-2\sigma}{2k}} \left(x - k \frac{t^\alpha}{\Gamma(1+\alpha)} + \xi_0\right)\right) \tag{21}$$

$$u_7(x, t) = \sqrt{\frac{-3k+6\sigma}{\beta}} \cot\left(\sqrt{\frac{k-2\sigma}{2k}} \left(x - k \frac{t^\alpha}{\Gamma(1+\alpha)} + \xi_0\right)\right) \tag{22}$$

$$u_8(x, t) = -\sqrt{\frac{-3k+6\sigma}{\beta}} \cot\left(\sqrt{\frac{k-2\sigma}{2k}} \left(x - k \frac{t^\alpha}{\Gamma(1+\alpha)} + \xi_0\right)\right) \tag{23}$$

**Functional Variable Method**

Introducing the wave transformation:

$$u(x, t) = U(\xi), \xi = x - k \frac{t^\alpha}{\Gamma(1+\alpha)} \tag{3}$$

Eqn. (1) reduce the form of eqn.(4) an ordinary differential equation:

$$kU''(\xi) + (2\sigma - k)U(\xi) + \frac{\beta}{3}U^3(\xi) = 0 \tag{4}$$

according to functional variable method, we take  $u_\xi = F(u)$  and some successive derivatives of  $u(\xi)$  to following:

$$u_{\xi\xi} = \frac{1}{2}(F^2)'$$

$$u_{\xi\xi\xi} = \frac{1}{2}(F^2)''\sqrt{F^2} \tag{24}$$

$$u_{\xi\xi\xi\xi} = \frac{1}{2}[(F^2)'''F^2 + \frac{1}{2}(F^2)''(F^2)'],$$

Thus we obtain,

$$(F^2)' = \frac{2(k-2\sigma)}{k}u - \frac{2\beta}{3k}u^3 \tag{25}$$

integrating the eqn. (25), we have

$$F(u) = \sqrt{-\frac{\beta}{6k}}u \sqrt{u^2 - \frac{6(k-2\sigma)}{\beta}} \tag{26}$$

from  $u_\xi = F(u)$  and (26) we deduce that

$$\int \frac{du}{u \sqrt{u^2 - \frac{6(k-2\sigma)}{\beta}}} = \sqrt{-\frac{\beta}{6k}}(\xi + \xi_0) \tag{27}$$

$\xi_0$  is a integration constant. After integrating (27), we achieve the following exact solutions:

**Case 1.** If  $k = 2\sigma$ , then

$$u_1(x, t) = \pm \frac{1}{\sqrt{-\frac{\beta}{6k}\left(x - k \frac{t^\alpha}{\Gamma(1+\alpha)} + \xi_0\right)}} \tag{28}$$

**Case 2.** If  $\frac{6(k-2\sigma)}{\beta} > 0$ , then

$$u_9(x, t) = \sqrt{\frac{6(k-2\sigma)}{\beta}} \sec\left(\sqrt{\frac{2\sigma-k}{k}}\left(x - k\frac{t^\alpha}{\Gamma(1+\alpha)} + \xi_0\right)\right) \quad (29)$$

$$u_{10}(x, t) = -\sqrt{\frac{6(k-2\sigma)}{\beta}} \sec\left(\sqrt{\frac{2\sigma-k}{k}}\left(x - k\frac{t^\alpha}{\Gamma(1+\alpha)} + \xi_0\right)\right) \quad (30)$$

$$u_{11}(x, t) = \sqrt{\frac{6(k-2\sigma)}{\beta}} \csc\left(\sqrt{\frac{2\sigma-k}{k}}\left(x - k\frac{t^\alpha}{\Gamma(1+\alpha)} + \xi_0\right)\right) \quad (31)$$

$$u_{12}(x, t) = -\sqrt{\frac{6(k-2\sigma)}{\beta}} \csc\left(\sqrt{\frac{2\sigma-k}{k}}\left(x - k\frac{t^\alpha}{\Gamma(1+\alpha)} + \xi_0\right)\right) \quad (32)$$

**Case 3.** If  $\frac{6(k-2\sigma)}{\beta} < 0$ , then

$$u_{13}(x, t) = \sqrt{\frac{6(2\sigma-k)}{\beta}} \operatorname{sech}\left(\sqrt{\frac{k-2\sigma}{k}}\left(x - k\frac{t^\alpha}{\Gamma(1+\alpha)} + \xi_0\right)\right) \quad (33)$$

$$u_{14}(x, t) = -\sqrt{\frac{6(2\sigma-k)}{\beta}} \operatorname{sech}\left(\sqrt{\frac{k-2\sigma}{k}}\left(x - k\frac{t^\alpha}{\Gamma(1+\alpha)} + \xi_0\right)\right) \quad (34)$$

$$u_{15}(x, t) = \sqrt{\frac{6(2\sigma-k)}{\beta}} \operatorname{csch}\left(\sqrt{\frac{k-2\sigma}{k}}\left(x - k\frac{t^\alpha}{\Gamma(1+\alpha)} + \xi_0\right)\right) \quad (35)$$

$$u_{16}(x, t) = -\sqrt{\frac{6(2\sigma-k)}{\beta}} \operatorname{csch}\left(\sqrt{\frac{k-2\sigma}{k}}\left(x - k\frac{t^\alpha}{\Gamma(1+\alpha)} + \xi_0\right)\right) \quad (36)$$

## Discussion

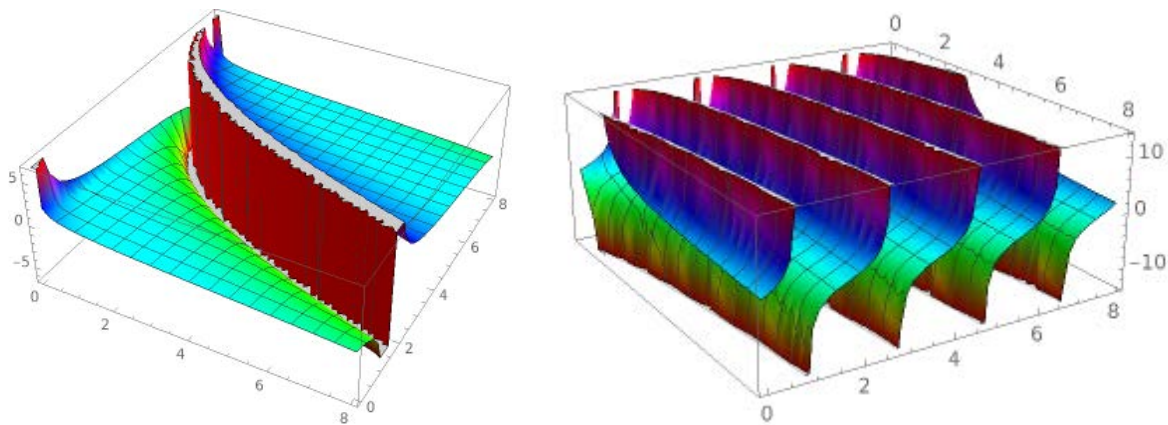


**Figure 1** – 3D plots of the exact solution  $u_3(x, t)$  and  $u_5(x, t)$  respectively, for the case of;  $k = -2.23$ ,  $\sigma = -0.75$ ,  $\beta = 2.07$ ,  $\alpha = 0.41$  and  $k = 0.85$ ,  $\sigma = -1.81$ ,  $\beta = -2.88$ ,  $\alpha = 0.3$

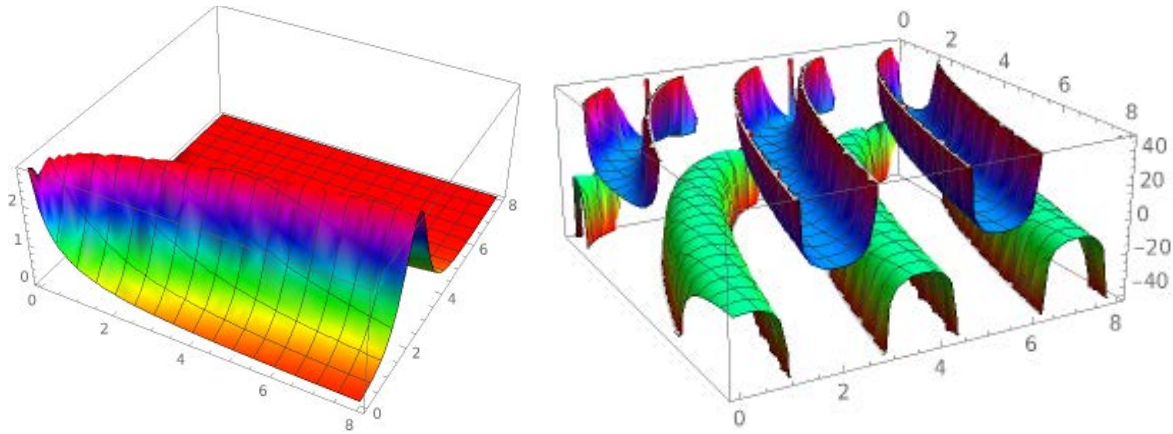


**Figure 2** – 3D plots of the exact solution  $u_9(x, t)$  and  $u_{12}(x, t)$  respectively, for the case of;  
 $k = 1.009, \sigma = -1.17, \beta = 2.39, \alpha = 0.399$  and  $k = -1.55, \sigma = -3.4, \beta = 0.74, \alpha = 0.4$

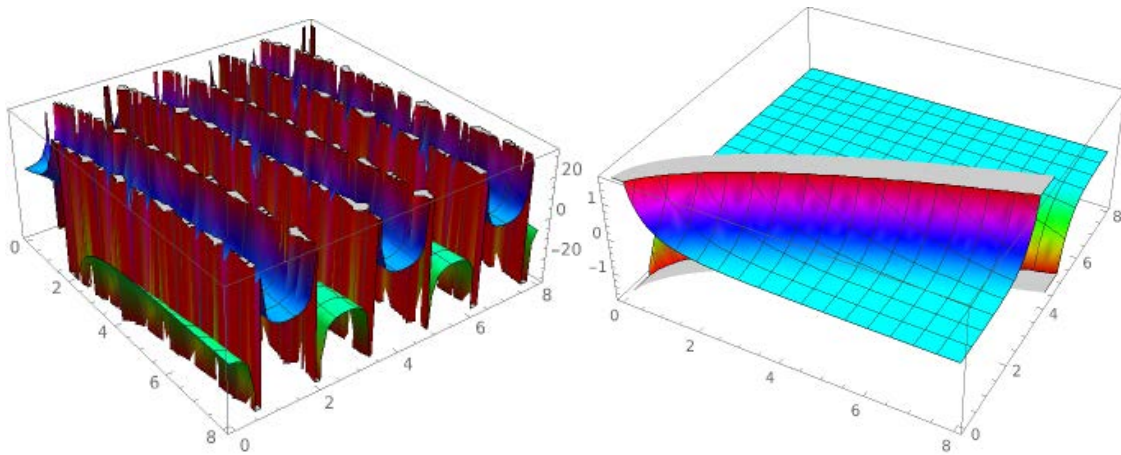


**Figure 3** – 3D plots of the exact solution  $u_{13}(x, t)$  and  $u_{16}(x, t)$  respectively, for the case of;  
 $k = 0.48, \sigma = 1.43, \beta = 2.39, \alpha = 0.44$  and  $k = 1.27, \sigma = -1.86, \beta = -2.08, \alpha = 0.54$

In this section, we have presented some comparisons about physical behaviours. First method gives us hyperbolic solutions and trigonometric solutions (see Fig. 1-4); on the other hand, the second one gives rational solutions, hyperbolic solutions and periodic solutions. Compacton waves and kink soliton waves have been achieved via first method, compacton waves and bell-shaped soliton waves have also been obtained via second method. Thanks to these comparisons, we can have an idea about physical interpretation of other nonlinear FPDEs.

### Conclusion

In this study, thanks to FVM and FIM, we have attained new exact solutions of the fractional modified Camassa – Holm equation. The proposed methods are powerful, reliable and effective to

obtain nonlinear FPDEs defined by conformable derivative. Main advantage of these methods is generating more type of solution functions than the other analytical methods. Trueness of solution functions have also been proved by using the Mathematica program. Additionally, some 3D graphs have been examined for proper values of the parameters. Obtained results and comparisons show that methods will be useful to make the physical interpretation of nonlinear FPDEs arising in applied physics and mathematics.

### References

- 1 Podlubny, Fractional Differential Equations: an Introduction to Fractional Derivatives, Fractional Differential Equations, to Methods of Their Solution and Some of Their Applications. Elsevier, 1998K.

- Satou, H. Ikezoe, S. Mitsuoka, K. Nishio, and S. C. Jeong, *Phys. Rev. C* 65 (2002) 054602.
- 2 Hilfer, R., *Applications of fractional Calculus in Physics*, World Scientific Publishing, River Edge, NJ, USA (2000).
- 3 Kilbas, A., Srivastava, H. M., Trujillo, J. J., *Theory and Applications of Fractional Differential Equations*. North-Holland Mathematics Studies, Elsevier Science, Amsterdam, The Netherlands, 204 (2006).
- 4 Caputo, M., *Elasticita e Dissipazione*. Zanichelli, Bologna, (1969).
- 5 Li, C., Guo, Q., Zhao, M., On the solutions of (2+1)-dimensional time – fractional Schrödinger equation, *Appl. Math. Lett.*, 94 (2019): 238–243.
- 6 Atangana A., D. Baleanu, D., New fractional derivatives with nonlocal and non-singular kernel: theory and application to heat transfer model, *Therm. Sci.*, 20 (2016): 763.
- 7 Liu, W., Chen, K., The functional variable method for finding exact solutions of some nonlinear time fractional differential equations, *Pramana – J. Phys.*, 81 (2013): 3.
- 8 Wazwaz, A. M., The extended tanh method for new solitons solutions for many forms of the fifth order KdV equations, *Appl. Math. Comput.*, 184 (2), (2007): 1002-1014.
- 9 Hosseini, K., Ansari, R., Gholamin, P., Exact solutions of some nonlinear systems of partial differential equations by using the first integral method, *J. Math. Anal. and Apps.*, 387, (2012): 807 – 814.
- 10 Rezazadeh, H., et al., New exact solutions of nonlinear conformable time-fractional Phi-4 equation. *Chinese Journal of Physics*, 56(6) (2018) 2805-2816.
- 11 Kaplan, M., Akbulut, A., Bekir, A., Solving space-time fractional differential equations by using modified simple equation method, *Commun. Theor. Phys.*, 65(5) (2016): 563.
- 12 Odabasi, M., Traveling wave solutions of conformable time-fractional Zakharov–Kuznetsov and Zoomeron equations, *Chinese Journal of Physics*, 64 (2020): 194-202.
- 13 Bekir, A., Guner, O., Bhrawy, A. H., Biswas, A., Solving nonlinear fractional differential equations using exp-function and  $G'/G$ -expansion methods. *Rom. J. Phys.* 60(3–4) (2015): 360–378.
- 15 Pandir, Y., Gurefe Y., Misirli, E., The extended trial equation method for some time-fractional differential equations, *Discrete Dyn. Nat. Soc.*, 2013 (2013): 491359.
- 16 Gurefe, Y., The generalized Kudryashov method for the nonlinear fractional partial differential equations with the beta-derivative, *Revista Mexicana de Física*, 66 (2020): 771-781.
- 17 Youssri, Y. H., Abd-Elhameed, W. M., *Romanian Journal of Physics* 63 (2018): 107.
- 18 Öztürk, Z., Bilgil, H., Exact Solutions of Rosenzweig-MacArthur (RM) Model Equations by Using Exp Function Method. *Avrupa Bilim ve Teknoloji Dergisi*, 16 (2019): 427-433.
- 19 Kurt, A., Tasbozan, and O., Cenesiz, Y., Homotopy analysis method for conformable burgers korteweg-de vries equation, *Bull. Math. Sci. Appl.*, 17 (17) (2016): 23.
- 20 He, J. H., Variation iteration method-a kind of non-linear analytic technique: some examples, *Int. J. Non-linear Mech.* 34 (4) (1999): 699–708.
- 21 Prakash, A., Kumar, M., Baleanu, D., A new iterative technique for a fractional model of nonlinear Zakharov–Kuznetsov equations via Sumudu transform, *Appl. Math. Comput.*, 334 (2018): 30–40.
- 22 Akbulut, A., Kaplan, M., Auxiliary equation method for time-fractional differential equations with conformable derivative, *Comput Math Appl.*, 75 (2018) 876-882.
- 23 Guner, O., New exact solutions to the spacetime fractional nonlinear wave equation obtained by the ansatz and functional variable methods, *Opt Quant Electron*, 50 (2018): 38.
- 24 Kadomtsev, B. B., Petviashvili, V. I., Relativistically invariant two-dimensional models of field theory which are integrable by means of the inverse scattering problem method, *Sov. Phys. JETP.*, 74 (6) (1978): 1017-1027.
- 25 Cheng, Y. F., Dai, T. Q., Exact solutions of the Klein-Gordon equation with a ring-shaped modified Kratzer potential. *Chin. J. Phys.*, 45 (5) (2007): 480-487.
- 26 Khater, M. M. A., Zahran, E. H. M., New method to evaluating exact and traveling wave solutions for non-linear evolution equations, *J. Comput. Theor. Nanosci*, 12 (2015): 1 – 9.
- 27 Eslami, M., Rezazadeh, H., The first integral method for Wu–Zhang system with conformable time fractional derivative, *Calcolo*, 53 (2016): 475-485.
- 28 Inc, M., Inan, E., Ugurlu, Y., New applications of the functional variable method. *Optik*, 136 (2017): 374– 381.
- 29 Zulfiqar, A., Ahmad, J., Exact solitary wave solutions of fractional modified Camassa-Holm equation using an efficient method, *Alexandria Engineering Journal*, 59(5) (2020): 3565-3574.
- 30 Khalil R., Al Horani, M., Yousef, A., Sababheh, M., A new definition of fractional derivative, *Journal of Computational and Applied Mathematics*, 264 (2014): 65-70.

M.K. Daulybayev<sup>1,2\*</sup> , K.T. Konisbayeva<sup>1</sup> , N.R. Tortbay<sup>1</sup> 

<sup>1</sup>Al-Farabi Kazakh National University, Almaty, Kazakhstan

<sup>2</sup>Institute of Information and Computational Technologies, Almaty, Kazakhstan

\*e-mail: mdaulybayev@gmail.com

## Integral bvp for singularly perturbed system of differential equations

**Abstract.** The article presents a two-point integral BVP for singularly perturbed systems of linear ordinary differential equations. The integral BVP for singularly perturbed systems of ordinary differential equations previously has not been considered. The paper shows the influence of nonlocal boundary conditions on the asymptotic of the solution of the regarded BVP and the significant effect of integral terms in the definition of the limiting BVP. An explicit constructive formula for the solution of this BVP using initial and boundary functions of the homogeneous perturbed equation is obtained. A theorem on asymptotic estimates of the solution and its derivatives is given. It is established that the solution of the integral BVP at the point  $t = 0$  is infinitely large as  $\mu \rightarrow 0$ . From here, it follows that the solution of the considered boundary value problem has an initial jump of zero order. It is found that the solution of the original integral BVP is not close to the solution of the usual limiting unperturbed BVP. A changed limiting BVP is obtained. The presence of integrals in the boundary conditions leads to the fact that the limiting BVP is determined by the changed boundary conditions. This follows from the presence of the jump and its order. A theorem on the close between the solutions of the original perturbed and changed limiting problems is given.

**Key words:** singularly perturbation, small parameter, asymptotic, initial jumps, asymptotic estimate, BVP.

### Introduction

Many applied problems lead to the consideration of differential systems with small parameters. In the case when the type of the given system changes as small parameters tend to zero, then it is said that it is singularly perturbed. The systematic study of the theory of singularly perturbed equations began with the works of A.N. Tikhonov [1] and V. Vazov [2], where they prove their famous theorems on the passage to the limit in singularly perturbed problems. A significant contribution to the further development of the main directions of the theory was made by L.S. Pontryagin [3], N.N. Bogolyubov, Yu.A. Mitropol'skiy [4], M.I. Vishik, L.A. Lyusternik [5], A.B. Vasilieva, V.F. Butuzov [6], S.A. Lomov [7], Imanaliev M.I. [8] and others.

In the works, [9-12] initial problems with infinitely large value of an initial data for a sufficiently small value of the parameter were studied. In this case, the solution to the original problem for a sufficiently small value of the parameter approached the solution of the changed

degenerate problem. Such initial problems are called Cauchy problems with an initial jump.

BVPs for differential, integro-differential equations with small parameters at the highest derivatives are studied in [13-15]. Here take places initial and boundary jumps phenomena when some derivatives of the solution are unbounded at the left point of the segment or at the both ends. In the work [16] initial problem for piecewise constant argument differential equations is studied.

The boundary value problems considered in [17, 18] are local. We consider nonlocal boundary value problems for a system of singularly perturbed differential equations.

For systems of differential equations, such problems have not been considered previously. In these problems, in addition to the initial jumps of the fast and slow variables, the phenomenon of the initial jumps of the integral terms also arises. Thus, the presence of integrals in the boundary conditions leads to a significant modification of the limiting boundary value problem, to which the solution of the original perturbed nonlocal boundary value problem tends.

**Problem statement and auxiliary materials**

We present the following singularly perturbed system of ordinary differential equations of the form

$$\begin{cases} \mu z'' + A_1(t)z' + B_1(t)z + C_1(t)y = F_1(t) \\ y' + A_2(t)z' + B_2(t)z + C_2(t)y = F_2(t) \end{cases} \quad (1)$$

with the following boundary conditions

$$h_1 z(t, \mu) \equiv z(0, \mu) = \alpha$$

$$h_2 z(t, \mu) \equiv z(1, \mu) - \int_0^1 \sum_{i=0}^1 a_i(x) z^{(i)}(x, \mu) dx = \beta \quad (2)$$

$$h_3 y(t, \mu) \equiv y(0, \mu) = \gamma$$

$$z_1^{(j)}(t, \mu) = z_{10}^{(j)}(t) + O(\mu), \quad j = 0, 1,$$

$$z_2^{(j)}(t, \mu) = \frac{1}{\mu^j} \exp\left(\frac{1}{\mu} \int_0^t \kappa(x) dx\right) (\kappa^j(t) z_{20}(t) + O(\mu)), \quad j = 0, 1, \quad (4)$$

Where  $\kappa(t) = -A_1(t) < 0$ , functions  $z_{i0}(t)$ ,  $i = 1, 2$  are solutions of the problems  $A_1(t)z'_{10} + B_1(t)z_{10} = 0$ ,  $z_{10}(0) = 1$ ,  $A_1(t)z'_{20} + (A_1(t) - B_1(t))z_{20} = 0$ ,  $z_{10}(0) = 1$  respectively have the form

$$z_{10}(t) = \exp\left(-\int_0^t \frac{B_1(x)}{A_1(x)} dx\right), \quad (5)$$

$$z_{20}(t) = \frac{A_1(0)}{A_2(t)} \exp\left(\int_0^t \frac{B_1(x)}{A_1(x)} dx\right)$$

Let the function  $K(t, s, \varepsilon)$  as  $0 \leq s \leq t \leq 1$  is solution to the problem

$$\begin{aligned} L_\mu K(t, \mu, \varepsilon) &= 0, \quad K(s, s, \mu) = \\ &= 0, \quad K'(s, s, \mu) = 1 \end{aligned} \quad (6)$$

The function  $K(t, s, \mu)$  – the Cauchy function, which can be represented as [8]:

where  $\mu > 0$  – small parameter,  $\alpha, \beta, \gamma$  – given constants, which do not depend on  $\mu$ .

Now we make two assumptions:

I.  $A_i(t), B_i(t), C_i(t), F_i(t), i = 1, 2$  are sufficiently smooth in the segment  $0 \leq t \leq 1$ ;

II.  $A_1(t) \geq \delta = const > 0, 0 \leq t \leq 1$

Some other conditions will be imposed later. We view the following homogeneous singularly perturbed differential equation

$$L_\mu z \equiv \mu z'' + A_1(t)z' + B_1(t)z = 0 \quad (3)$$

If the conditions I, II are satisfied, then the fundamental set of solutions  $z_i(t, \mu), i = 1, 2$  of the equation (3) has the asymptotic representation as  $\mu \rightarrow 0$  [8]:

$$K(t, s, \mu) = \frac{W(t, s, \mu)}{W(s, \mu)}, \quad (7)$$

where  $W(s, \varepsilon)$  – Wronskian, composed of a fundamental set of solutions  $z_1(s, \mu), z_2(s, \mu)$  equation (3), and  $W(t, s, \mu)$  – determinant, obtained from  $W(s, \mu)$  by replacing its second row with  $z_1(s, \mu), z_2(s, \mu)$ . For the function  $K(t, s, \mu)$ , the following estimates can be obtained:

$$\begin{aligned} K^{(j)}(t, s, \mu) &= -\mu \frac{z_{10}^{(j)}(t)}{z_{10}(s)\kappa(s)} + \\ &+ \mu^{1-j} \exp\left(\frac{1}{\mu} \int_s^t \kappa(x) dx\right) \frac{\kappa^j(t) z_{20}(t)}{z_{20}(s)\kappa(s)} + \\ &+ O\left(\mu^2 + \mu^{2-j} \exp\left(\frac{1}{\mu} \int_s^t \kappa(x) dx\right)\right), \quad j = 0, 1, \end{aligned} \quad (8)$$

where  $z_{i0}(t), i = 1, 2$  is expressed by formula (5).

Now we introduce the boundary functions of the function  $\Phi_i(t, \mu)$ ,  $i = 1, 2$ , which are solutions of the following problem

$$L_\mu \Phi_i(t, \mu) = 0, \quad h_k \Phi_i(t, \mu) = \delta_{ki}, \quad k, i = 1, 2, \quad (9)$$

where  $\delta_{ki}$  – Kronecker symbol. Consider the determinant

$$\Delta(\mu) = \begin{vmatrix} h_1 z_1(t, \mu) & h_1 z_2(t, \mu) \\ h_2 z_1(t, \mu) & h_2 z_2(t, \mu) \end{vmatrix}$$

For the determinant  $\Delta(\mu)$ , taking into account (2), (4), (5), the asymptotic representation as  $\mu \rightarrow 0$  is valid

$$\Delta(\mu) = \Delta_0 + O(\mu), \quad (10)$$

where  $\Delta_0 = a_1(0) - h_2 z_{10}(t)$ .

III. Let  $\Delta_0 \neq 0$

Boundary functions  $\Phi_i(t, \mu)$ ,  $i = 1, 2$  can be represented in the form [8]:

$$\Phi_i(t, \mu) = \frac{\Delta_i(t, \mu)}{\Delta(\mu)}, \quad i = 1, 2, \quad (11)$$

where  $\Delta_i(t, \mu)$  is the determinant obtained by replacing the  $i$ -th row with the fundamental set of solutions  $z_1(s, \mu)$ ,  $z_2(s, \mu)$  to equation (3).

For the boundary functions  $\Phi_i(t, \mu)$ ,  $i = 1, 2$  from (11), with considering (4), (10), one can obtain the following asymptotic representations as  $\mu \rightarrow 0$ :

$$\begin{aligned} \Phi_1^{(j)}(t, \mu) &= \frac{a_1(0)z_{10}^{(j)}(t)}{\Delta_0} - \frac{1}{\mu^j} \exp\left(\frac{1}{\mu} \int_0^t \kappa(x) dx\right) \frac{\kappa^j(t)z_{20}(t)z_{10}(t)}{\Delta_0} + \\ &+ O\left(\mu + \frac{1}{\mu^{j-1}} \exp\left(\frac{1}{\mu} \int_0^t \kappa(x) dx\right)\right), \quad j = 0, 1, \\ \Phi_2^{(j)}(t, \mu) &= -\frac{z_{10}^{(j)}(t)}{\Delta_0} + \frac{1}{\mu_j} \exp\left(\frac{1}{\mu} \int_0^t \kappa(x) dx\right) \frac{\kappa^j(t)z_{20}(t)}{\Delta_0} + \\ &+ O\left(\mu + \frac{1}{\mu^{j-1}} \exp\left(\frac{1}{\mu} \int_0^t \kappa(x) dx\right)\right), \quad j = 0, 1, \end{aligned} \quad (12)$$

**Main results.**

From the system (1), we find

$$\begin{aligned} y(t, \mu) &= \gamma e^{-\int_0^t C_2(s) ds} + \int_0^t (F_2(s) - \\ &- A_2(s)z'(s, \mu) - B_2(s)z(s, \mu)) e^{-\int_0^s C_2(p) dp} ds \end{aligned} \quad (13)$$

Let us substitute in the first equation of system (1) the expression (13) with respect to  $z(s, \mu)$ , we acquire the Volterra integro differential equation

$$\begin{aligned} L_\mu y &\equiv \mu z'' + A_1(t)z' + B_1(t)z = \\ &= F(t) + \int_0^1 \sum_{i=0}^1 H_i(t, s) z^{(i)}(s, \mu) ds \end{aligned} \quad (14)$$

with the following boundary conditions

$$\begin{aligned} h_1 z(t, \mu) &\equiv z(0, \mu) = \alpha \\ h_2 z(t, \mu) &\equiv z(1, \mu) - \int_0^1 \sum_{i=0}^1 a_i(x) z^{(i)}(x, \mu) dx = \beta \end{aligned} \quad (15)$$

where

$$\begin{aligned}
 F(t) &= F_1(t) - \gamma C_1(t) e^{-\int_0^t C_2(s) ds} - \int_0^t C_1(t) F_2(s) e^{-\int_s^t C_2(p) dp} ds, \\
 H_0(t, s) &= C_1(t) B_2(s) e^{-\int_s^t C_2(p) dp}, \quad H_1(t, s) = C_1(t) A_2(s) e^{-\int_s^t C_2(p) dp},
 \end{aligned}
 \tag{16}$$

We seek the solution to the BVP (14), (15) in the form:

$$\begin{aligned}
 z(t, \mu) &= C_1 \Phi_1(t, \mu) + C_2 \Phi_2(t, \mu) + \\
 &+ \frac{1}{\mu} \int_0^t K(t, s, \mu) u(s, \mu) ds
 \end{aligned}
 \tag{17}$$

where  $C_i, i = 1, 2$  - unknown constants,  $u(t, \mu)$  satisfies the integral equations

$$u(t, \mu) = f(t, \mu) + \int_0^t H(t, s, \mu) u(s, \mu) ds. \tag{18}$$

Here

$$\begin{aligned}
 f(t, \mu) &= F(t) + C_1 \int_0^1 \sum_{i=0}^1 H_i(t, s) \Phi_1^{(j)}(s, \mu) ds + \\
 &+ C_2 \int_0^1 \sum_{i=0}^1 H_i(t, s) \Phi_2^{(j)}(s, \mu) ds,
 \end{aligned}$$

$$H(t, s, \mu) = \frac{1}{\mu} \int_s^t \sum_{i=0}^1 H_i(t, p) K^{(j)}(p, s, \mu) dp \tag{19}$$

The kernel  $H(t, s, \mu)$  is continuous in the domain  $0 \leq t \leq 1, 0 \leq s \leq t$  and is bounded for sufficiently small  $\mu$ . Therefore, the resolvent  $R(t, s, \mu)$  of the kernel  $H(t, s, \mu)$  is also limited and also has the following asymptotic representation

$$R(t, s, \mu) = \bar{R}(t, s) + O(\mu), \tag{20}$$

where  $\bar{R}(t, s)$  is the part of the resolvent  $R(t, s, \mu)$  which do not depend on  $\mu$ .

Solving equation (18) using the resolvent we find

$$z(t, \mu) = \sum_{i=1}^2 C_i Q_i(t, \mu) + P(t, \mu), \tag{21}$$

where

$$Q_i(t, \mu) = \Phi_i(t, \mu) + \frac{1}{\mu} \int_0^t K(t, s, \mu) \bar{\phi}_i(s, \mu) ds, \tag{22}$$

$$i = 1, 2, \quad P(t, \mu) = \frac{1}{\mu} \int_0^t K(t, s, \mu) \bar{F}(s, \mu) ds$$

$$\bar{\phi}_i(t, \mu) = \int_0^1 \sum_{j=0}^1 \bar{H}_j(t, s, \mu) \Phi_i^{(j)}(s, \mu) ds, \tag{23}$$

$$i = 1, 2, \quad \bar{F}(t, \mu) = F(t) + \int_0^t R(t, s, \mu) F(s) ds,$$

$$\begin{aligned}
 \bar{H}(t, s, \mu) &= H_j(t, s) + \int_s^t R(t, p, \mu) H_i(p, s) ds, \\
 & \quad j = 0, 1
 \end{aligned}$$

For the function  $\bar{\phi}_i(t, \mu), \bar{F}(t, \mu), \bar{H}_j(t, s, \mu)$  from (23), in view of (20), (12), we get the following asymptotic representations as  $\mu \rightarrow 0$ :

$$\bar{\phi}_1(t, \mu) = \bar{\phi}_1(t) - \bar{H}_1(t, t) \frac{z_{10}(t) z_{20}(t)}{\Delta_0} e^{\frac{1}{\mu} \int_0^t \kappa(x) dx} + O(\mu), \tag{24}$$

$$+ O(\mu), \quad \bar{F}(t, \mu) = \bar{F}(t) + O(\mu),$$

$$\bar{\phi}_2(t, \mu) = \bar{\phi}_2(t) - \bar{H}_1(t, t) \frac{z_{20}(t)}{\Delta_0} e^{\frac{1}{\mu} \int_0^t \kappa(x) dx} +$$

$$+ O(\mu), \quad \bar{H}_j(t, s, \mu) = \bar{H}_j(t, s) + O(\mu), \quad j = 0, 1$$

where

$$\bar{\phi}_1(t) = \bar{H}_1(t, 0) \frac{h_2 z_{10}(t)}{\Delta_0} + \int_0^1 \sum_{i=0}^1 \bar{H}_i(t, s) \frac{a_1(0) z_{10}^{(i)}(s)}{\Delta_0} ds,$$

$$\bar{\phi}_2(t) = -\frac{\bar{H}_1(t, 0)}{\Delta_0} - \int_0^1 \sum_{i=0}^1 \bar{H}_i(t, s) \frac{z_{10}^{(i)}(s)}{\Delta_0} ds,$$

Now, from (22), in consideration of (8), (12), (24) we derive the asymptotic representations:

$$\begin{aligned}
 Q_1^{(j)}(t, \mu) &= \frac{a_1(0)z_{10}^{(j)}(t)}{\Delta_0} - \int_0^t \frac{z_{10}^{(j)}(t)\bar{\phi}_1(s)}{z_{10}(s)\kappa(s)} ds - \frac{\kappa^{j-2}(t)\bar{\phi}_1(t)}{\mu^{j-1}} - \\
 &- \frac{1}{\mu} e^{\frac{1}{\mu} \int_0^t \kappa(x) dx} \frac{\kappa^j(t)z_{20}(t)h_2z_{10}(t)}{\Delta_0} \left( 1 + \int_0^t \frac{\bar{H}_1(s,s)}{\kappa(s)} ds \right) + O \left( \mu + \frac{1}{\mu^{j-1}} e^{\frac{1}{\mu} \int_0^t \kappa(x) dx} \right), \\
 Q_2^{(j)}(t, \mu) &= -\frac{z_{10}^{(j)}(t)}{\Delta_0} - \int_0^t \frac{z_{10}^{(j)}(t)\bar{\phi}_2(s)}{z_{10}(s)\kappa(s)} ds - \frac{\kappa^{j-2}(t)\bar{\phi}_2(t)}{\mu^{j-1}} + \\
 &+ \frac{1}{\mu} e^{\frac{1}{\mu} \int_0^t \kappa(x) dx} \frac{\kappa^j(t)z_{20}(t)}{\Delta_0} \left( 1 + \int_0^t \frac{\bar{H}_1(s,s)}{\kappa(s)} ds \right) + O \left( \mu + \frac{1}{\mu^{j-1}} e^{\frac{1}{\mu} \int_0^t \kappa(x) dx} \right), \\
 P^{(j)}(t, \mu) &= -\int_0^t \frac{z_{10}^{(j)}(t)\bar{F}(s)}{z_{10}(s)\kappa(s)} ds - \frac{\kappa^{j-2}(t)\bar{F}(t)}{\mu^{j-1}} - \\
 &- \frac{1}{\mu^{j-1}} e^{\frac{1}{\mu} \int_0^t \kappa(x) dx} \frac{\kappa^j(t)z_{20}(t)\bar{F}(0)}{\kappa^2(0)} + O \left( \mu + \frac{1}{\mu^{j-2}} e^{\frac{1}{\mu} \int_0^t \kappa(x) dx} \right),
 \end{aligned} \tag{26}$$

From (21), in consideration of (15), we determine the unknown constants  $C_i, i = 1, 2$  from the system

$$\begin{cases} C_1 h_1 Q_1(t, \mu) + C_2 h_1 Q_2(t, \mu) = \alpha - h_1 P(t, \mu), \\ C_1 h_2 Q_1(t, \mu) + C_2 h_2 Q_2(t, \mu) = \beta - h_2 P(t, \mu) \end{cases} \tag{27}$$

where the asymptotic representations are valid

$$h_1 Q_1(t, \mu) = 1, \quad h_1 Q_2(t, \mu) = 0, \quad h_1 P(t, \mu) = 0$$

$$h_2 Q_1(t, \mu) = -\int_0^1 \frac{\bar{z}_{10}(s)\bar{\phi}_1(s)}{z_{10}(s)\kappa(s)} ds + O(\mu),$$

$$h_2 Q_2(t, \mu) = 1 - \int_0^1 \frac{\bar{z}_{10}(s)\bar{\phi}_2(s)}{z_{10}(s)\kappa(s)} ds + O(\mu)$$

$$h_2 P(t, \mu) = -\int_0^1 \frac{\bar{z}_{10}(s)\bar{F}(s)}{z_{10}(s)\kappa(s)} ds + O(\mu),$$

$$\bar{z}_{10}(t) = z_{10}(1) - a_1(s)z_{10}(s) - \int_s^1 \sum_{i=0}^1 a_i(x)z_{10}^{(i)}(x) dx$$

Let the condition be satisfied

$$IV. \quad \omega_0 = 1 - \int_0^1 \frac{\bar{z}_{10}(s)\bar{\phi}_2(s)}{z_{10}(s)\mu(s)} ds \neq 0$$

Then from system (27), in view of (28), we have

$$C_1 = \alpha, \quad C_2 = \omega + O(\mu), \tag{29}$$

where

$$\omega = \frac{1}{\omega_0} \left( \beta + \int_0^1 \frac{\bar{z}_{10}(s)(\alpha\bar{\phi}_1(s) + \bar{F}(s))}{z_{10}(s)\kappa(s)} ds \right) \tag{30}$$

**Theorem 1.** Under conditions I-IV there exists a positive constant  $\mu_0$  that for  $\mu \in (0, \mu_0]$  there exists a unique solution of problem (1), (2) which satisfies the following asymptotic estimates as  $\mu \rightarrow 0$ :

$$\begin{aligned}
 |z^{(j)}(t, \mu)| &\leq C(|\alpha a_1(0) - \beta| + |\alpha A_2(0) + \gamma| + \\
 &+ \max_{0 \leq t \leq 1} |F_1(t)| + \max_{0 \leq t \leq 1} |F_2(t)|) \left( 1 + \frac{1}{\mu^j} e^{-\delta \frac{t}{\mu}} \right) \\
 |y(t, \mu)| &\leq C(|\alpha a_1(0) - \beta| + |\alpha A_2(0) + \\
 &+ \gamma| + \max_{0 \leq t \leq 1} |F_1(t)| + \max_{0 \leq t \leq 1} |F_2(t)|) \left( 1 + e^{-\delta \frac{t}{\mu}} \right)
 \end{aligned} \tag{31}$$

where  $C > 0, \delta > 0$  – some constants independent of  $\mu$ .

**Proof.** In view of (26), (29) from (21) for solutions of the problem (1), (2) we derive the following asymptotic representations as  $\mu \rightarrow 0$ :

$$\begin{aligned}
z^{(j)}(t, \mu) &= \frac{(\alpha a_1(0) - \omega) z_1^{(j)}(t)}{\Delta_0} - \int_0^t \frac{z_{10}^{(j)}(s)(\alpha \bar{\phi}_1(s) + \omega \bar{\phi}_2(s) + \bar{F}(s))}{z_{10}(s)\kappa(s)} ds - \\
&\frac{\kappa_{j-2}(t)(\alpha \bar{\phi}_1(s) + \omega \bar{\phi}_2(s) + \bar{F}(s))}{\mu^{j-1}} - \frac{\kappa^j(t) z_{20}(t)(\alpha h_2 z_{10}(t) + \omega)}{\mu^j \Delta_0} \left( 1 + \int_0^t \frac{\bar{H}_1(s, s)}{\kappa(s)} ds \right) + \\
&+ O \left( \mu + \frac{1}{\mu^{j-1}} e^{\frac{1}{\mu} \int_0^t \kappa(x) dx} \right), j = 0, 1 \\
y(t, \mu) &= \left( \gamma - \frac{A_2(0)(\alpha h_2 z_{10}(t) + \omega)}{\Delta_0} \right) e^{-\int_0^t C_2(s) ds} + \int_0^t \left\{ F_2(s) - A_2(s) \left[ \frac{(\alpha a_1(0) - \omega) z'_{10}(s)}{\Delta_0} - \right. \right. \\
&\left. \left. \int_0^s \frac{z'_{10}(s)(\alpha \bar{\phi}_1(p) + \omega \bar{\phi}_2(p) + \bar{F}(p))}{z_{10}(p)\kappa(p)} dp - \frac{\alpha \bar{\phi}_1(s) + \omega \bar{\phi}_2(s) + \bar{F}(s)}{\kappa(s)} \right] - \right. \\
&\left. - B_2(s) \left[ \frac{(\alpha a_1(0) - \omega) z_{10}(s)}{\Delta_0} - \int_0^s \frac{z_{10}(s)(\alpha \bar{\phi}_1(p) + \omega \bar{\phi}_2(p) + \bar{F}(p))}{z_{10}(p)\kappa(p)} dp \right] \right\} e^{-\int_0^t C_2(p) dp} ds + \\
&+ \frac{A_2(t) z_{20}(t)(\alpha h_2 z_{10}(t) - \omega)}{\Delta_0} \left( 1 + \int_0^t \frac{\bar{H}_1(s, s)}{\kappa(s)} ds \right) e^{\frac{1}{\mu} \int_0^t \kappa(x) dx} + O(\mu)
\end{aligned} \tag{32}$$

We transform in (32) the expressions  $\alpha a_1(0) - \omega$ ,  $\gamma - \frac{A_2(0)(\alpha h_2 z_{10}(t) - \omega)}{\Delta_0}$  to the form

$$\begin{aligned}
\alpha a_1(0) - \omega &= \frac{1}{\omega_0} \left( \alpha a_1(0) - \beta - \int_0^1 \frac{z_{10}(s)(\alpha \bar{\phi}_1(s) + \alpha a_1(0) \bar{\phi}_2(s) + \bar{F}(s))}{z_{10}(s)\kappa(s)} ds \right) \\
\gamma - \frac{A_2(\alpha h_2 z_{10}(t) - \omega)}{\Delta_0} &= \gamma + \alpha A_2(0) - \frac{A_2(0)}{\Delta_0 \omega_0} \left( \alpha a_1(0) - \beta - \int_0^s \frac{\bar{z}_{10}(s)(\bar{F}(s) - \alpha \bar{H}_1(s, 0))}{z_{10}(s)\kappa(s)} ds \right)
\end{aligned} \tag{33}$$

and the expressions  $\alpha \bar{\phi}_1(t) + \omega \bar{\phi}_2(t) + \bar{F}(t)$ ,  $\alpha \bar{\phi}_1(t) + \alpha a_1(0) \bar{\phi}_2(t) + \bar{F}(t)$ ,  $\bar{F}(t) - \alpha \bar{H}_1(t, 0)$  to the form

$$\begin{aligned}
\alpha \bar{\phi}_1(t) + \omega \bar{\phi}_2(t) + \bar{F}(t) &= \frac{1}{\omega_0} (\alpha \bar{\phi}_1(t) + \beta \bar{\phi}_2(t) + \bar{F}(t)) = \\
&= \frac{1}{\omega_0} \left( \frac{\alpha a_1(0) - \beta}{\Delta_0} \bar{H}_1(t, 0) + \frac{\alpha a_1(0) - \beta}{\Delta_0} \int_0^s \sum_{i=0}^1 \bar{H}_i(t, s) z_{10}^{(i)}(s) ds + \bar{F}(t) - \alpha \bar{H}_1(t, 0) \right), \\
\alpha \bar{\phi}_1(t) + \alpha a_1(0) \bar{\phi}_2(t) + \bar{F}(t) &= \bar{F}(t) - \alpha \bar{H}_1(t, 0),
\end{aligned} \tag{34}$$

$$\begin{aligned} \bar{F}(t) - \alpha \bar{H}_1(t, 0) = & -(\alpha A_2(0) + \gamma) \left( C_1(t) e^{-\int_0^t C_2(p) dp} + \int_0^t \bar{R}(t, s) C_1(s) e^{-\int_0^s C_2(p) dp} ds \right) + \\ & + F_1(t) + \int_0^t \bar{R}(t, s) F_1(s) ds - \int_0^t \left( C_1(t) + \int_s^t \bar{R}(t, p) C_1(p) dp \right) F_2(s) e^{-\int_s^t C_2(p) dp} ds \end{aligned}$$

Then from (34) the asymptotic estimate will be represented in the form

$$\begin{aligned} & |\alpha \bar{\varphi}_1(t) + \omega \bar{\varphi}_2(t) + \bar{F}(t)| \leq \\ & \leq C(|\alpha a_1(0) - \beta| + |\alpha A_2(0) + \gamma| + \\ & + \max_{0 \leq t \leq 1} |F_1(t)| + \max_{0 \leq t \leq 1} |F_2(t)|) \end{aligned}$$

$$\begin{aligned} & |\alpha \bar{\varphi}_1(t) + \alpha a_1(0) \bar{\varphi}_2(t) + \bar{F}(t)| \leq \\ & \leq C(|\alpha A_2(0) + \gamma| + \max_{0 \leq t \leq 1} |F_1(t)| + \max_{0 \leq t \leq 1} |F_2(t)|) \end{aligned} \quad (35)$$

Now, from asymptotic formulas (32), in view of (33) – (35), we get estimates (31). Theorem 1 is proved.

Theorem 1 implies that

$$\begin{aligned} z(0, \mu) = O(1), \quad z'(0, \varepsilon) = O\left(\frac{1}{\mu}\right), \\ y(0, \mu) = O(1), \quad y'(0, \mu) = O\left(\frac{1}{\mu}\right), \quad \mu \rightarrow 0 \end{aligned} \quad (36)$$

Consequently, the solution of the integral BVP (1), (2) has an initial jump of zero order at the left point of the segment.

**A changed unperturbed problem.**

In view of the problem (1), (2) as  $\mu = 0$  we obtain the following BVP

$$\begin{aligned} \begin{cases} A_1(t) \tilde{z}' + B_1(t) \tilde{z} + C_1(t) \tilde{y} = F_1(t) \\ \tilde{y}' + A_2(t) \tilde{z}' + B_2(t) \tilde{z} + C_2(t) \tilde{y} = F_2(t) \end{cases} \quad (37) \\ h_1 \tilde{z}(t) = \alpha, \quad h_3 \tilde{y}(t) = \gamma \quad (38) \end{aligned}$$

Now, we investigate the limit passage between the solutions of the perturbed problem (1), (2) and the

usual unperturbed problem (37), (38). In system (1), (2) we carry out a change of variables by the formulae  $u(t, \mu) = z(t, \mu) - \tilde{z}(t)$ ,  $v(t, \mu) = y(t, \mu) - \tilde{y}(t)$ .

Then we get the system

$$\begin{cases} \mu u'' + A_1(t) u' + B_1(t) u + C_1(t) v = -\mu \tilde{z}''(t) \\ v' + A_2(t) u' + B_2(t) u + C_2(t) v = 0 \end{cases} \quad (39)$$

with boundary conditions

$$\begin{aligned} h_1 u(t, \mu) &= 0 \\ h_2 u(t, \mu) &= \beta - h_2 \tilde{z}(t) \\ h_3 v(t, \mu) &= 0 \end{aligned} \quad (40)$$

Since in the boundary conditions (38) we did not use the condition  $h_2 \tilde{z}(t)$ . Therefore in the conditions (40)  $\beta - h_2 \tilde{z}(t) \neq 0$ . Problem (39), (40) is of the same type as problem (1), (2). Then by virtue of Theorem 1 we have the following estimates for  $u(t, \mu), v(t, \mu)$ :

$$|u^{(j)}(t, \mu)| \leq C(|\beta - h_2 \tilde{z}(t)| + \mu) \left(1 + \frac{1}{\mu^j} e^{-\delta \frac{t}{\mu}}\right),$$

$$j = 0, 1$$

$$|v(t, \mu)| \leq C(|\beta - h_2 \tilde{z}(t)| + \mu) \left(1 + e^{-\delta \frac{t}{\mu}}\right),$$

Hence, it follows that the solution  $z(t, \mu), y(t, \mu)$  does not tend to the solution  $\tilde{z}(t), \tilde{y}(t)$  of the unperturbed problem (37), (38).

Now, consider the unperturbed system

$$\begin{cases} A_1(t) \bar{z}' + B_1(t) \bar{z} + C_1(t) \bar{y} = F_1(t), \\ \bar{y}' + A_2(t) \bar{z}' + B_2(t) \bar{z} + C_2(t) \bar{y} = F_2(t) \end{cases} \quad (41)$$

with changed boundary conditions

$$\begin{aligned} h_1 \bar{z}(t) &= \alpha + \Delta_z, & h_2 \bar{z}(t) &= \beta + \Delta_J, \\ h_3 \bar{y}(t) &= \gamma + \Delta_y \end{aligned} \quad (42)$$

where  $\Delta_z$ ,  $\Delta_y$  and  $\Delta_J$  are initial jumps. The problem (41), (42) is called a changed unperturbed problem.

**Theorem 2.** Let conditions I-IV hold. Then for the difference between of the solutions of the original problem (1), (2) and changed unperturbed problem (41), (42) the following asymptotic estimates are valid as  $\mu \rightarrow 0$ :

$$\begin{aligned} |z^{(j)}(t, \mu) - \bar{z}^{(j)}(t)| &\leq C(|\Delta_J - a_1(0)\Delta_z| + \\ &+ |\Delta_y + A_2(0)\Delta_z| + \mu) \left(1 + \frac{1}{\mu^j} e^{-\frac{\delta t}{\mu}}\right), \quad j = 0, 1 \\ |y(t, \mu) - \bar{y}(t)| &\leq C(|\Delta_J - a_1(0)\Delta_z| + \\ &+ |\Delta_y + A_2(0)\Delta_z| + \mu) \left(1 + e^{-\frac{\delta t}{\mu}}\right), \end{aligned} \quad (43)$$

where  $C > 0$ ,  $\delta > 0$  – some constants independent of  $\mu$ .

**Proof.** For the functions  $u(t, \mu) = z(t, \mu) - \bar{z}(t)$ ,  $v(t, \mu) = y(t, \mu) - \bar{y}(t)$  we have the system (39) with boundary conditions

$$\begin{aligned} h_1 u(t, \mu) &= -\Delta_z, & h_2 u(t, \mu) &= -\Delta_J, \\ h_3 v(t, \mu) &= -\Delta_y \end{aligned} \quad (44)$$

Using estimates (31) to the problem (39), (44), we have

$$\begin{aligned} |u^{(j)}(t, \mu)| &\leq C(|\Delta_J - a_1(0)\Delta_z| + \\ &+ |\Delta_y + A_2(0)\Delta_z| + \mu) \left(1 + \frac{1}{\mu^j} e^{-\frac{\delta t}{\mu}}\right), \quad j = 0, 1 \\ |v(t, \mu)| &\leq C(|\Delta_J - a_1(0)\Delta_z| + \\ &+ |\Delta_y + A_2(0)\Delta_z| + \mu) \left(1 + e^{-\frac{\delta t}{\mu}}\right), \end{aligned}$$

This yields estimates (43). Theorem 2 is proved.

From Theorem 2 we have that the solution of the singularly perturbed BVP (1), (2) will tend to the solution of the changed unperturbed BVP (41), (42) under the following conditions:

$$\Delta_J = a_1(0)\Delta_z, \quad \Delta_y = -A_2(0)\Delta_z \quad (45)$$

Then the boundary conditions (42) in consideration of (45) take the form

$$\begin{aligned} h_1 \bar{z}(t) &= \alpha + \Delta_z, & h_2 \bar{z}(t) &= \beta + a_1(0)\Delta_z, \\ h_3 \bar{y}(t) &= \gamma - A_2(0)\Delta_z \end{aligned} \quad (46)$$

where  $\Delta_z$  – initial jump of the fast variable  $z(t, \mu)$ .

Thus, the solution  $z(t, \mu), y(t, \mu)$  of the singularly perturbed BVP (1), (2) as  $\mu \rightarrow 0$  approaches the solution  $\bar{z}(t), \bar{y}(t)$  of the changed unperturbed BVP (41), (46), i.e. passages to the limit take place:

$$\lim_{\mu \rightarrow 0} z^{(j)}(t, \mu) = \bar{z}^{(j)}(t), \quad i = 0, 1, \quad 0 < t \leq 1$$

$$\lim_{\mu \rightarrow 0} y(t, \mu) = \bar{y}(t), \quad 0 < t \leq 1.$$

## Conclusion

In this work, asymptotic estimates of the solution of an integral BVP for a singularly perturbed system of linear ordinary differential equations are obtained. The study has shown that the solution of the original singularly perturbed integral BVP does not tend to the solution of the usual unperturbed BVP. The presence of integral terms in the boundary conditions will significantly change the corresponding unperturbed problem. The solution of the original singularly perturbed integral BVP tends to the solution of the so-called changed unperturbed BVP is proved. However, the boundary conditions have changes: an initial jump of the fast variable appears. Thus, the changed unperturbed problem is presented as a problem with an additional parameter. Note that this modification of the degenerate BVP is associated with an infinitely large value of the first-order derivatives as the small parameter tends to zero. The results obtained allow us to construct asymptotic expansions of solutions of singularly perturbed nonlinear problems.

## Acknowledgement

The present work was partially supported by the Grant “Inertial neural networks with unpredictable fluctuations” (2020–2022) of the Committee of Science of the Ministry of Education and Science of the Republic of Kazakhstan (Grant No.AP08856170).

## References

1. Tihonov A.N., O zavisimosti reshenij differencial'nyh uravnenij ot malogo parametra // *Matematicheskij sbornik* 22(2) (1948): 193–204 (In Russian).
2. Wasow W., Singular perturbations of boundary value problems for nonlinear differential equations of the second order// *Comm. On Pure and Appl. Math.* 9 (1956): 93–113.
3. Pontryagin L.S. Asimptoticheskoe povedenie reshenij system differencial'nyh uravnenij s malym parametrom pri vysshih proizvodnyh. // *Izv. AN SSSR*, 21(31) (1957): 605-626 (In Russian).
4. Bogoliubov, N. and Mitropolskii, Y.A. Asymptotic methods in the theory of nonlinear oscillations // *Hindustan Publ. Corp., Delhi.* (1961):517.
5. Vishik M.I., Lyusternik L.A. Regulyarnoe vyrozhdeniei pograničnyj sloj dlya linejnyh differencial'nyh uravnenij s malym parametrom // *UMN.* 12(5) (1957): 3 – 122 (In Russian).
6. Vasil'eva A., Butuzov V. and Kalachev L. The boundary function method for singular perturbation problems// *ser. SIAM Studies in Applied Mathematics.* Philadephia: SIAM, 14 (1995):219, doi: 10.1137/1.9781611970784.
7. Lomov S. Introduction to the general theory of singular perturbations / Providence, RI: American Mathematical Society, (1992):375.
8. Imanaliev M.I. Asimptoticheskie metody v teorii singulyarno vozmushchennyh integro-differencial'nyh system / Frunze: Ilim, (1972): 356. (In Russian).
9. Vishik M.I., Lyusternik L.A. O nachal'nom skachke dlya nelinejnyh differencial'nyh uravnenij, sodержashchih malyj parametr // *Doklady AN SSSR.* 132(6) (1960): 1242–1245. (In Russian).
10. Kassymov K.A. Ob asimptotike resheniya zadachi Koshi s bol'shimi nachal'nymi usloviyami dlya nelinejnyh obyknovennyh differencial'nyh uravnenij, sodержashchih malyj parametr // *Uspekhi mat. nauk.* 17(5) (1962): 187– 188.(In Russian).
11. Kassymov K.A. Asymptotika resheniya zadachi s nashalnym skachkom dliya nelinejnyh system differencialnyx uravnenii s malym parametrom pri starshei proizvodnoi // *DAN SSSR.* – 189(5) 1969: 941-944.(In Russian).
12. Kassymov K.A. Asymptotika resheniya zadachi s nashalnym skachkom dliya nelinejnyh system differencialnyx uravnenii gyperbolicheskogo tipa s malym parametrom pri starshei proizvodnoi // *DAN SSSR*, 196(2) (1971): 274-277. (In Russian).
13. Abil'daev E.A., Kassymov K.A. Asimptoticheskie ocenki reshenij singulyarno vozmushchennyh kraevykh zadach s nachal'nymi skachkami dlya linejnyh differencial'nyh uravnenij // *Differencial'nye uravneniya*, 28(10) (1992): 1659–1668. (In Russian).
14. Kassymov K.A., Nurgabyly D.N. Asymptotic Behavior of Solutions of Linear Singularly Perturbed General Separated Boundary-Value Problems with Initial Jump // *Ukrainian Mathematical Journal.* 55(11) (2003): 1777-1792.
15. Dauylbaev M.K., Mirzakulova A.E. Asymptotic behavior of solutions of singular integro-differential equations // *Journal of Discontinuity, Nonlinearity, and Complexity*, 5(2) (2016): 147–154.
16. Akhmet M, Dauylbayev M.K., Mirzakulova A.E. A singularly perturbed differential equation with piecewise constant argument of generalized type // *Turkish Journal of Mathematics*, 42(4) (2018): 1680–1685.
17. Kassymov K.A., Tazhimuratov I.T., Sheriyazdan T.T. Nerazdelennaya kraevay zadacha dlya singulyarno vozmuchennoi systemy linejnyx differencialnyx uravnenii// *Vestnik KazGU, seriamatematika, mehanika I informatika* 21(2) (2000): 72-80.(In Russian).
18. Kassymov K.A., Sheriyazdan T.T. Asimptoticheskie resheniya nerazdelennykh kraevykh zadach dliya singulyarno vozmuchennoi systemy linejnyx differencialnyx uravnenii // *Almaty.* (2001): 110.(In Russian).

A.A. Issakhov , A.K. Manapova\* 

Kazakh-British technical university, Almaty, Kazakhstan

\*e-mail: manapova.a.k.math@gmail.com

## Numerical modeling of air flow inside the human nose cavity

**Abstract.** The complex structure of the human nasal cavity makes it difficult to study the flow of air in it, therefore, at present, mathematical and computer modeling is used for this purpose. These studies are relevant due to the development of inhalation methods for injections drugs into the nose, with the help of which surgery can be performed. Within the framework of the Navier-Stokes, temperature and concentration system of equations using the ANSYS Fluent application, a three-dimensional test calculation of the air flow in the human nasal cavity was carried out at various modes of inhalation, normal inhalation and during exercise. The laminar model was used to close the Navier-Stokes equations, and the SIMPLE method was used to perform the relationship between velocity and pressure. In the graphics package AutoCAD, a geometric three-dimensional model of the nasal cavity was built, reconstructed from images of the nose in coronary sections. As a result of numerical simulation, the fields of velocity, pressure, temperature and concentration were obtained. The obtained results were compared with the experimental data from [10] and the numerical results from [3]. The obtained results match with the experimental data. It was found that the inhaled air is heated and humidified to the state of the nasal tissue, the shells increase the rate of local transfer of heat and moisture by improving mixing and maintaining thin boundary layers, the capacity of a healthy nose exceeds the requirements necessary for conditioning the inhaled air under normal breathing conditions.

**Key words:** system of equations Navier-Stokes, anatomical model of the nose, coronary planes, flow structure, method SIMPLE, inhaled air conditioning.

### Introduction

The nose is located at the beginning of the human respiratory tract and plays an important role in transporting air to the lungs, in purifying the air, in delivering drugs to the body during inhalation, etc. Physical deficiencies in the nasal cavity make it difficult to perform these functions. For treatment and surgery, in order to avoid unwanted complications, it is necessary to have a good knowledge of the structure of the nasal cavity and the structure of the movement of the inhaled gas.

Mathematical modeling of the air flow in the human nasal cavity can investigate the structure of the flow, which cannot be detected by modern instrumental methods, makes it possible to predict the results of real surgical operations, and can also help in determining the method of drug delivery during inhalation.

Studies of the flow of air in the human nasal cavity have been conducted since the 1990s, to which the works of the authors [1-6], etc. The first calculations were carried out only for one part of the

nasal cavity, where the computational grid did not reach 100,000 cells [3, 4, 7]. In later works, one can see the results of the study of both sides of the nasal cavity, where the calculations were carried out for several 10 times larger numbers of grid cells.

The air flow in the human nasal cavity has been experimentally studied for decades in works [8-16].

In addition, the authors of [3, 17, 18-21] carried out an analysis of fluid dynamics (CFD) of the human nasal cavity, confirming the main experimental observations.

The first native publication on this topic appeared in 2016 [22], where a two-dimensional computational study of transport phenomena in model cross-sections of the nasal cavity of a normal human nose was investigated on the basis of a two-dimensional incompressible system of Navier-Stokes equations. In the mentioned work, the methods of finite volumes and projection are applied. Research has shown that a normal nose can maintain balance even under extreme conditions.

In [23], studies of airflow transfer in a nasal cavity model for normal inspiratory rate in various

environmental conditions were carried out, where numerical results showed that during normal breathing, the human nose copes with the metabolism of heat and relative humidity in order to balance the alveolar conditions within.

In [24], numerical methods based on an anatomically accurate model of the nose were tested. It was found that the laminar model achieves good similarity with experimental results under calm breathing conditions (180 ml / s) and performs better than the turbulent RANS model. The turbulent RANS models gave more accurate predictions for the increase in respiration rate, but the LES and DNS results were better. As expected, the LES and DNS can provide accurate forecasts of nasal airflow in all conditions, but their computational costs are 100 times greater. Among all the tested RANS models, the standard model most closely matches the experimental values in terms of the velocity profile and turbulence intensity.

For more efficient computation of numerical simulation of air transport in the human nasal cavity, parallel computing technologies are used. In [25], a two-dimensional numerical simulation of air transport in model sections of the nasal cavity by the projection method was carried out, where the algorithm is parallelized using geometric decompositions. As a result, the effectiveness of various methods of decomposition of the computational domain was determined.

### Mathematical model

Mathematical model is

$$\begin{cases} \nabla \cdot U = 0 \\ \frac{\partial U}{\partial t} + (U \cdot \nabla)U = -\frac{1}{\rho} \nabla P + \nu \nabla^2 U \\ \frac{\partial T}{\partial t} + (U \cdot \nabla)T = -\frac{k}{\rho c_p} \nabla^2 T \\ \frac{\partial C}{\partial t} + (U \cdot \nabla)C = -D \nabla^2 C \end{cases} \quad (1)$$

where  $U$  – velocity vector,  $T$  – temperature,  $C$  – concentration,  $t$  – time,  $x, y, z$  – spatial coordinates,  $\rho$  – density,  $k$  – thermal diffusivity,  $c_p$  – specific heat,  $\nu$  – kinematic viscosity,  $D$  –

molecular diffusion coefficient,  $\nabla^2$  – Laplacian operator.

Initial conditions:  $u_{t=0} = v_{t=0} = w_{t=0} = 0$ ,  $T_{t=0} = 32^\circ\text{C}$ ,  $C_{t=0} = 0,0235 \text{ kgH}_2\text{O}/\text{m}^3$ .

Input boundary conditions for speed: for normal breathing  $u = v = w = 1 \text{ m/c}$  and for breathing during the exercise  $u = v = w = 2.5 \text{ m/c}$ .

Boundary conditions on the inlet for temperature and concentration:  $T_{t=0} = 25^\circ\text{C}$ ,  $C_{t=0} = 0,0047 \text{ kgH}_2\text{O}/\text{m}^3$ .

The boundary conditions for the velocity at the walls of the nasal cavity and turbinate are specified as no slip conditions.

Boundary conditions on the walls for temperature and concentration:  $T_{wall} = 37^\circ\text{C}$ ,  $C_{wall} = 0,0438 \text{ kgH}_2\text{O}/\text{m}^3$ .

The ANSYS FLUENT application package is used for numerical modelling. The laminar model was used to close equations (1), and the SIMPLE algorithm was used to relate pressure and velocity.

56 forms of the transverse coronary planes of the nasal cavity obtained from [26] and were digitized, restored in the graphic program Autocad. Final result was constructed as a geometric model of the nasal cavity of a real person (Figure 1).

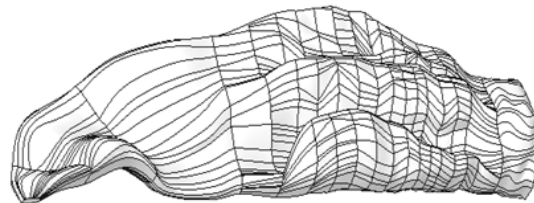
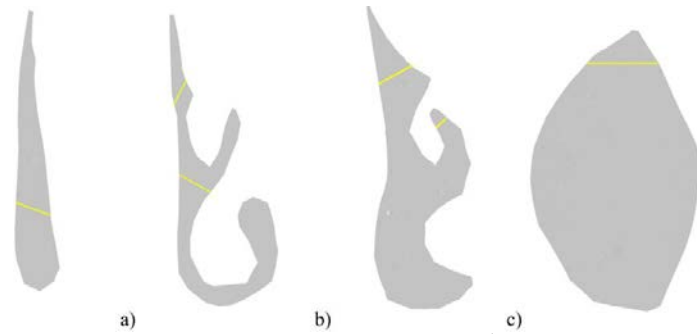


Figure 1 – Constructed 3D model of the nasal cavity

The right side of the nasal cavity was used during calculation, in which the  $Y$  axis is directed vertically upward, the  $X$  axis is directed from the entrance to the nasopharynx along the main direction of flow. Computational grid consists of 692 158 elements.

Computational fluid dynamics (CFD) analysis of nasal function is studied with the article [3]. The numerical results were compared with the detailed experimentally measured velocity profiles from [10] and the numerical results from [3].

The results were obtained in the indicated lines of 4<sup>th</sup>, 6<sup>th</sup>, 8<sup>th</sup>, 9<sup>th</sup> planes (Figure 2).



**Figure 2** – a) a line with a dimension of 2.66 mm in 4<sup>th</sup> plane; b) – lines with dimensions 1.42 mm and 1.81 mm in 6<sup>th</sup> plane; c) – lines with dimensions 2.26 mm and 2.29 mm 8<sup>th</sup> plane; d) line with a size of 3.28 mm in 9<sup>th</sup> plane

**Numerical results**

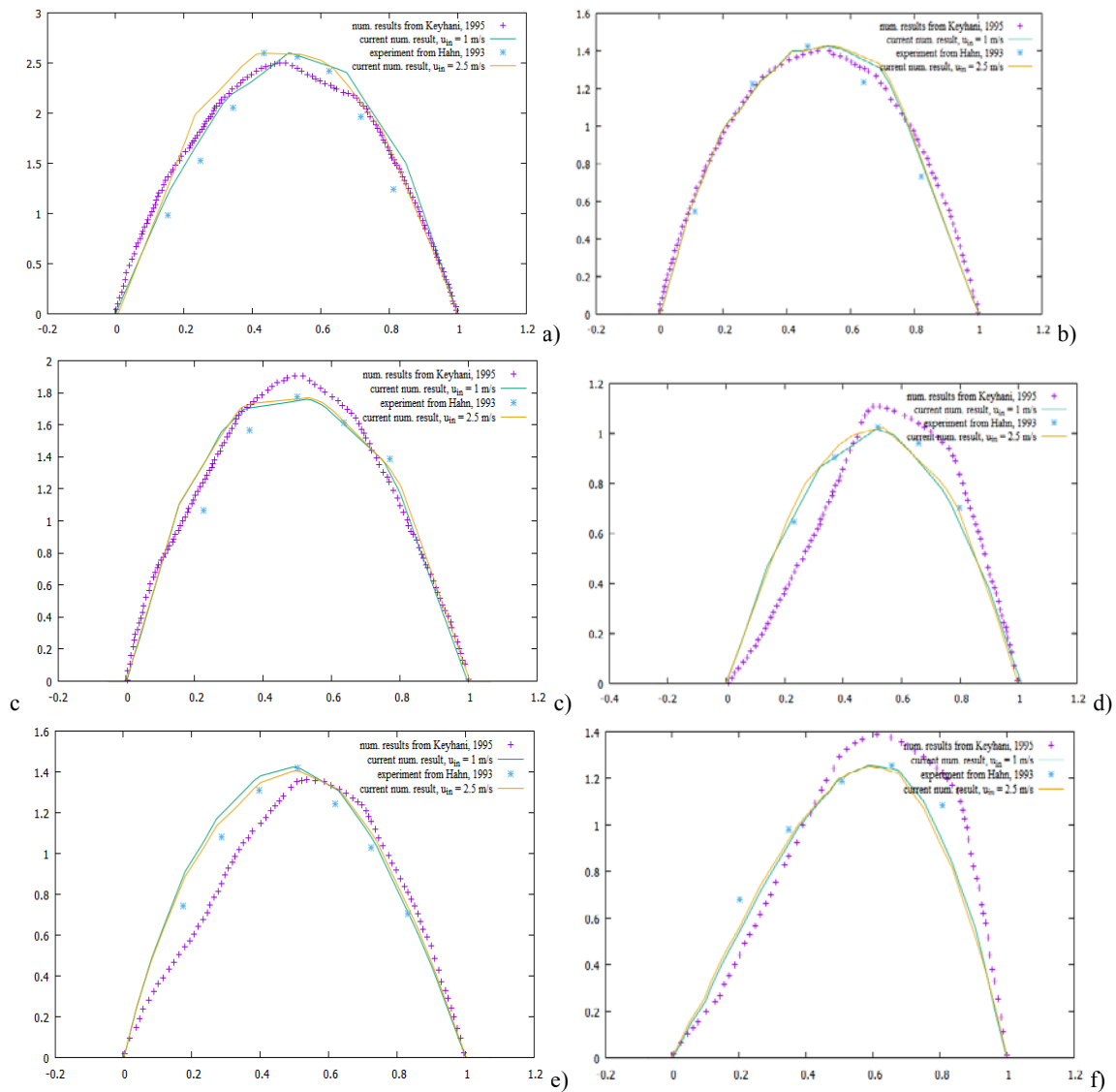


**Figure 3** – a) Velocity profiles U in 4<sup>th</sup> plane in line 2.66; b) Velocity profiles U in 6<sup>th</sup> plane in line 1.42; c) Velocity profiles U in 6<sup>th</sup> plane in line 1.81; d) Velocity profiles U in 8<sup>th</sup> plane in line 2.26; e) Velocity profiles U in 8<sup>th</sup> plane in line 2.29; f) Velocity profiles U in 9<sup>th</sup> plane in line 3.28

The results of the current numerical simulation are in good agreement with the experimental data from [10], as shown in Figures 3 (a-f). The profiles were dimensioned for maximum speed. Dimensionless distance was from the lateral to the medial sides of the airways.

Numerical results match with experimental measurements less than 20 percent at the most comparison locations. More accurate agreement was

obtained at many points in the model. The difference between the results can be attributed to different sources of numerical and experimental errors.

In figure 4 velocity contours show the appearance of vortices in the vicinity of the turbinate itself.

In figure 5 due to air heating, the temperature increases by 37°C.

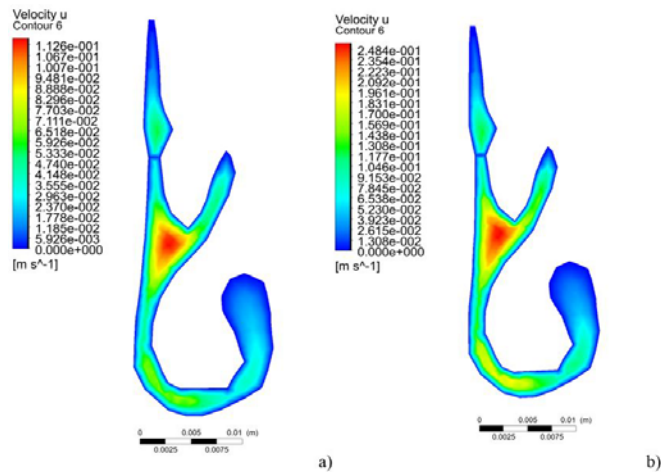


Figure 4 – Velocity contours in cross-section 6 with inlet velocities a – 1 m/s and b – 2,5 m/s

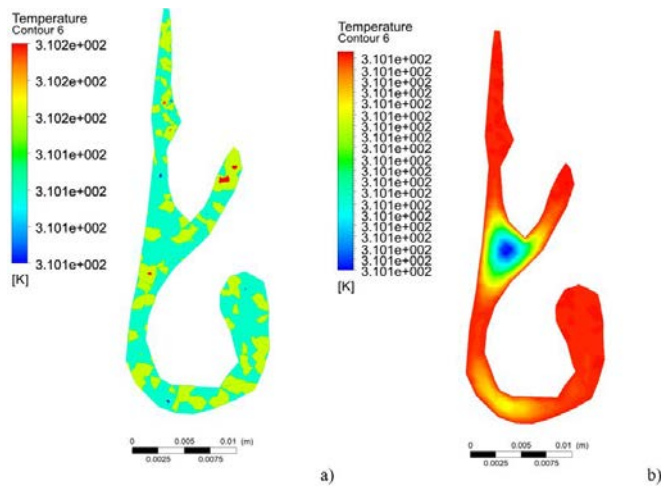
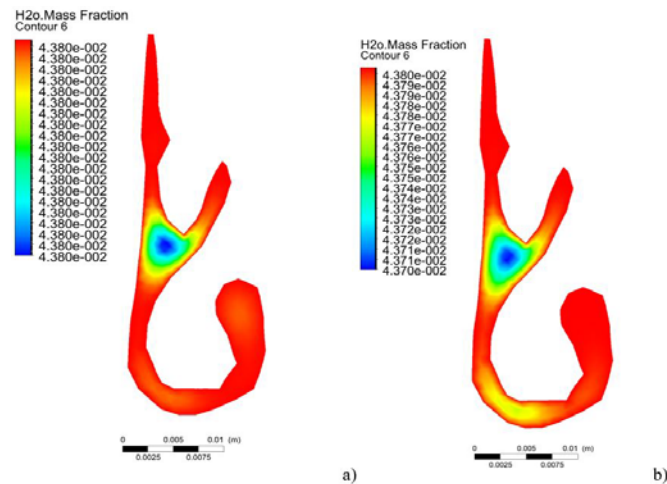


Figure 5 – Temperature contours in cross-section 6 with inlet velocities a – 1 m/s and b – 2,5 m/s



**Figure 6** – Concentration contours in cross-section 6 with inlet velocities  
a – 1 m/s and b – 2,5 m/s

In the vicinity of the shell, moisture increases due to the narrowing of the nasal cavity. In figure 6 moisture concentration reaches  $0.438 \text{ kgH}_2\text{O} / \text{m}^3$ .

### Conclusion

A three-dimensional numerical simulation of the nasal cavity models has been carried out due to lack of studying problems of air transport phenomena in it. Inhaled air is heated and humidified to the state of the nasal tissue. The shells increase the rate of local heat and moisture transfer by improving mixing and maintaining thin boundary layers. During an average inhalation (when the speed is maximum), a rapidly moving air core dominates in the flow of inhaled air, and as a result, the instantaneous heat and mass exchange of the inhaled air is significantly reduced.

The nose can handle a range of extreme conditions. However, impaired circulation or surface moisture can reduce the rate of heat or moisture flows into the inhaled air. The capacity of a healthy nose exceeds the capacity required for conditioning the inhaled air under normal breathing conditions. As a consequence, it can be effective during heavy breathing and variety of entry conditions, including a scrubbing process to remove toxic gases and particles.

In future studies, it will be necessary to improve the detailed description of the processes' dynamics of heat transfer, water and soluble gas on the surface of the mucous membrane, especially in the region of the turbinate.

### References

- 1 Garcia G.J., Bailie N.A., Martins D.A., Kimbell J.S. "Atrophic rhinitis: A CFD study of air conditioning in the nasal cavity." *Journal of Applied Physiology*. 103 (2007): 1082–1092.
- 2 Hörschler I., Schröder W., Meinke M. "Numerical analysis of the impact of the nose geometry on the flow structure. Part II: Nasal valve and lower turbinate." *Computational Fluid Dynamics Journal*. 16 (2008): 243–260.
- 3 Keyhani K., Scherer P.W., Mozell M.M. "Numerical simulation of airflow in the human nasal cavity." *J. Biomech. Engng.* 117 (1995): 429–441.
- 4 Lindemann J., Keck T., Wiesmiller K., Sander B., Brambs H.J., Rettinger G., Pless D. "A numerical simulation of intranasal air temperature during inspiration." *The Laryngoscope*. 114 (2004): 1037–1041.
- 5 Rhee J.S., Cannon D.E., Frank D.O., Kimbell J.S. "Role of virtual surgery in preoperative planning. assessing the individual components of functional nasal airway surgery." *Arch. Facial. Plast. Surg.* 14 (2012): 354–359.
- 6 Segal R.A., Kepler G.M., Kimbell J.S. "Effect of differences in nasal anatomy on airflow distribution: a comparison of four individuals at rest." *Annals of Biomedical Engineering*. 36 (2008): 1870–1882.
- 7 Wen J., Inthavong K., Tian Z.F., Tu J.J., Xue C.L., Li C.G. "Airflow pattern in both sides of a realistic human nasal cavity for laminar and

turbulent conditions.” *Proceedings of 16th Australasian Fluid Mechanics Conference*. Gold Coast, (2009): 68–74.

8 Churchill S.E., Shackelford L.L., Georgi J.N., Black M.T. “Morphological variation and airflow dynamics in the human nose.” *American Journal of Human Biology*. 16 (2004): 625–638.

9 Girardin M., Bilgen E., Arbour P. “Experimental study of velocity fields in a human nasal fossa by laser anemometry.” *Annals of Otolaryngology, Rhinology and Laryngology*. 92 (1983): 231–236.

10 Hahn I., Schere P.W., Mozell M.M. (1993). “Velocity profiles measured for airflow through a large-scale model of the human nasal cavity.” *Journal of Applied Physiology*. 75 (1993): 2273–2287.

11 Hornung D.E., Leopold D.A., Youngentob S.L., Sheehe P.R., Gagne G.M., Thomas F.D. “Airflow patterns in a human nasal model.” *Archives of Otolaryngology—Head and Neck Surgery*. 113 (1987): 169–172.

12 Kelly J.T., Prasad A.K., Wexler A.S. “Detail flow patterns in the nasal cavity.” *Journal of Applied Physiology*. 89 (2000): 323–337.

13 Kim S.K., Chung S.K. (2004). “An investigation on airflow in disordered nasal cavity and its corrected models by tomographic PIV.” *Measurement Science and Technology*. 14 (2004): 1090–1096.

14 Park K.I., Brucker C., Limberg W. “Experimental study of velocity fields in a model of human nasal cavity by DPIV.” In B. Ruck, A. Leder, & D. Dopheide, *Laser anemometry advances and applications: Proceedings of the seventh international conference, University of Karlsruhe, Karlsruhe, Germany*. (1997).

15 Schreck S., Sullivan K.J., Ho C.M., Chang H. K. “Correlations between flow resistance and geometry in a model of the human nose.” *Journal of Applied Physiology*. 75 (1993): 1767–1775.

16 Swift D.L., Proctor D.F. “Access of air to the respiratory tract.” In J. D. Brain, D. F. Proctor, L. M. Reid, *Respiratory defense mechanisms: Part I*. (1977): 63–93.

17 Subramaniam R.P., Richardson R.B., Morgan K.T., Kimbell J.S. “Computational fluid dynamics simulations of inspiratory airflow in the human nose and nasopharynx.” *Inhalation Toxicology*. 10 (1998): 91–120.

18 Horchler I., Meinke M., Schröder W. “Numerical simulation of the flow field in a model of the nasal cavity.” *Computers and Fluids*. 32 (2003): 39–45.

19 Weinhold I., Mlynski G. “Numerical simulation of airflow in the human nose.” *European Archives of Otorhinolaryngology*. 261 (2004): 452–455.

20 Shi H., Kleinstreuer C., Zhanga Zh. “Modeling of inertial particle transport and deposition in human nasal cavities with wall roughness.” *Aerosol Science*. 38 (2007): 398–419.

21 Kleinstreuer C., Zhang Z. (2003). “Laminar-to-turbulent fluid-particle flows in a human airway model.” *International Journal of Multiphase Flow*. 29 (2003): 271–289.

22 Issakhov A., Yessenkozha A.M. “Mathematical modelling of air flow in the human respiratory system.” *International Journal of Mathematics and Physics*. 27 (2016): 27–32.

23 Issakhov A., Zhandaulet Y., Abylkassymova A., Issakhov A. “A numerical simulation of air flow in the human respiratory system for various environmental conditions.” *Theoretical Biology and Medical Modelling*. 18 (2021).

24 Li Ch., Jiang J., Dong H., Zhao K. “Computational modeling and validation of human nasal airflow under various breathing conditions.” *Journal of Biomechanics*. <http://dx.doi.org/10.1016/j.jbiomech.2017.08.031>

25 Issakhov A., Abylkassymova A. “Application of parallel computing technologies for numerical simulation of air transport in the human nasal cavity.” *Springer international publishing, Innovative computing, optimization and its application*. (2018).

26 Liu Y., Johnson M. R., Matida E. A., Kherani S., and Marsan J. “Creation of a standardized geometry of the human nasal cavity” *J Appl Physiol*. 106 (2009): 784–795.

S.D. Maussumbekova  A. Duysenali\* Al-Farabi Kazakh National University  
\*e-mail: [duisenali\\_akzholl@live.kaznu.kz](mailto:duisenali_akzholl@live.kaznu.kz)

## Numerical simulation of boiling liquid outflows process

**Abstract.** Computational algorithm was developed based on the well-known ANSYS Fluent software package for studying unsteady wave outflow of a saturated liquid from high-pressure pipelines during emergency depressurization. The unsteady processes of the outflow of liquid, boiling as a result of depressurization of high-pressure vessels, have been investigated. The system of equations for the conservation of mass, momentum, and energy in a two-dimensional coordinate system is used in order to create mathematical model this process. The features of the formation of jets of boiling liquid at various equilibrium initial states of water in a high-pressure vessel under conditions close to the experiments carried out by the authors [10] have been studied. The spatial distributions of pressure, temperature and velocity of the forming jet are obtained. Numerical results have shown that, over time, the character of the velocity distribution acquires a conical shape. With an increase in the initial temperature and pressure, this distribution is preserved, and the opening angle increases. The results are in qualitative agreement with the experimental data.

**Key words:** outflows of boiling liquid, mathematical and numerical modeling, homogeneous mixture, depressurization of a pressure vessel.

### Intruduction

The relevance of studies of the wave process of the efflux of a boiling coolant is due to the increasing requirements for ensuring the safety of modern power plants in emergency operating conditions. Establishing the laws of changing the parameters of the coolant in time in high-pressure circuits during sudden depressurization is necessary for calculating additional loads and extreme temperatures in the structural elements of the circuits, for designing devices for localizing the consequences of an accident, etc. In engineering practice, the calculation of the emergency outflow of a high-temperature coolant is usually carried out within the framework of quasi-stationary methods [1-4].

An experimental study of the dynamics of a superheated liquid from high-pressure chambers was carried out in [5, 6]. Numerical modeling of the process of depressurization of a pipeline with a hot coolant on the basis of a homogeneous model was carried out in [7]. On the basis of experiments from [5 non-stationary processes of efflux of boiling water in a one-dimensional formulation were numerically investigated in [8]. The authors generalized the two-phase model of the boiling steam-water mixture for the two-dimensional case with axial symmetry in [9,10]. The features of the formation of jets of a

boiling liquid were studied at various values of the initial saturation parameters close to the thermodynamic critical point.

Numerical modeling of the process of formation of a jet of a boiling coolant taking into account the nonequilibrium of the steam-water mixture near the rupture boundary is presented in [8]. The authors had used the model of an ideal compressible fluid in the quasi-stationary approximation in order to solve the problem. The experiments on explosive boiling up of water jets as a result of their outflow through a thin cylindrical nozzle from high-pressure vessels are analyzed in [10].

The study of the motion of heterogeneous mixtures taking into account the initial structure of the mixture and the physical properties of the phases is associated with the use of new parameters and the solution of equations that are more complicated than those with which one has to deal with in the mechanics of single-phase (homogeneous) media. In addition, a detailed description of intraphase and interphase interactions in heterogeneous media is extremely difficult. Rational schematization is especially necessary here to obtain observable results and their understanding.

The works [5] – [11] are devoted to the issues of the expiration of two-phase flows. High values of temperature and pressure in containers with water

during depressurization lead to its rapid expansion and boiling. The initial, unsteady stage of the efflux of a boiling liquid is of particular interest both in theoretical and experimental terms, since it is characterized by significant metastable wave processes.

The problem of emergency depressurization of systems with a liquid coolant at high pressure is far from well understood. This also applies to the mechanical side of the phenomenon of wave outflow of a boiling liquid, accompanied by intense phase transformations and restructuring of the structure of the vapor-liquid flow. It is advisable to carry out theoretical research in the direction of analyzing the physics of the process, constructing its mathematical models and developing methods for numerical integration that describe the process of equations.

### Formulation of the problem

The main assumptions were used in the mathematical formulation of the problem like:

- the movement of the medium is two-dimensional, the influence of the design features of the pipelines on the outflow process can be neglected;
- the temperature inside the pipe is identically equal to the saturation temperature at a given pressure.

The equations of state of this medium are constructed according to the known equations of state of the phases using the usual assumption about the additivity of thermodynamic functions:

$$\begin{aligned} i(x, p) &= (1 - x)i_1(p) + xi_2(p) = \\ &= i_1(p) + xl(p); \\ V(p) &= (1 - x)V_1(p) + xV_2(p), \end{aligned} \quad (1)$$

there  $i$  и  $V$  – specific enthalpy and volume of the mixture;  $l$  – specific heat of vaporization; indices 1 and 2 mark the parameters of liquid and vapor, respectively. The equations of conservation of mass and momentum and the equation of heat inflow for two-dimensional unsteady motion of an equilibrium vapor-liquid mixture in a channel of constant cross-section have the following form:

$$\frac{d\rho}{dt} + \rho \frac{\partial v_x}{\partial x} + \rho \frac{\partial v_y}{\partial y} = 0, \quad (2)$$

$$\rho \frac{dv_x}{dt} = -\frac{\partial p}{\partial x}, \quad \rho \frac{dv_y}{dt} = -\frac{\partial p}{\partial y} \quad (3)$$

$$\rho \frac{de}{dt} + p \operatorname{div} v = 0 \quad (4)$$

Let there be a cylindrical vessel (a piece of pipeline) of constant cross-section with a length  $L$ , filled with a saturated liquid with pressure  $p_0$  and temperature  $T_s(p_0)$ . At the moment of time  $t = 0$ , a sudden depressurization of the right end occurs (rupture of the diaphragm). The liquid in the outlet section boils, the forming vapor-liquid mixture starts to move and flows out with a pressure  $p_c$ , much less than the pressure  $p_0$ . A rarefaction wave will go through the liquid inside the pipe. The problem of calculating a non-stationary process accompanying a sudden depressurization of a pipeline is to determine the laws of change in pressure, velocity, steam content and temperatures in time in various sections of the pipe. Mathematically, it is a mixed problem for the system of partial differential equations (2) – (4) with the following initial and boundary conditions:

$$\begin{aligned} \vartheta(z, 0) &= 0, \quad p(z, 0) = p_0, \\ T(z, 0) &= T_s(p_0) \\ \vartheta(0, t) &= 0, \quad p(L, t) = p_c \end{aligned} \quad (5)$$

### Numerical solution technique

ANSYS software was used for solving of problem. At first stage, geometry of object was created with the help of built-in DesignModeler editor. Mesh editor allows sampling computational domain. Transition to Setup editor allows setting initial and boundary conditions of task, and choose solution method. (Figure 1).

The geometry of the computational domain is a rectangular section of the pipe, which corresponds to the following dimensions: the part of the section where the boiling liquid is located: length – 7 cm, width – 1 cm, and the medium – air: length. – 14 cm, width – 2 cm, the full computational domain is rectangular with length – 21 cm and height 3 cm. The algorithm for creating the geometry and mesh of the problem, setting the boundary conditions in the Ansys software are shown in Figures 2-3.

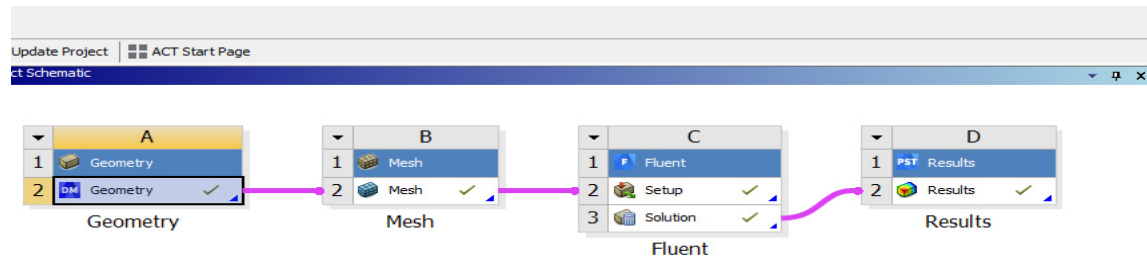


Figure 1 – Ansys project

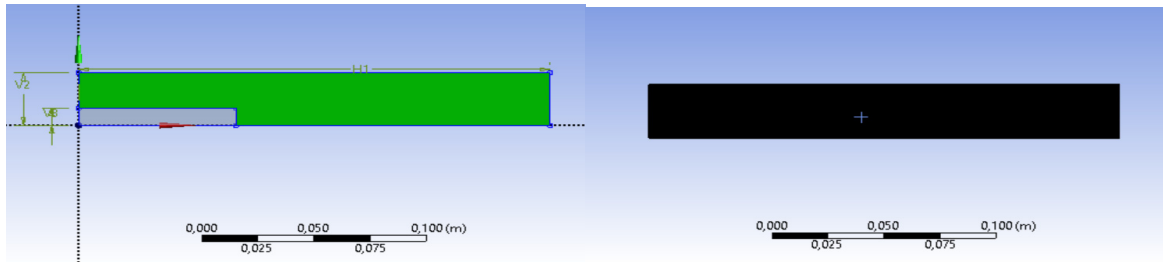
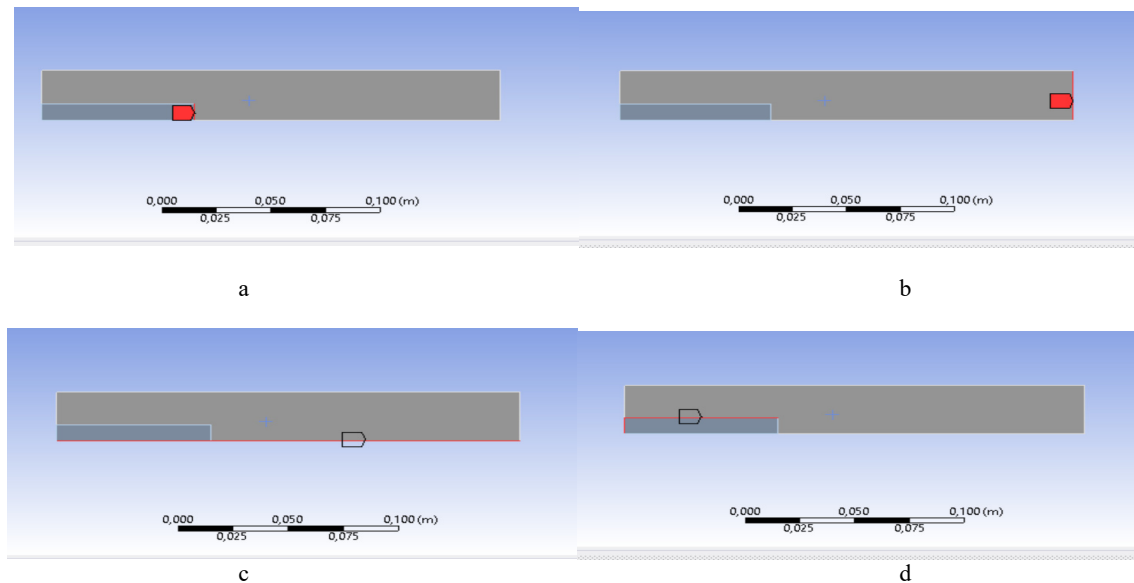


Figure 2 – Geometry of the computational domain

Figure 3 – Boundaries of the computational domain:  
Inlet (a); Outlet (b); Axis (c); Pipe Wall (d)

The boundary conditions are set as follows: the air velocity in the free volume is  $0.001 \text{ m/s}$ . The relative pressure at the outlet from the pipe is  $0 \text{ Pa}$ . To obtain a solution, we choose a paired calculation scheme that combines pressure and speed.

### Results and analysis of numerical calculations

We investigated the dynamics of the vapor-liquid mixture during depressurization of the pipe under

various initial conditions inside the pipe. The following values were set as the initial values for the pressure and temperature inside the pipe: A:  $p = 246 \text{ kPa}$ ,  $T = 400 \text{ K}$ ; B:  $p = 475 \text{ kPa}$ ,  $T = 423 \text{ K}$ ; C:  $p = 1553 \text{ kPa}$ ,  $T = 473 \text{ K}$  and  $T = 300 \text{ K}$  in outside zone.

The pressure and velocity profiles are shown in figure 4 for various pipe sections after depressurization. Numerical results lead that the mixture instantly sets in motion: the speed increases, the pressure

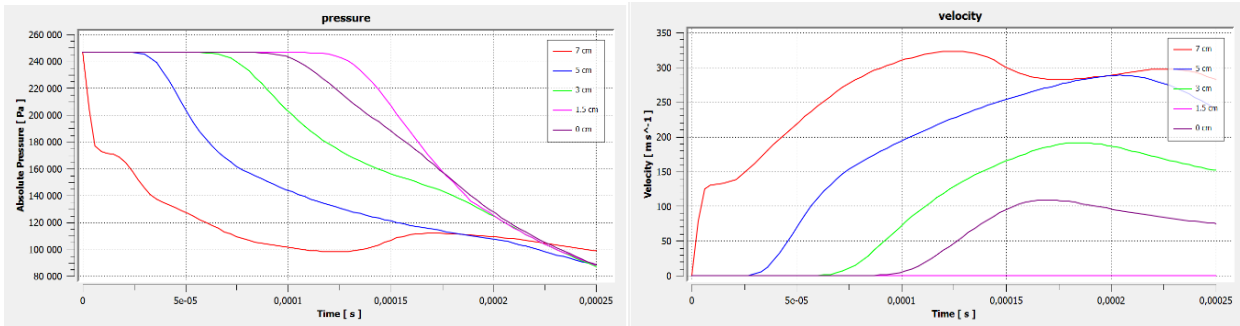
drops. The closer the discontinuity point is (7 cm), the more intense the pressure drop, which is consistent with the results of [8].

The pressure contours are shown in Figure 5 at different times with initial values  $p = 246 \text{ кПа}$ ,  $T = 400\text{K}$ . As a result of depressurization, a fast unloading wave propagates inside the pipe, and a spatial outflow of the boiling flow begins, in which a radial expansion of the jet is observed due to vaporization.

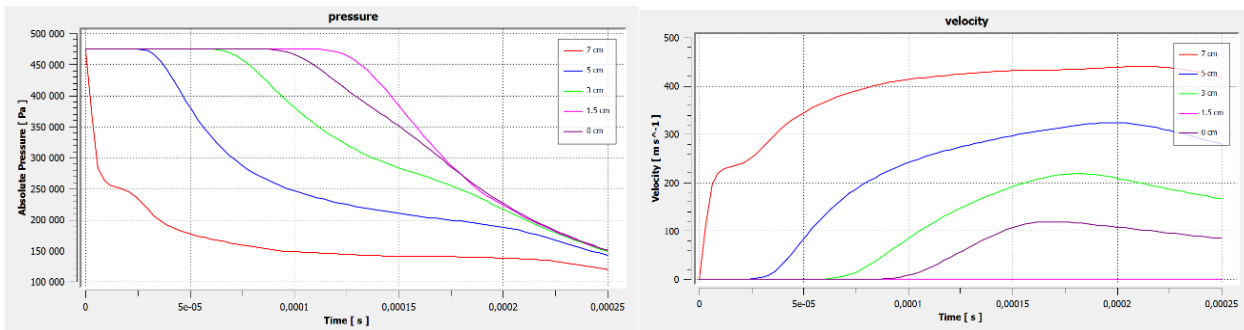
The velocity profiles acquire a characteristic conical shape with changing time.

The velocity profiles acquire a characteristic conical shape with changing time.

A



B



C

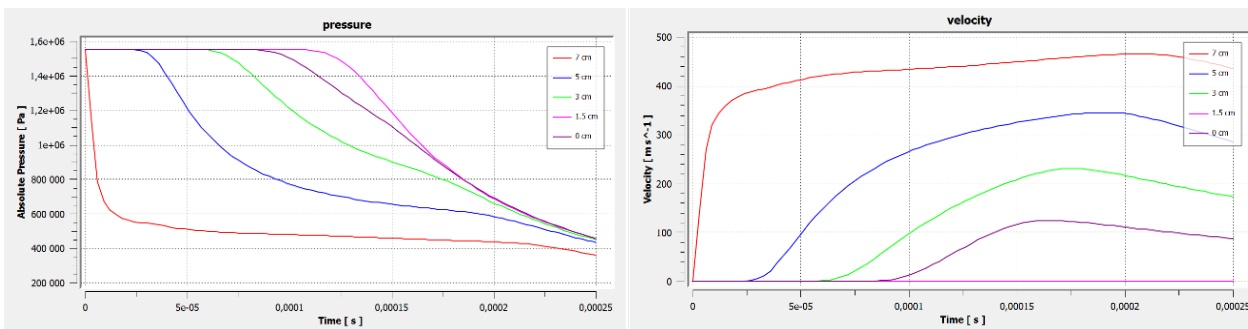


**Figure 4** – Distribution of pressure (left) and velocity (right) under different initial conditions in the pipe:

A:  $p = 246 \text{ кПа}$ ,  $T = 400\text{K}$ ;

B:  $p = 475 \text{ кПа}$ ,  $T = 423\text{K}$ ;

C:  $p = 1553 \text{ кПа}$ ,  $T = 473\text{K}$ .

The stream of boiling water also has a conical shape, and the opening angle increases with increasing in the initial temperature and pressure in

the saturation state to 423 K and 475 kPa, respectively (Figure 6) in comparison with the previous version.

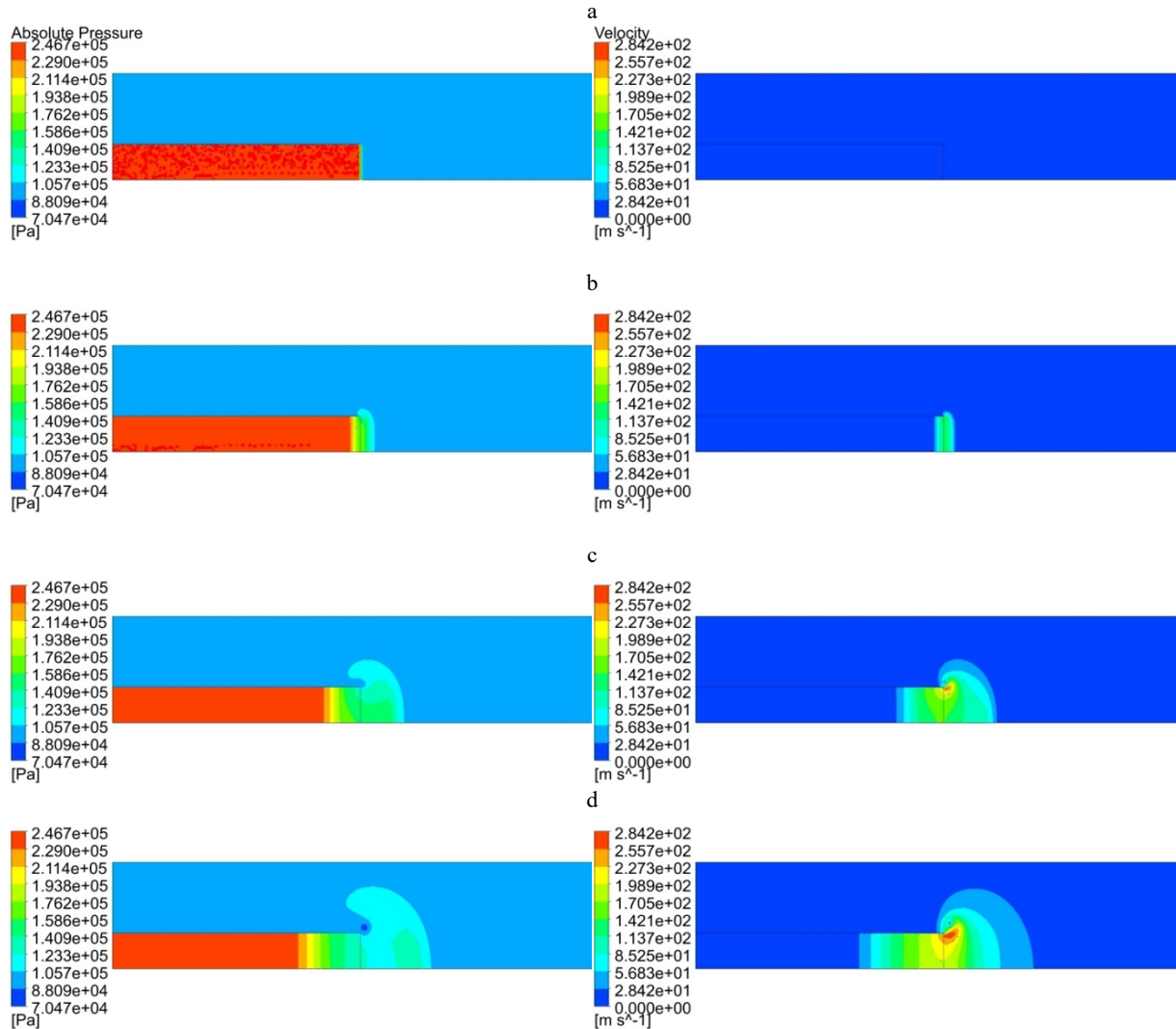


**Figure 5** – Pressure (left) and velocity (right) circuits at different points in time:  
 $t = 0$  c (a);  $t = 1.5e - 5$  c (b);  $t = 2.4e - 5$  c (c);  $t = 4.2e - 5$  c (d)  
 for  $p = 246.7$  kPa,  $T = 400K$ ;

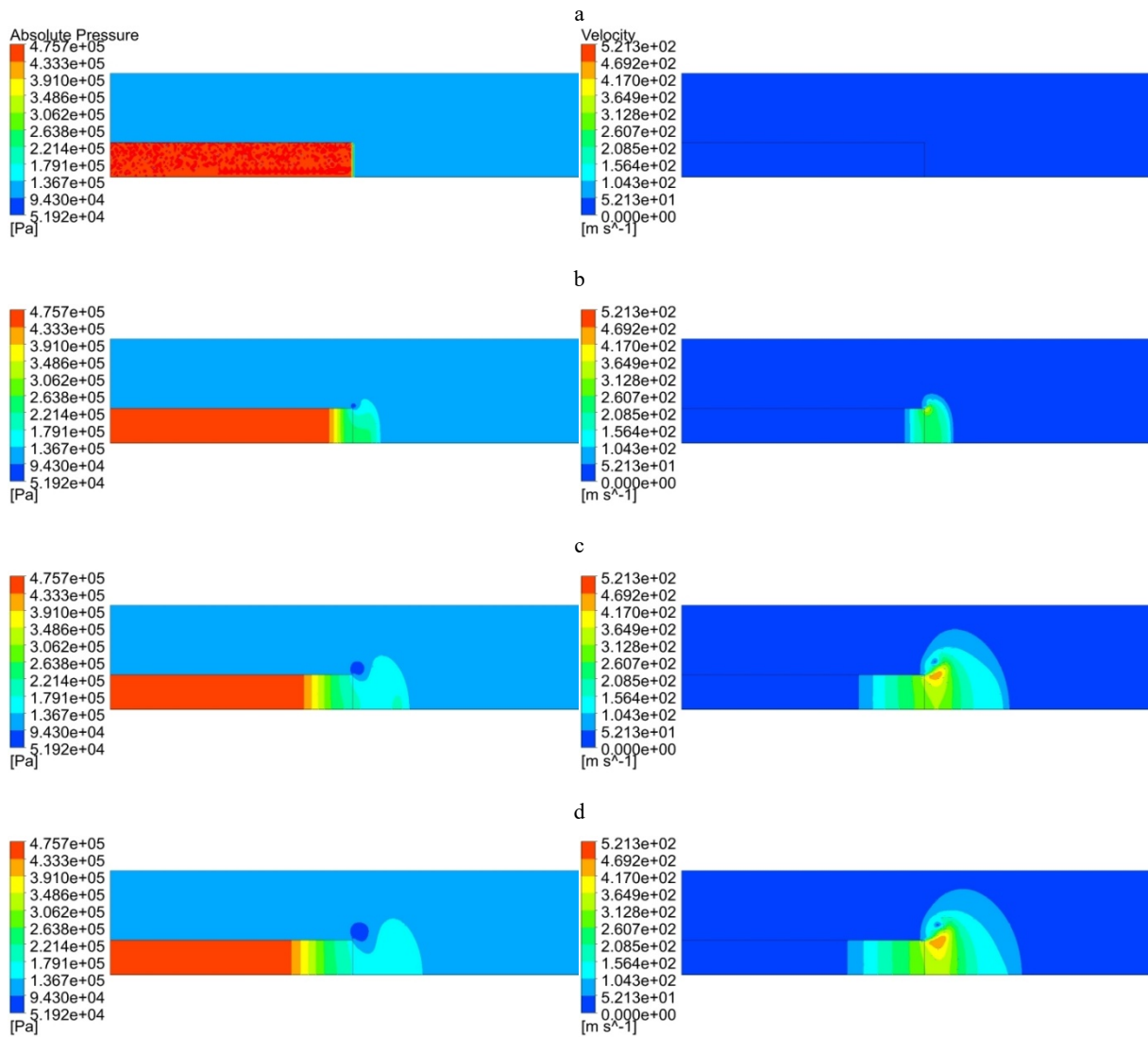


**Figure 6** – Pressure (left) and velocity (right) circuits  
 at different points in time:  
 $t = 0$  c (a);  $t = 1.5 \cdot 10^{-5}$  c (b);  $t = 2.4 \cdot 10^{-5}$  c (c);  $t = 4.2 \cdot 10^{-5}$  c (d)  
 for  $p = 475 \text{ kPa}$ ,  $T = 423 \text{ K}$

Calculations have shown that a further increase in temperature to 473 K leads to a significant increase in speed, but the jet opening angle does not exceed 70 degrees (Figure 7). This result is consistent with the

experimental data from [10], in which, up to the indicated temperatures, the jet also had a conical shape with an increase in the opening angle with an increase in the initial temperature.

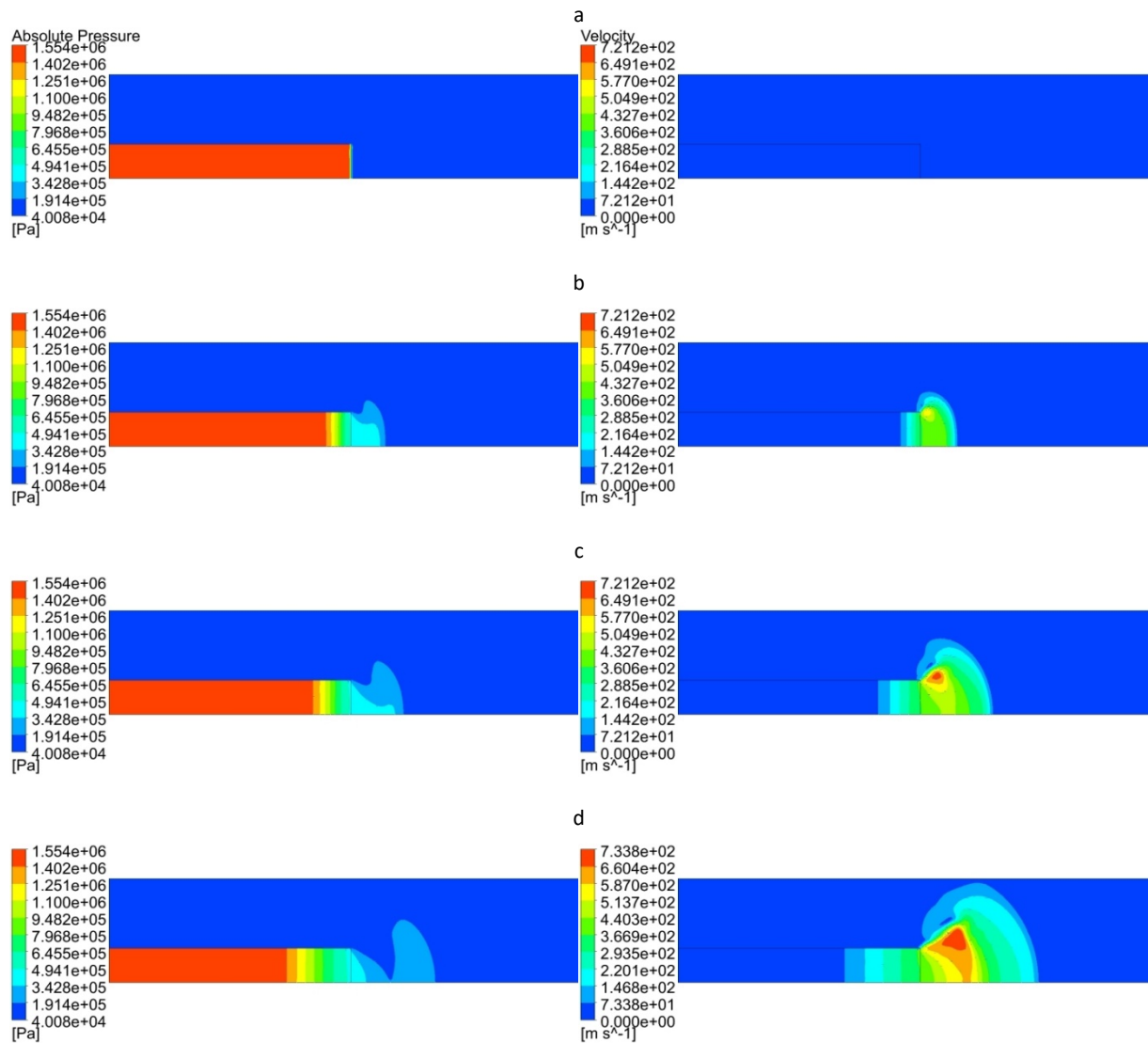


**Figure 7** – Pressure (left) and velocity (right) contours at different points in time:  $t = 0$  c (a);  $t = 1.5 \cdot 10^{-5}$  c (b);  $t = 2.4 \cdot 10^{-5}$  c (c);  $t = 4.2 \cdot 10^{-5}$  c (d) for  $p = 1553 \text{ kPa}$ ,  $T = 473 \text{ K}$ .

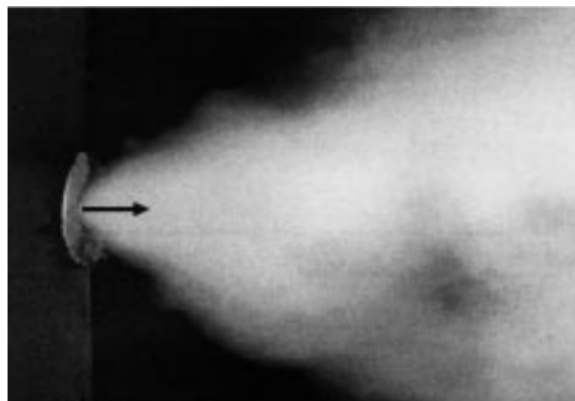


**Figure 8** – Pressure outlet from the boiling liquid chamber at a temperature of 473K [10]

The photograph which taken from [9] has been shown in Figure 8, where an experimental jet of boiling liquid can be seen at an initial saturation temperature of 473K. A comparative analysis of the photograph and the results of numerical experiments shows their qualitative agreement.

### Conclusion

In this paper, we propose a model for the dynamics of a two-dimensional vapor-liquid mixture in the case of a sudden depressurization of a high-pressure pipe. The numerical experiments of the model was carried out on the basis of the ANSYS software package. The features of the formation of jets of boiling liquid at various equilibrium initial states of water in a high-pressure vessel under conditions close to the experiments carried out by the authors [10] have been studied. The spatial distributions of pressure, velocity and temperature fields are obtained. The results of numerical experiments have shown that at initial temperatures of the state of water saturation below 473 K, the jet has a conical shape; a further increase in the initial saturation temperature leads to the formation of the initial stage of the jet breakup mode, which is in qualitative agreement with the experimental results of [10]. The results of this work can be used in processing the corresponding experimental data and creating methods for calculating the processes accompanying emergency depressurization of complex multi-element high-pressure systems.

### References

- 1 Ivandaev A.I., Gubaidulin A.A. Issledovanie nestatsionarnogo istecheniya vskipayushchej zhidkosti v termodinamicheski ravnovesnom priblizhenii [Investigation of a nonstationary outflow of boiling liquid in a thermodynamic equilibrium approximation]. *Teplofizika Vysokikh Temperatur – High Temperature* vol. 16, no. 3 (1978): 556-562.
- 2 Edwards A.R., O'Brien T.P. Studies of phenomena connected with the depressurization of water reactors. *J. Br. Nucl. Energ. Soc.* vol. 9, no. 2 (1970): 125-135.
- 3 Nigmatulin R.I. Dynamics of multiphase media. Hemisphere, N.Y. vol. 1 (1990): 532.
- 4 Shagapov V.Sh., Yalaev A.Ya. On the theory of the bulk boiling of a liquid with transition into a metastable state. *Theoretical Foundations of Chemical Engineering* vol. 46, no. 4 (2012): 348-358.
- 5 R.Kh. Bolotnova and V.A. Buzina. Spatial modeling of the nonstationary processes of boiling liquid outflows from high pressure vessels. *computational continuum mechanics* vol. 7, no 4 (2014): 343-352.
- 6 Pinhasi G.A., Ullmann A., Dayan A. 1D plane numerical model for boiling liquid expanding vapor explosion (BLEVE). *Int. J. Heat Mass Tran.* vol. 50, no. 23-24 (2007): 4780-4795.
- 7 Ivashnev O.E. Specific features of the modeling of boiling-fluid flows. *Fluid Dynamics* vol. 43, no. 3 (2008): 390-401.
- 8 Bolotnova R.Kh., Buzina V.A., Galimzianov M.N., Shagapov V.Sh. *Gidrodinamicheskie osobennosti protsessov istecheniya vskipayushchej zhidkosti [Hydrodynamic features of the boiling liquid outflow processes]. Teplofizika i aeromehanika – Thermophysics and Aeromechanics* vol. 19, no. 6 (2012): 719-730.
- 9 Pribaturin N.A., Bezrukov Yu.A., Bykov M.A., Krasnov S.N., Onshin V.M., Lezhnin S.I., Sorokin A.L. Issledovanie strui pri istechenii vskipayushchej vody pri razryve truboprovoda [The study of the jet at the outflow of boiling liquid at break pipe]. *Proceedings of the 4th Russian National Conference on Heat Transfer* vol. 5, no. 6 (2006): 284-287.
- 10 Reshetnikov A.V., Mazheiko N.A., Begletsov V.N., Skokov V.N., Koverda V.P. Pulsation dynamics during explosive boil-up of overheated water jets. *Technical Physics Letters* vol. 33, no. 9 (2007): 732-734.
- 11 Nigmatulin R.I., Bolotnova R.Kh. Wide-range equation of state for water and steam: Simplified form. *High Temperature* vol. 49, no. 2 (2011): 303-306.

M. Odsuren<sup>1\*</sup> , G.Khuukhenkhuu<sup>1</sup> , S.Davaa<sup>1</sup> , K.Kato<sup>2</sup> 

<sup>1</sup> National University of Mongolia, Ulaanbaatar, Mongolia

<sup>2</sup>Hokkaido University, Sapporo, Japan

\*e-mail:odsuren@seas.num.edu.mn

## Structure of resonance states in the simple schematic model

**Abstract.** The complex scaling method is one of the powerful tool in wide areas of physics, particularly in nuclear physics. In the first stage, its advantage was mainly pointed out for description of the resonance states in the composite systems. In the last decade, the usage of this method has increased not only to obtain information on resonance states but also to determine scattering quantities in the observables. To determine the presence of many resonant states at the wave is not easy and complex scaling method can be used to determine the obtain many resonant states. The simple schematic two-body model is applied for study of many resonant states. Applying the complex scaling method, we can easily obtain several resonance states even with a wide and a sharp decay widths simultaneously. In this work, one bound and five resonance states for  $J^\pi = 0^+$  wave and one bound and four resonance states for  $J^\pi = 1^-$  wave are reported.

**Key words:** Complex scaling method, resonance and continuum states, cluster model.

### Introduction

Since the cluster structures of light nuclei are often observed as resonance states, it is important to develop the study of resonance states in multi-cluster systems. In theoretical studies for light nuclei, the complex scaling method (CSM) is a useful tool to get information unbound states as well as bound states within the same treatment. The detailed information about the structure of light nuclei has been carried out using different methods, one of them is the CSM [1-2]. The complex scaling was first proposed mathematically and it has been widely used in all fields of physics, especially in resonance and scattering studies in nuclear physics.

In the first stage, its advantage was mainly pointed out for description of the resonance states in the composite systems. Developing the CSM to give us a possibility to obtain information of continuum and non-continuum states for three-, four-, and five body systems. In the last decade, the usage of this method has increased not only to obtain information on resonance states but also to determine scattering quantities in the observables [3-5]. Furthermore, to understand structure of neutron rich nuclei, it is required to study structure of continuum and bound states as well. Recently, it has attracted much attention that the CSM has applied for observation of wide resonant and virtual states considering continuum states in light nuclei [6-10].

In this work, we apply the CSM to a simple schematic two-body model [8] for obtaining many resonance states. Applying the simple schematic potential for  $J^\pi = 0^+$  and  $1^-$  waves, we calculate five resonance states in each waves.

### Method

We take up two-body systems, which are described by the *Schrödinger* equation

$$\hat{H}|\Psi\rangle = E|\Psi\rangle,$$

where the Hamiltonian  $H$  consists of kinetic energy  $T$  and potential  $V$  for the relative motion between two bodies. The eigenvalue problem is generally solved under a boundary condition of asymptotic outgoing waves for bound states and resonances. The outgoing boundary condition directly enables us to solve bound states in an  $L^2$  functional basis set because the states have negative energies and a damping behavior in the asymptotic region. Resonant states are unbound and defined as the eigenstates belonging to the complex eigenenergy, which corresponds to a complex momentum value in the lower half plane [3]. The resonant states cannot be solved in the  $L^2$  functional space due to asymptotically divergent behavior. Furthermore, continuum states of arbitrary positive energies cannot also be obtained under the outgoing

condition. The complex scaling has been introduced to solve resonant states within  $L^2$  basis functions and is defined by the following complex-dilatation transformation for relative coordinate  $r$  and momentum  $k$  is rewritten as  $r \rightarrow r e^{i\theta}$ . Where  $\theta$  is a scaling angle given by a real number and  $0 < \theta < \theta_{\max}$ . The maximum value  $\theta_{\max}$  is determined to keep analyticity of the transformed potential. For example,  $\theta_{\max} = \pi/4$  for a Gaussian potential. In a many-body system, this transformation makes every branch cut rotated by  $-2\theta$  from the real axis on the complex energy plane. In the wedge region pinched by the rotated branch cut and the positive energy axis, resonance eigenstates are obtained by solving the following eigenvalue problem:

$$\hat{H}(\theta)|\Psi^\theta\rangle = E^\theta|\Psi^\theta\rangle,$$

$$\Psi^\theta = \sum_{i=1}^N c_i^\theta \varphi_i,$$

within an appropriate non-orthogonal  $L^2$  basis set  $\{\varphi_i, i=1, 2, \dots, N\}$ . Where  $\hat{H}(\theta)$  and  $\Psi^\theta$  are the complex scaled Hamiltonian and wave function, respectively. The bound states are obtained on the negative-energy axis independently from  $\theta$  as well as the ordinary bound states. Because of a finite number of basis states, the continuum states are discretized with complex energies distributed on the rotated branch cut ( $2\theta$  line).

The eigenvalues and eigenstates of the complex scaled *Schrödinger* equation (2) are classified as

$$[E, \Psi^\theta] = \begin{cases} (E_b, \Psi^b) & b = 1, \dots, N_b; & \text{bound states} \\ (E_r, \Psi^r) & r = 1, \dots, N_r^\theta; & \text{resonant states,} \\ (E_c(\theta), \Psi^c) & c = 1, \dots, N - N_b - N_r^\theta; & \text{continuum states} \end{cases} \quad (4)$$

where  $N_b$  and  $N_r^\theta$  are the number of bound states and the number of resonant states which depend on  $\theta$ , respectively. The complex energies of resonant states are obtained as  $E^\theta = E_r - i\Gamma_r/2$ , where  $E_r$  is resonance energy and  $\Gamma_r$  is width of the resonant state. The discretized energies  $E_c(\theta)$  of continuum states are  $\theta$  dependent and expressed as  $E_c(\theta) = \epsilon_c^r - i\epsilon_c^i$ .

These three-kind solutions of the complex-scaled *Schrödinger* equation construct the extended completeness relation:

$$\sum_{b=1}^{N_b} |\Psi^b\rangle\langle\tilde{\Psi}^b| + \sum_{r=1}^{N_r^\theta} |\Psi^r\rangle\langle\tilde{\Psi}^r| + \int_{L_c} dE_c |\Psi^c\rangle\langle\tilde{\Psi}^c| = 1, \quad (5)$$

where the tilde ( $\tilde{\phantom{x}}$ ) in bra states means the biorthogonal states with respect to the ket states due to non-Hermitian property of  $H^\theta$ . The integration of the third term is taken along the rotated branch cut  $L_c$ . In the case of eigenstates within a finite number of  $L^2$  basis states, the integration for continuum states is approximated by the summation of discretized states as [6]

$$\sum_{b=1}^{N_b} |\Psi^b\rangle\langle\tilde{\Psi}^b| + \sum_{r=1}^{N_r^\theta} |\Psi^r\rangle\langle\tilde{\Psi}^r| + \sum_{c=1}^{N-N_b-N_r^\theta} |\Psi^c\rangle\langle\tilde{\Psi}^c| \approx 1. \quad (6)$$

It has been investigated that the reliability of the approximation of the continuum states are confirmed by using a sufficiently large basis number of  $N$  in the CSM [2].

### Results and discussion

The Hamiltonian of the present model is given as

$$H = -\frac{\hbar^2}{2\mu} \nabla^2 + V(r), \quad (7)$$

where

$$V(r) = -8.0 \exp(-0.16r^2) + 4.0 \exp(-0.04r^2). \quad (8)$$

For simplicity, we put  $\frac{\hbar^2}{\mu} = 1$  (MeV fm<sup>2</sup>). This potential introduced in Ref. [8] has an attractive pocket in a short range but a repulsive barrier at a large distance. To solve the Eq. (2), we employ the Gaussian basis functions given as

$$u_i(\hat{r}) = N_l(b_i)r^l \exp\left(-\frac{1}{2b_i^2}r^2\right) Y_{lm}(\hat{r}), \quad (9)$$

where the range parameters are given by a geometric progression as  $b_i = b_0 \gamma^{i-1}$ ,  $i = 1, 2, \dots, N$ .

In this calculation, we apply  $N = 20$  and employ the optimal values of  $b_0$  and  $\gamma$  to obtain stationary resonance solutions.

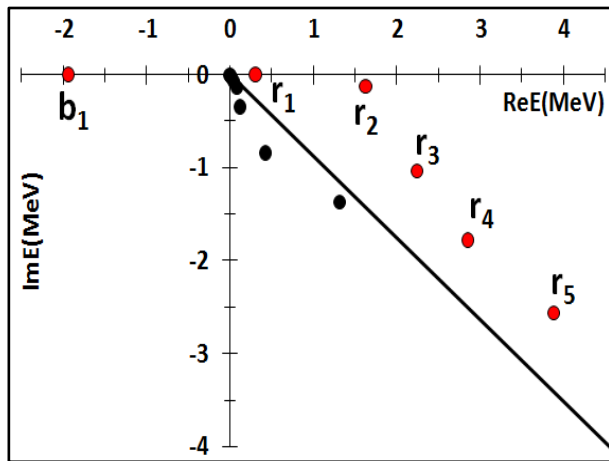


**Figure 1** – Schematic scenario of energy eigenvalues for  $J^\pi = 0^+$  wave on the complex energy plane. Here bound state is expressed as  $b$ . The resonant states are displayed  $r$  and indexes of  $r$  are corresponding the number of resonant states.  $\theta = 15^\circ$  is applied as a scaling angle.

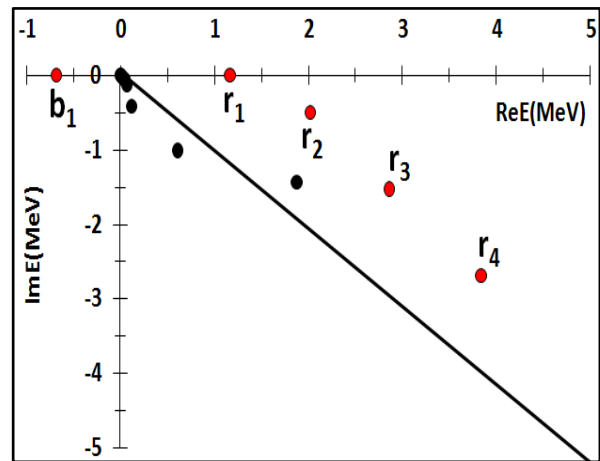


**Figure 2** – Schematic scenario of energy eigenvalues for  $J^\pi = 1^-$  wave on the complex energy plane. The same analysis is performed as done in Fig. 1.  $\theta = 20^\circ$  is applied as a scaling angle.

In Figs. 1-2, the energy eigenvalue distributions on the complex energy plane for  $J^\pi = 0^+$  and  $1^-$  waves are shown. When we apply  $\theta = 15^\circ$ , we observe isolated energy points as shown in Fig.1. In Fig.1, we find one bound and five resonance states for  $J^\pi = 0^+$  wave. The bound state is expressed as a red filled circle on the negative energy axis and it is expressed as  $b$ . The resonant states are displayed by red filled circles and given by  $r$  and indexes of  $r$  are corresponding the number of resonant states.

In Fig.2, we obtained one bound and four resonance states for  $J^\pi = 1^-$  wave by applying  $\theta = 20^\circ$ . We calculate one bound and four resonance states for  $J^\pi = 1^-$  wave. In Fig. 2, the filled red circles are expressed bound and resonant states. The

bound state is expressed  $b$  and obtained on the negative energy axis.  $r$  implies the resonant states and its indexes are corresponding the number of resonant states.

As can be seen from Figs. 1-2, energy eigenvalues are located on the  $2\theta$  lines except bound and resonance states. The resonant poles with narrow and wide decay widths appear above the threshold as shown with the filled red circles in Figs. 1-2.

The results of the calculated resonance energies and widths for  $J^\pi = 0^+$  and  $1^-$  partial waves applying the schematic potential model are summarized in Table I. Table I contains the bound and resonance energies with decay widths at each partial waves.

**Table I** – The calculated resonance energies and decay widths for  $J^\pi = 0^+$  and  $1^-$  waves.

$0^+$ wave		$1^-$ wave	
E (MeV)	state	E (MeV)	state
-1.922782	bound	-0.674647	bound
$0.3101-i10^{-6}$	resonance	$1.1710-i4.948 \times 10^{-3}$	resonance
$1.6322-i0.1228$	resonance	$2.0309-i4.8944 \times 10^{-1}$	resonance
$2.2493-i0.9367$	resonance	$2.8318-i1.7186$	resonance
$2.7667-i1.3169$	resonance	$3.7834-i2.5148$	resonance
$3.8433-i1.8445$	resonance		

## Conclusions

In this work we discussed many resonant states for  $J^\pi = 0^+$  and  $1^-$  waves applying a simple schematic potential, in the framework of the CSM to investigate the bound and unbound states. The present method is very useful to get structure information of many resonant states with bound state in the same manner. We calculated one bound and five resonance states for  $J^\pi = 0^+$  wave and one bound and four resonance states for  $J^\pi = 1^-$  wave, respectively. For getting the structure of many resonant states give us a possibility to develop a method for determining a broad resonance state or a virtual state calculating scattering quantities using continuum and non-continuum states.

## Acknowledgments

This work was supported by the Asian Research Center project (ARC) at National University of Mongolia (ARC2020-2021 P2019-3710). The numerical calculation was supported by the MINATO cluster computing system at the Nuclear Research Center, National University of Mongolia.

## References

1. Ho Y.K. "The method of complex coordinate rotation and its applications to atomic collision processes." *Phys. Rep.* Vol.99 (1983): 1.
2. Aoyama S., Myo T., Katō K., Ikeda K. "The Complex Scaling Method for Many-Body Resonances and Its Applications to Three-Body Resonances." *Prog. Theor. Phys.* Vol.116 (2006): 1.
3. Katō K., Aikawa M., Myo T., et al. "Decomposition of scattering phase shifts and reaction cross sections using the complex scaling method." *Physical Review C.* Vol.89, no.3 (2014): 034322.
4. Kruppa A.T., Katō K. "Resonances in Complex-Scaled Orthogonality Condition Model of Nuclear Cluster System." *Prog. Theor. Phys.* Vol.84 (1990): 1145.
5. Khuukhenkhoo G., Kato K., et al. "Structure of Continuum States of A= 5 Mirror Nuclei in the Complex Scaling Method." *Acta Physica Polonica B.* Vol.50, no.3 (2019): 549.
6. Myo T., Ohnishi A., Katō K. "Resonance and Continuum Components of the Strength Function." *Prog. Theor. Phys.* Vol.99 (1998): 801.
7. Odsuren M., Khuukhenkhoo G., Sarsembayeva A.T., Amangeldi N., Katō K. "Analysis of continuum level density for virtual and resonance states." *Indian Journal of Physics* (2021): 1.
8. Csótó A., Gyarmati B., Kruppa A. T., Pál K. F., Moiseyev N. "Back-rotation of the wave function in the complex scaling method." *Phys. Rev. A.* Vol.41 (1990): 3469.
9. Katō K., Khuukhenkhoo G., Davaa S., et al. "Scattering cross section for various potential systems." *Nuclear Engineering and Technology* Vol. 49, no.5 (2017): 1006.
10. Katō K., Khuukhenkhoo G., et al. "Scattering phase shifts in the complex scaling method." *Journal Experimental and Theoretical Physics letters* Vol.102, no.7 (2015): 409.



S. A. L. Maftunzada

Faryab University, Maymana, Afghanistan

e-mail: [latif.maftunzada@gmail.com](mailto:latif.maftunzada@gmail.com)

## Definition of physical parameters of 8 X-class solar flares

**Abstract.** We observed top 8 X-class solar flares registered in the period May 1998 – May 2015. We measure physical parameters of 8 solar flares, such as the temporal scale, size, and magnetic flux density, and find that the sizes of flares tend to be distributed more broadly as the GOES class becomes weaker and that there is a lower limit of magnetic flux density that depends on the GOES class. We also made a brief analysis of solar flares registered in these days, also has shown the duration of time and peak of solar flares in Universal time. We have identified several physical quantities of solar flares and estimated reconnection rate of solar flares. To determine the physical parameters we used images taken with the AIA instrument on board SDO satellite at wavelengths 131 Å, 174 Å, 193 Å, 211 Å, 335 Å, 1600 Å, 1700 Å, 4500 Å, SXT – pictures, HMI Magnetogram, SOLIS Chromospheric Magnetogram, GOES XRT-data. Using the observed values, we calculate reconnection inflow velocity, coronal Alfvén velocity, and reconnection rate. The inflow velocities vary from a few kilometers per second to several tens of kilometers per second, and the Alfvén velocities in the corona are in the range of  $10^3$  to  $10^4$  kilometers per second. As a result, the rate of reconnection is  $10^{-3}$ . We find that the reconnection rate in a flare tends to decrease as the GOES class of the flare increases.

**Key words:** solar flares, X-rays, reconnection rate.

### Introduction

Across the electromagnetic spectrum, flares have a broad variety of effects. They emit x-rays and ultraviolet radiation during a pulse, suggesting extremely high temperatures. Radio waves demonstrate that a small fraction of particles are accelerated to high energies. Synchrotron radiation, which is generated by electrons spiraling along magnetic field lines, accounts for the majority of the radiation. The flux of high-energy particles and cosmic rays on Earth is also increased by intense flashes. Magnetic storms on Earth usually occur 36 hours after a flare on the Sun. The most popular theory is that the solar wind is amplified, compressing the magnetosphere and raising the magnetic field at the Earth's surface. Solar flares form when the direction of the local magnetic field suddenly shifts. The alternative reason for the rapid release of energy in bursts is magnetic reconnection [1].

Solar flares are one of the most strong and energetic phenomena in the solar atmosphere. Due to their importance in the energy balance of the solar corona and their work playing an important role in space weather, several observations

investigated the release of energy and induction of solar flares based on solar activity. National solar observatories provide a wealth of data to the overall network, spanning long time periods (e.g., Solar and Heliospheric Observatory, SOHO), multiple perspectives (Solar Terrestrial Relations Observatory, STEREO), and returning a large amount of data (Solar Dynamics Observatory, SDO). Specifically, the huge amount of SDO data are accessible only from a few repositories, such type of data as a full-cadence data or full-disk of scientific concern are hard to download, because of their size.

Solar flares are large "explosions" that occur as a sudden brightening of the Sun's atmosphere over active areas (sunspot groups). They live in the chromosphere and corona, but the most powerful ones can also increase the photosphere's temperature (producing a flare visible even in white light). Richard Carrington, who was drawing sunspots at the time, found two bright spots in one of the sunspot classes and called it a solar flare. In just ten minutes, they brightened and faded. Carrington had already noted that this phenomenon was accompanied the next night by the emergence of the northern lights. In the last century, less than a hundred of these white-flares have been discovered.

In the short wavelength range, the brightening is even more pronounced (UV and X-ray). The Sun's total ultraviolet radiation increases by a significant factor during a flare, while the amount X-ray radiation increases by orders of magnitudes [2].

Solar flares are massive solar explosions that carry energy, light, and high-speed particles into space. These flares are often linked to coronal mass ejections, which are solar magnetic storms (CMEs). The number of solar flares increases every 11 years, and the sun is currently approaching another solar maximum, which will most likely occur in 2013. This means there would be more flares, some small and some large enough to send radiation all the way to Earth.

Based on a classification scheme that distinguishes solar flares according to their frequency, the most powerful flares are classified as "X-class flares." A-class (near background levels) is the smallest, followed by B, C, M, and X. Each letter reflects a 10-fold increase in energy production,

similar to the Richter scale for earthquakes. As a result, an X is ten times an M and one hundred times a C. Within each letter class there is a finer scale from 1 to 9 [3-6].

Earth is not affected by C-class and smaller flares because they are too tiny. M-class flares can trigger brief radio blackouts and minor radiation storms at the poles, putting astronauts in risk. [7-8].

The most powerful flare ever measured with modern methods occurred in 2003, during the last solar maximum, and it was so powerful that the sensors measuring it were overloaded. The massive solar X-ray flare that occurred on November 4th was estimated to be an X28. This is a new record-breaking X-ray flare, the most powerful in recorded observational history.

In this work we have identified several physical quantities of X-class solar flares and estimated reconnection rate of X-class solar flares. We have analyzed top 8 strongest solar flares registered from the period May 1998 – May 2015.

**Table 1** – Strongest solar flares since May 1998 [6].

№	GOES class	Date	Region	Start	Maximum	End
1	X3.1	2014/10/24	2192	21:07	21:41	22:13
2	X3.1	2002/08/24	0069	00:49	01:12	01:31
3	X3	2002/07/15	0030	19:59	20:08	20:14
4	X2.8	2013/05/13	1748	15:48	16:05	16:16
5	X2.8	2001/12/11	9733	07:58	08:08	08:14
6	X2.8	1998/08/18	8307	08:14	08:24	08:32
7	X2.7	2015/05/05	2339	22:05	22:11	22:15
8	X2.7	2003/11/03	0488	01:09	01:30	01:45
9	X2.7	1998/05/06	8210	07:58	08:09	08:20
10	X2.6	2005/01/15	0720	22:25	23:02	23:31

### Data analysis

The magnetic energy contained in the solar atmosphere may explain the amount of energy  $E_{flare}$  emitted during a flare [9],

$$E_{flare} \sim E_{mag} = \frac{B_{cor}^2 L^3}{8\pi} \quad (1)$$

where  $L$  is the characteristic size of the flare and  $B_{cor}$  is the characteristic magnetic flux density in the corona [10-13]. Since the released magnetic energy equals the energy flowing into the

reconnection field, the energy release rate can be expressed as

$$\left| \frac{dE_{mag}}{dt} \right| \sim 2 \frac{B_{cor}^2}{4\pi} V_{in} L^2 \quad (2)$$

where  $V_{in}$  is the inflow velocity of the plasma. Therefore, the time required for the energy inflow to supply the flare energy is estimated as

$$\tau_{flare} \sim E_{flare} \left( \left| \frac{dE_{mag}}{dt} \right| \right)^{-1} \sim \frac{L}{4V_{in}} \quad (3)$$

and this should be the timescale of the flare. We can measure the inflow velocity  $V_{in}$  using this timescale as

$$V_{in} \sim \frac{L}{4\tau_{flare}} \tag{4}$$

To calculate the nondimensional reconnection rate  $M_A \equiv \frac{V_{in}}{V_A}$ , we must first calculate the Alfven velocity  $V_A = \frac{B_{cor}}{(4\pi\rho)^{1/2}}$  in the inflow region: As a

result, we can calculate inflow velocity  $V_{in}$ , Alfven velocity  $V_A$ , and reconnection rate  $M_A$  by measuring the coronal mass, the flare's spatial scale  $L$ , the magnetic flux density in the corona  $B_{cor}$ , the coronal density  $\rho$ , and the flare's timescale  $\tau_{flare}$ , [14-15].

The Geostationary Operational Environmental Satellite, or GOES [5], keeps track of solar flares in real time. Satellites GOES 13, GOES 14, and GOES 15 provided data on electrons, protons, and X-rays [5-6].

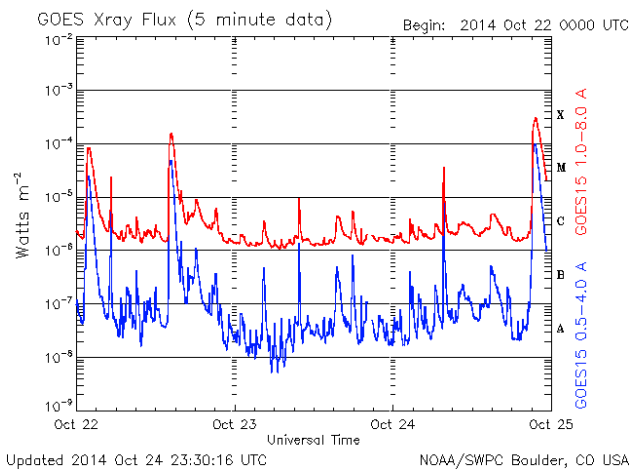
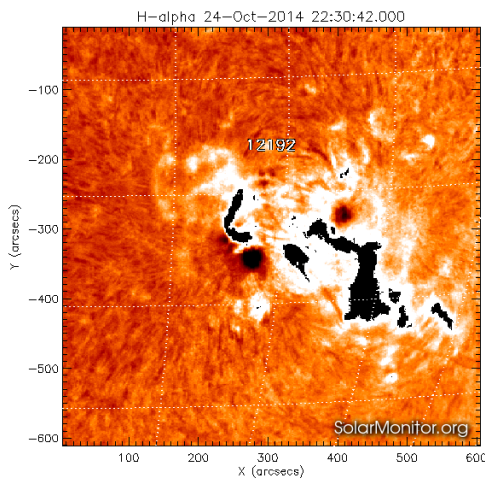


Figure 1 – Active area 12192 (GHN H $\alpha$ ) and the total X-ray flux obtained in GOES 13 and GOES 15 [5]

In Fig. 1 shown the images obtained on the board of Hinode satellite in XRT (October 24, 2014, X3.1). To determine the length of the loops, we used SXT images. The length of the

loops can be calculated using the SXT data. The total flux of X-rays and an electron, which was registered on October 24, 2014, is shown in Fig. 2.

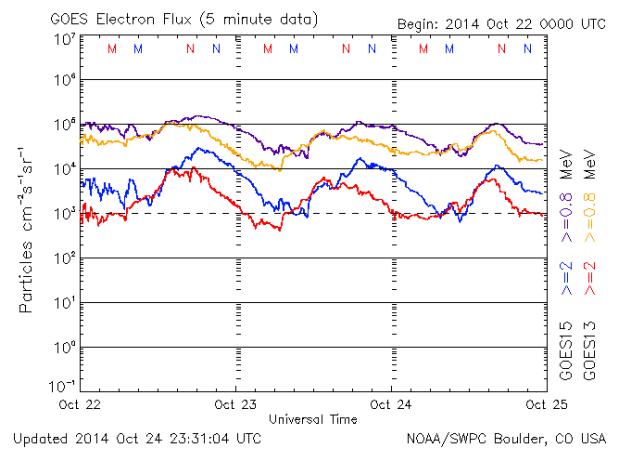
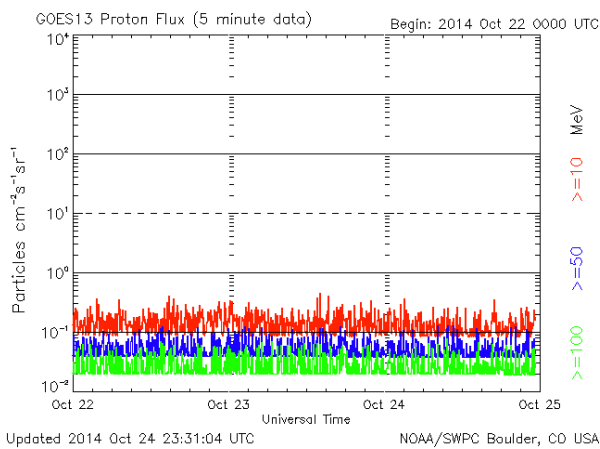


Figure 2 – Total proton and electron flux obtained in GOES 13 and GOES 15 [5]

**Results**

Using the above described method, we analyzed 8 X-class solar flares that have been registered 1998-2015 years. The reconnection rate was examined in relation to the GOES class of solar flares. The flare parameters obtained in this study are summarized in Table 2.

There is a weak correlation between the timescale  $\tau_{flare}$  and the GOES peak flux (Fig. 3a). The characteristic size of flares,  $L$ , shows a larger scatter when the GOES peak flux is smaller (Fig. 3b). Figure 4 shows the dependence of the reconnection rate  $M_A$  from GOES class.

**Table 2** – Parameters of the flares

Date	Active region	GOES class	$\tau(s)$	$L(cm)$	$V_{in}(cm \cdot s^{-1})$	$M_A$	$E_{flare} / \tau(erg \cdot s^{-1})$
2014/10/24	2192	X3.1	2040	2,18E9	2,67E5	3,33E-4	4,05E27
2002/08/24	0069	X3.1	1380	2,1E9	3,81E5	4,76E-4	5,41E27
2002/07/15	0030	X3	540	2,83E9	1,31E6	1,63E-3	3,36E28
2001/12/11	9733	X2.8	600	1,89E9	7,85E5	9,81E-4	8,97E27
2015/05/05	2339	X2.7	360	3,19E9	2,22E6	2,77E-3	7,25E28
2003/11/03	0488	X2.7	1260	1,96E9	3,88E5	4,85E-4	4,78E27
1998/05/06	8210	X2.7	660	1,16E9	4,39E5	5,49E-4	1,9E27
2005/01/15	0720	X2.6	2220	1,38E9	1,55E5	1,94E-4	9,46E26

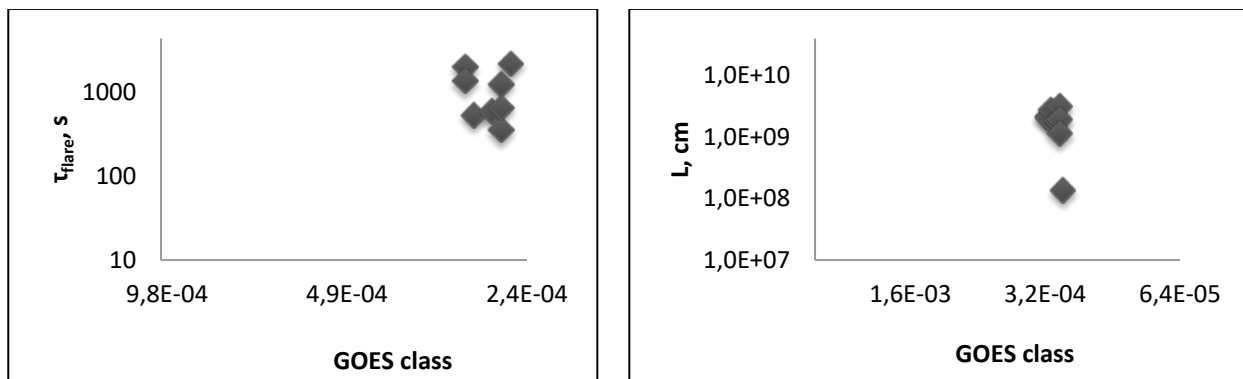


**Figure 3** – Physical parameters of each flare plotted against the GOES class. (a) Timescale  $\tau_{flare}$ . (b) Size  $L$ .

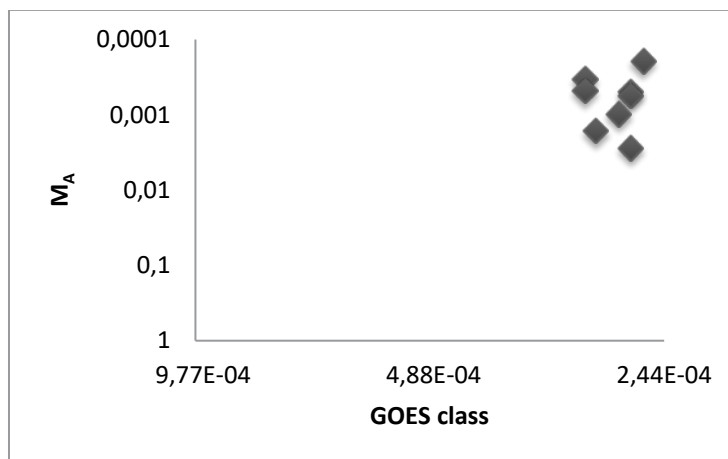


**Figure 4** – Reconnection rate  $M_A$  plotted against GOES class.

## Conclusion

As a result of the sudden flash, the flux of high-energy particles and cosmic rays increases on Earth. Magnetic storms on Earth typically occur 36 hours after a flare event on the Sun has been detected. The amplification of the solar wind, which compresses the magnetosphere and raises the magnetic field at the Earth's surface, is the most common explanation. Solar flares arise in areas where a sharp change in the direction of the local magnetic field occurs. The reconnection rate values are distributed in a range from to  $10^{-4} - 10^{-3}$ . As the GOES class increases, the value of the reconnection rate decreases. The reconnection rate obtained in this study is within one order of magnitude of the Petschek model's predicted maximum value [13].

## References

- 1 Sweet P.A. Cambridge: Cambridge Univ. Press, 1958.
- 2 Parker E.N. "Sweet's mechanism for merging magnetic fields in conducting fluids." *J. Geophys. Res.* Vol.62 (1957): 509-520.
- 3 Parker E.N. "The solar flare phenomenon and theory of reconnection and annihilation of magnetic fields." *Astrophys. J. Supp.* Vol.8 (1963): 177-211.
- 4 Garcia, H.A. "Forecasting methods for occurrence and magnitude of proton storms with solar hard X rays." *Space Weather* Vol.2 (2004): S06003.
- 5 GOES Space Environment Monitor. <http://www.ngdc.noaa.gov/stp/satellite/goes/> (accessed May 31, 2021).
- 6 Solar Flare Data. <ftp://ftp.ngdc.noaa.gov/STP/space-weather/solar-data/solar-features/solar-flares/x-rays/goes/> (accessed May 31, 2021).
- 7 Isobe H., Takasaki H., Shibata K. "Measurement of the Energy Release Rate and the Reconnection Rate in Solar Flares." *ApJ.* Vol.632 (2005): 1184.
- 8 Aschwanden M. J., Alexander D. "Solar Flare and CME Observations with STEREO/EUVI." *Solar Phys.* Vol.204 (2001): 91.
- 9 A. Sarsembayeva, F. Belisarova, M. Odsuren, A. Sarsembay. "February 25, 2014 solar flare data analysis in SunPy." *Physical Sciences and Technology.* Vol.7, No. 3-4 (2020): 22-26.
- 10 Garcia H. A. "Forecasting methods for occurrence and magnitude of proton storms with solar hard X rays." *Space Weather* Vol.2 (2004): S06003.
- 11 Haisch, B., Strong, K.T., Rodono, M. "Flares on the Sun and other Stars." *Ann. Revs. Astron. Astrophys.* Vol. 29 (1991): 275.
- 12 Phillips K. J.H., Feldman U. "Properties of cool flare with GOES class B5 to C2." *Astron. Astrophys.* Vol.304 (1995): 563.
- 13 W.N. Hess Washington D.C.: NASA SP-50, 1964.
- 14 K. Nagashima. "Statistical study of the reconnection rate in solar flares observed with Yohkoh SXT." *ApJ.* Vol. 647, no.654 (2006).
- 15 Sarsembayeva A.T., et al. "Solar activity monitoring for the PERIOD March 20-25, 2019." *NEWS of the National Academy of Sciences of the Republic of Kazakhstan. Series of Physical and Mathematical* №4 (2020): 35-41.

E. Boos<sup>1</sup> , V. Bunichev<sup>1</sup> , G. Nurbakova<sup>2\*</sup> ,  
N. Habyl<sup>2</sup> , S. Ruġtembayeva<sup>2</sup> , D. Temirkhanova<sup>2</sup> 

<sup>1</sup>Moscow State University named after Lomonosov, Moscow, Russia

<sup>2</sup>Al-Farabi KazNU, Almaty, Kazakhstan

\*e-mail: g.nurbakova@gmail.com

## Top-quark physics in hadronic collisions

**Abstract.** This article is devoted to the processes with the participation of the  $t$ -quark. The top quarks are one of the most amazing elementary particles. Predictions of the characteristics of various interactions involving the  $t$ -quark have high theoretical accuracy, as well as  $t$ -quark has large production cross section which makes it a unique laboratory for testing the Standard Model and beyond. The top quark is one of the important objects in the searches for new effects.

The review includes the main properties of the top quark, the complete theoretical analysis and experimental measurements of top quark processes and the possibilities of searching for manifestations of New physics (NF) beyond the Standard Model (SM).

Interactions of  $t$ -quarks are described in the framework of the model-independent way and gauge-invariant methods.

Another distinctive feature of study of the  $t$ -quark processes is the absence of hadrons containing  $t$ -quark in nature. So there is a unique opportunity to study the fundamental properties of a  $t$ -quark without any hadronization effects.

**Key words:** Higgs boson, top quark, Feynman diagram, model independent and gauge invariant method, Form factor, partial width, Standard Model.

### Introduction

In this review, we give a brief description of the top quark physics, which is the most amazing among the elementary particles.

The name "elementary" particle has two meanings: the term "elementary" particle is used for all for all subatomic particles whose dimensions are smaller than  $10^{-10}$  m (the characteristic atomic dimensions). Namely all baryons, mesons, quarks, leptons, photons, gluons, massive vector bosons ( $W^\pm$ ,  $Z^0$ ), and the Higgs boson are "elementary" particles.

More precise scientific meaning of the term "elementary" is that an "elementary" particle is an object that does not have an internal structure and behaves like a point like object in all currently known interactions and at all available interaction energies. The modern point like particles are all quarks, leptons, photons, gluons, massive vector bosons, ( $W^\pm$ ,  $Z^0$ ), and the Higgs boson. Baryons and mesons are composite particles that consist of quarks and gluons.

The  $t$  quark was discovered by the collaborations D0 and CDF [2, 3]. Historical overview of the  $t$ -quark discovery and the results of the study of the  $t$ -quark physics are described in [4]. A more detailed description of the  $t$ -quarks physics with full theoretical and experimental aspects can be found in the review [1].

The past ten year results of the Large Hadron Collider (LHC -Large Hadron Collider) led to a set of surprising discoveries and interesting results. Some rare processes with the participation of the  $t$ -quark have been detected experimentally. It has been measured their characteristics with high accuracy. A search for possible manifestations of the "New Physics" in the  $t$ -quark sector was carried out. It wasn't observed statistically significant experimental deviations from the SM predictions. And according to the results of measurements, restrictions were established on the parameters of new models, which lead to deviations from the SM predictions.

## 1 The properties of the top quark

In the Standard Model (SM), the  $t$ -quark is the heaviest particle of the third generation and has the same quantum numbers as the “up” and “charm” quarks. It is a fermion with spin  $\frac{1}{2}$  and electric charge  $Q = +2/3$ . As known fermions described by the Dirac fermion field which can be decomposed into two projections with left and right chiralities. Therefore the left chiral part of the  $t$ -quark is the upper component of the weak isospin doublet, and the right chiral component is the weak isospin singlet. In strong interaction  $t$ -quark is considered as a colored triplet with respect to the SU(3) gauge group.

There are two distinctive features of the  $t$  quark from the other quarks. The first is its mass which is much larger than others. Also the  $t$ -quark very weak mixes by the first and second generation quarks.

The magnitude of the  $t$ -quark mass  $m_t$  is not predicted by theory. From the experimental measurements at Tevatron and LHC we have:

$$m_t = 173.1 \pm 0.6 \text{ GeV}$$

$$L_{SM} = -Q_t e \bar{t} \gamma^\mu A_\mu - \frac{g}{2 \cos v_W} \bar{t} \gamma^\mu \left[ \left( \frac{1}{2} - 2Q_t \sin^2 v_W \right) - \frac{1}{2} \gamma_5 \right] t Z_\mu - \frac{y_t}{\sqrt{2}} \bar{t} t H - g_s \bar{t} \gamma^\mu t^a t G_\mu^a - \frac{g}{\sqrt{2}} \sum_{q=d,s,b} \frac{V_{tq}}{2} \bar{t} \gamma^\mu (1 - \gamma_5) q W_\mu^+ + h. c. \quad (1)$$

where  $g_s$ ,  $e$  and  $g$  are the coupling constants of the strong, electromagnetic and weak interactions correspondingly, charge of the  $t$ -quark is  $Q_t = +2/3$ .

$$y_t = \sqrt{2} \frac{m_t}{v_{ew}}, \quad v_{ew} \approx 246 \text{ GeV} \quad (2)$$

where  $v_{ew}$  is the electroweak scale, i.e. the vacuum average of the Higgs field.

In expression (1) the matrix  $(1 - \gamma_5)$  corresponds to the fact that only the left-hand component of the  $t$ -quark participates in the interaction.

### 2.2 Lagrangian of anomalous top-quark interactions

Currently it is unknown what type of New Physics will be responsible for possible deviations from the predictions of the Standard Model. There exists a number of different scenarios of the Standard Model extensions: SUSY, models with

with an error less than 0.35%, which is the most accurate mass determination among all quarks [5]. The mass of the  $t$ -quark is only slightly less than the mass of the gold nucleus (for example, the mass of the 186th isotope of the nucleus is 173.2 GeV). Despite such a large value of the mass the  $t$ -quark behaves point like particle in all known creation and decay processes.

In the SM the mixing of quarks if expressed in terms of unitary Cabibbo-Kobayashi-Maskawa (CKM)  $|V_{qq'}|$  matrix [6, 7]. The value of the element  $|V_{tb}|$  is very close to one, while the value of the elements  $|V_{ts}|$  and  $|V_{td}|$  are much less than one. This suggests that within the SM the  $t$ -quark decays into a W-boson and  $b$ -quark with a probability close to 100%.

## 2 The study of the processes involving the top quarks within the sm and beyond

### 2.1 Interaction Lagrangian of the top quarks

Let us start from the Lagrangian which provides all interaction rules of the quarks. The Lagrangian of the  $t$ -quark interaction within the SM has the form (see [1, 8]):

extra space-time dimensions, composite or partially composite models. This lead either to predictions of new mechanisms of the interactions or to a significant change (enhancement) of rare processes involving the  $t$ -quarks. The experimental discovery of this new mechanisms and the enhancement of rare processes would indicate the existence of New Physics.

Anomalous interactions of the top quarks can be described by the effective field theory [9]. The effective field theory is more universal model-independent approach which is based on phenomenological Lagrangian [1,10,11]. This Lagrangian must be gauge-invariant with respect to the gauge group (otherwise, the introduced anomalous interactions would immediately lead to contradictions with modern precision measurements) and consists of a number of terms with increasing dimensions, suppressed by ever higher degrees of NF scale, which, as follows from the existing

constraints, should be significantly larger than the electroweak scale  $v_{ew} \approx 246 GeV$ :

$$L = L_{SM} + \sum_i \frac{c_i^{(6)}}{\Lambda^2} O_i^{(6)} + \frac{c_i^{(8)}}{\Lambda^4} O_i^{(8)} + \dots \quad (3)$$

The effective Lagrangian include the gauge-invariant operators  $O_i^{(N)}$  and the corresponding coefficients  $c_i^{(N)}$ . The complete set of operators of the lowest possible dimension 6, contributing to the interactions of the top quark with other SM fields, is given in the review [12]. This set of operators involving the  $t$ -quark field is the subset of the complete set of operators called the Warsaw basis [11].

In the framework of the effective field theory (EFT) the Lagrangian of anomalous  $t$ -quark interactions can be represented in the following form

$$L_{EFT} = L_{SM} + k_4 \bar{\psi}_q \hat{O}^{(4)} \psi_t + \frac{k_5}{\Lambda} \bar{\psi}_q \hat{O}^{(5)} \psi_t + \frac{k_6}{\Lambda^2} \bar{\psi}_q \hat{O}^{(6)} \psi_t + \dots \quad (4)$$

where  $\Lambda$  is the scale parameter of NF,  $k$  is anomalous constants that have a natural order of magnitude  $v_{ew}^2/\Lambda^2$ .

The question of constructing the effective gauge-invariant Lagrangians was also studied in earlier papers (see, for example, [9, 13, 14, 1]). For historical reasons, an effective Lagrangian in the unitary gauge of the following form is widely used in the analysis of experimental data:

$$L_{anoum} = \left. \begin{aligned} & -\frac{1}{\sqrt{2}} \sum_{q=u,c,t} \bar{t} (v_{tq}^H + \gamma_5 a_{tq}^H) q H \\ & -\frac{g}{\sqrt{2}} \bar{t} \gamma^\mu (f_V^L P_L + f_V^R P_R) b W_\mu^+ \\ & -\frac{g}{2 \cos v_W} \sum_{q=u,c,t} \bar{t} \gamma^\mu (v_{tq}^Z + a_{tq}^Z \gamma_5) q Z_\mu \\ & -g_s \sum_{q=u,c,t} \frac{k_{tq}^g}{\Lambda} \bar{t} \sigma^{\mu\nu} t^\alpha (f_{tq}^g + i h_{tq}^g \gamma_5) q G_{\mu\nu}^a \\ & -\frac{g}{\sqrt{2}} \bar{t} \frac{\sigma^{\mu\nu} \partial_\nu W_\mu^+}{M_W} (f_T^L P_L + f_T^R P_R) b \\ & -e \sum_{q=u,c,t} \frac{k_{tq}^\gamma}{\Lambda} \bar{t} \sigma^{\mu\nu} (f_{tq}^\gamma + i h_{tq}^\gamma \gamma_5) q A_{\mu\nu} \\ & -\frac{g}{2 \cos v_W} \sum_{q=u,c,t} \frac{k_{tq}^Z}{\Lambda} \bar{t} \sigma^{\mu\nu} (f_{tq}^Z + i h_{tq}^Z \gamma_5) q Z_{\mu\nu} \end{aligned} \right\} + h. c. \quad (5)$$

where  $g$  is the interaction constant of the gauge group of weak isospin  $SU(2)_L$ ,  $P_{L,R} = (1 \mp \gamma_5)/2$ ,  $\sigma_{\mu\nu} = i/2(\gamma_\mu \gamma_\nu - \gamma_\nu \gamma_\mu)$ , the field strength tensors are defined as usual ( $G_{\mu\nu}^a = \partial_\mu G_\nu^a - \partial_\nu G_\mu^a + \dots$ ); parameter  $\Lambda$  is the scale of New physics of the order of several TeV;  $k$  is anomalous constants

which is assumed to be a real numbers,  $f$  and  $h$  are constants generally considered as complex numbers with the normalization  $|f|^2 + |h|^2 = 1$ .

Values for the parameters from the Lagrangian (5) are:

$$\left. \begin{aligned} v_{tt}^H &= y_t = \sqrt{2} \frac{m_t}{v_{ew}}, & a_{tt}^H &= 0 \\ v_{tt}^H &= a_{tt}^H = 0, & q &\neq t \\ f_V^L &= \frac{v_{tq}}{2}, & f_V^R &= f_T^L = f_T^R = 0 \\ v_{tt}^Z &= \frac{1}{2} - 2Q_t \sin^2 v_W, & a_{tt}^Z &= \frac{1}{2} \\ v_{tt}^Z &= a_{tq}^Z = 0, & q &\neq t \end{aligned} \right\} \quad (6)$$

The experimental results are presented in terms of restrictions on the values of the anomalous coupling constants  $k$  in (4). In a number of cases the obtained constraints are re-expressed through limits on the probabilities of certain rare decays of the

$t$ -quarks. To explain the above, let us consider a typical (and very promising) example of such an anomalous interaction in the vertex  $tWb$  (see Figure 1). In the CM, such a vertex describes the interaction of the "left"  $t$ -quark and has the form:

$$L_{SM} = \bar{\psi}_q \hat{O}_{SM} \psi_t; \hat{O}_{SM} = \psi_t \frac{e}{2\sqrt{2}\sin\theta_W} V_{tb} \gamma^\mu (1 - \gamma^5);$$

$$\frac{e}{2\sqrt{2}\sin\theta_W} = M_W \sqrt{\frac{G_F}{\sqrt{2}}}$$

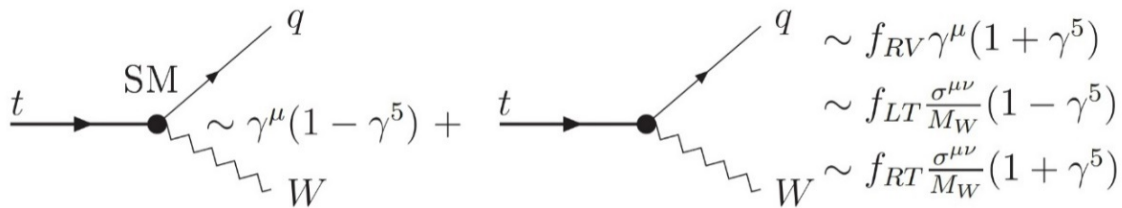


Figure 1 – Anomalous interaction at the vertex  $tWb$  [15]

At such interaction vertices the effects of so called New Physics can be manifested in the presence of "right" currents and anomalous magnetic and electrical moments. We can introduce a possible deviations from the SM by using the model-independent approach in

terms of all possible Lorentz-invariant structures in the effective  $tWb$  interaction Lagrangian.

2.3 Basic mechanisms of top-quark production

Total width of  $t$ -quark calculated in the NLO approximation is [5]:

$$\Gamma_t = \frac{G_F m_t^3}{8\pi\sqrt{2}} \left(1 - \frac{M_W^2}{m_t^2}\right)^2 + \left(1 + 2 \frac{M_W^2}{m_t^2}\right) \left[1 + \frac{2\alpha_s}{3\pi} \left(\frac{2\pi^2}{3\pi} - \frac{5}{2}\right)\right] \tag{7}$$

Within the Standard Model, the main mechanisms for the production of  $t$ -quarks in terms of the corresponding cross sections in hadron interactions are the gluon – gluon and quark –

antiquark annihilation leading to the formation of  $t\bar{t}$  couple (see Figure 2):

$$gg \rightarrow t\bar{t} \tag{8}$$

$$q\bar{q} \rightarrow t\bar{t}. \tag{9}$$

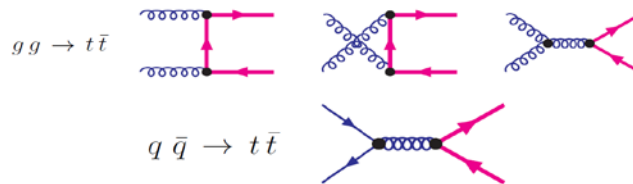


Figure 2 – Diagrams describing the formation of a couple  $t\bar{t}$ -quarks [15]

The next processes in terms of cross-section are electroweak ("single")  $t$ -quark production. These processes are usually classified according to the

magnitude of the square of the 4-momentum of the virtual W-boson participating in the process (see Figure3):

$$qb \rightarrow tq', p_W^2 < 0 \quad : t\text{-channel} \tag{10}$$

$$q\bar{q}' \rightarrow t\bar{b}, p_W^2 > 0 \quad : s\text{-channel} \tag{11}$$

$$gb \rightarrow tW, p_W^2 = M_W^2 \quad : tW\text{-channel} \tag{12}$$

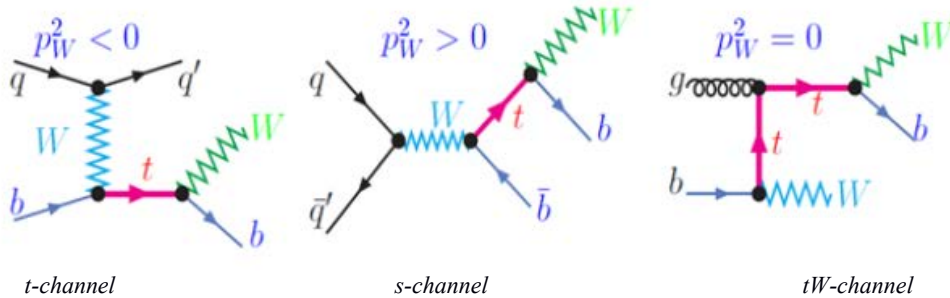


Figure 3 – Representative diagrams which describe the sub-processes of electroweak production of  $t$ -quarks [15]

### 3 Experimental searches of top quark

#### 3.1 Top quark mass measurement

The first measurements of the cross-sections and mass of the  $t$ -quark were carried out at the Tevatron collider (Fermilab, USA) in 1995. The CMS and ATLAS experiments of LHC have been measured the mass of the  $t$ -quark at different energies, as well as in various decay channels by different methods.

- The most accurate  $t$ -quark mass is measured in the distribution over the invariant mass of the decay products of the reconstructed  $t$ -quark:

$$t \rightarrow bW \rightarrow j_b jj \Rightarrow M(j_b'' W''(jj)),$$

$$t \rightarrow bW \rightarrow j_b l^\pm \nu \Rightarrow M_T(l E_T^{miss}).$$

- The  $t$ -quark mass can also be determined by examining the correlations of the distribution of the decay products. For example, in the decays

$$t \rightarrow bW, b \rightarrow B(b\bar{q}) \rightarrow J/\psi X, \\ W \rightarrow l^\pm \nu \rightarrow M(l^\pm J/\psi).$$

- It is also possible to determine the  $t$ -quark mass from the total cross-section for the production of  $t\bar{t}$ -quarks:

$$\sigma(pp \rightarrow t\bar{t}) = f(m_t).$$

Figure 4 shows an example of "measurement" of  $t$ -quark mass from the spectrum  $M(l^\pm J/\psi)$  and  $pp \rightarrow t\bar{t}$ .

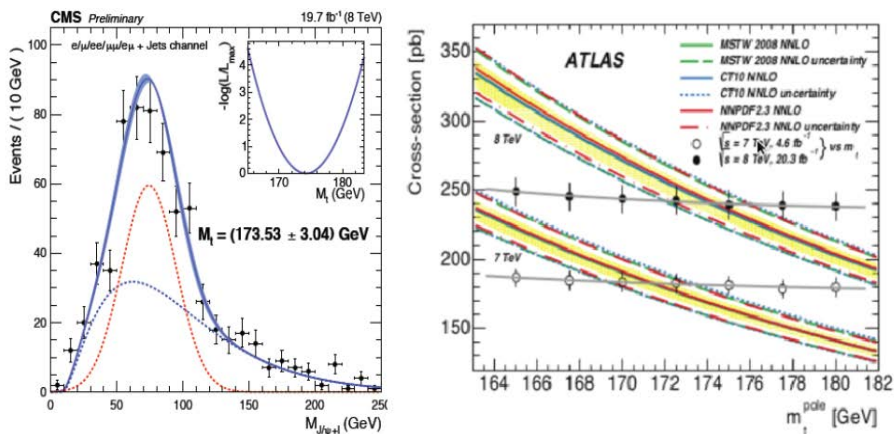


Figure 4 – Measurement results for the  $t$ -quark mass from the spectrum  $M(l^\pm J/\psi)$  and  $pp \rightarrow t\bar{t}$  [16]

In Figure 5 it is given the results of mass measurements of the  $t$ -quark with the decay channel combinations, as well as the total results from the experiments. This data was collected by the LHC group [16]. You can see that at the end of 2017 the  $t$ -quark mass has already been

measured independently with an accuracy of about 0.5 GeV (0.3%). From the CMS experiment  $\Delta = m_t - m_{\bar{t}} = -0.15 \pm 0.19(stat) \pm 0.09(syst)$  [17]. Within the framework of measurement errors, the mass of the  $t$ -quark and antiquark coincide.

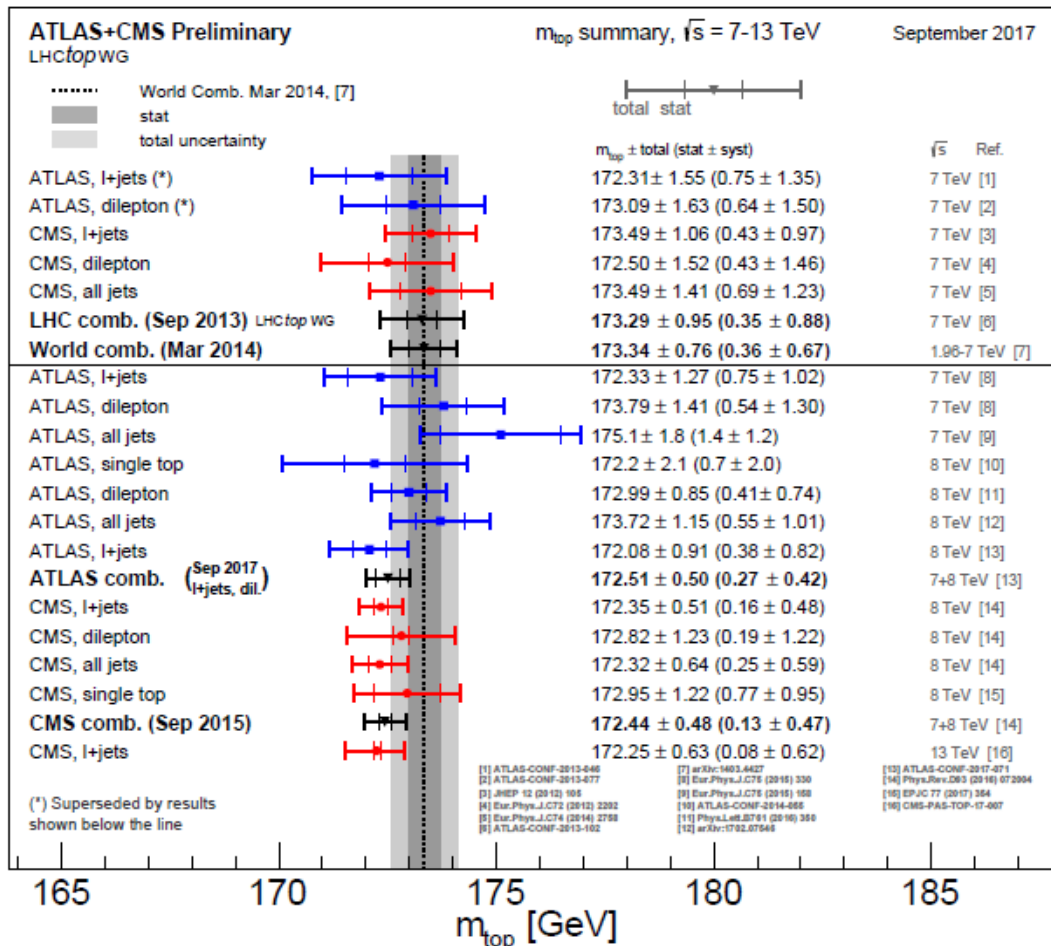


Figure 5 – Measurements of the  $t$ -quark mass in the CMS and ATLAS experiments in different  $t$ -quark decay channels and at different energies. The results of combining measurements in different channels are presented [16]

### 3.2 Top quark width measurements

To measure the width of a  $t$ -quark, it is necessary to study the distributions of the number of events over the  $M(bW)$  invariant mass of its decay products. The peak in this distribution determines the mass of the  $t$ -quark, and the width of the distribution determines the total width  $\Gamma_t$  of the decay.

However, such fitting of the distribution over  $M(bW)$  does not give an acceptable accuracy (in the lepton mode of W-boson decay due to the presence of an unregistered neutrino; in the hadron channel of

W-boson decay, the distribution is blurred by the combinatorial factors of jet permutation during the reconstruction of  $t$ -quarks). In the ATLAS [18] experiment, the  $t$ -quark width was measured by quoting the invariant mass of a charged lepton and a  $b$ -quark in the processes of paired  $t$ -quark generation. At the same time, signal events with different values (from 0.1 to 5.0 GeV in increments = 0.1 GeV) were generated to determine the width  $\Gamma_t$ . The value of  $\Gamma_t$  was determined from the minimum value of the negative logarithm of probability (see Figure 6).

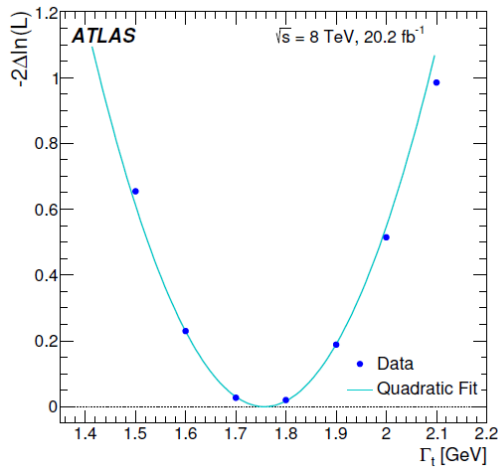


Figure 6 – Determination of the width  $\Gamma_t$  from the distribution of the negative logarithm of the probability [18]

In the CMS experiment [19] an indirect measurement of the width of the  $t$ -quark was carried out from the determined measurements of the decay probabilities of the  $t$  quark in pair production and the measurements of the cross-section for the electroweak production of the  $t$ -quark:

$$\Gamma_t = \frac{\sigma_{t-ch}^{exp}}{B(t \rightarrow Wb)} \times \frac{\Gamma^{th}(t \rightarrow Wb)}{\sigma_{t-ch}^{th}}$$

where  $\sigma_{t-ch}^{exp}(\sigma_{t-ch}^{th})$  is the measured (theoretical) value of the cross-section for the production of a single  $t$ -quark,  $\Gamma^{th}(t \rightarrow Wb) = 1.329 \text{ GeV}$  is the theoretical value of the decay width  $t \rightarrow Wb$  (calculated at  $t = 172.5 \text{ GeV}$  [5]).

The measurement results are given in Table 1.

Table 1 – Measured values of  $\Gamma_t$ , in experiments ATLAS [18] and CMS [19]

Experiment	$\Gamma_t^{exp}, \text{ GeV}$
ATLAS	$\Gamma_t = 1.76 \pm 0.33 \text{ (stat.)}_{-0.68}^{+0.79} \text{ (syst.)}$
CMS	$\Gamma_t = 1.36 \pm 0.03 \text{ (stat.)}_{-0.11}^{+0.14} \text{ (syst.)}$

A new theoretical method to measure the  $t$ -quark width was proposed in [20] by comparing invariant mass distributions below and above  $t$ -quark pair and single  $t$ -quark thresholds.

### 3.3 Coupling constant of the top quark and Higgs boson

The next important point is the calculation of the coupling constant of the Higgs boson with the  $t$ -quark ( $y_t$ ). It plays an important role in the SM as well as in its extensions. The value of this parameter can be measured in the reactions of pair and single production of  $t$ -quarks accompanied by the Higgs boson:

$$(t\bar{t}H) \quad pp \rightarrow tH\bar{t}X \quad (13)$$

$$(tH) \quad pp \rightarrow tHX \quad (14)$$

The different decay modes of the Higgs boson were studied experimentally:  $H \rightarrow b\bar{b}, WW^*, ZZ^*, \tau^+\tau^-, \gamma\gamma$ . Results of measurements of the parameter  $y_t$  are presented in Table 2.

Table 2 – The magnitude of the coupling of the Higgs boson with the  $t$ -quark

ATLAS[21]	CMS[22]
$y_t = 1.15 \pm 0.12$	$126_{-0.26}^{+0.31}$

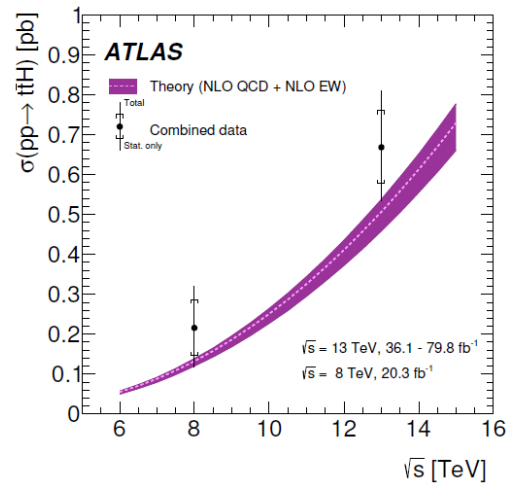


Figure 7 – Cross section for production of the Higgs boson accompanied by  $t$ - and  $t$ -quarks [21]

### 3.4 Top-quark pair production reactions

Within the Standard Model by using the known mass of the  $t$ -quark, it is possible to calculate the cross sections for the processes of its production and compare with the experimental values. In Figure 8 it is given the results of measuring the cross section for the pair production of the  $t$ -quark [16] obtained by the CMS and ATLAS experiments in different

decay channels at different energies. The theoretical results of the cross sections obtained within the SM and the results from the experiments are in good agreement.

3.5 Processes of a single  $t$ -quark production and a few rare  $t$ -quark production processes

The processes of pair production of  $t$ -quarks have the largest cross section. The processes of single  $t$ -quark generation are the next in terms of the cross-section. In Figure 9 it is shown the results of the cross section measurements for a single  $t$ -quark production in  $t$ -,  $tW$ - and  $s$ -channels [16]. Due to the very small value of the cross section and the huge background, the registration of the  $s$ -channel process of a single  $t$ -quark production presents significant complexity at the LHC, in contrast to the

Tevatron collider, where this cross section approximately corresponds to the  $t$ -channel process of a single production. The presented results demonstrate excellent agreement between the SM predictions for a single electroweak  $t$ -quark production and the measurements.

It was carried out calculations for more rare processes with the  $t$ -quark production. Obtained results are in Figure 10. It is shown the cross sections measured both in the SM and in the CMS experiment for the processes of pair  $t$ -quarks production in association with gauge bosons and Higgs boson,  $b$ -quark pair, as well as the production of four-quarks [23]. The shown level of measurement errors makes it possible to judge the current measurement sensitivity in the  $t$ -quark sector at the LHC.

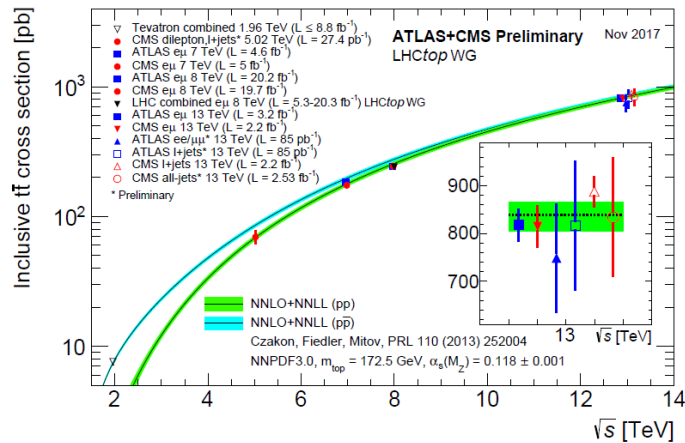


Figure 8 – Cross sections for  $t$ -quark pair production measured in the CMS and ATLAS experiments in different  $t$ -quark decay channels and at different energies. The blue lines show the values of the cross sections calculated within the framework of the SM, the measurement error is highlighted in color [16]

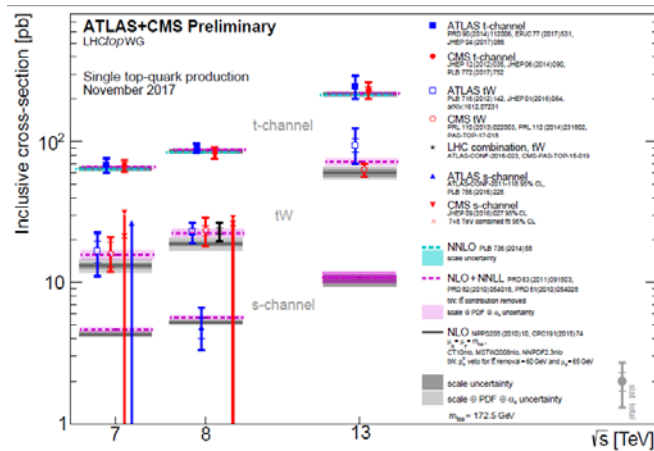
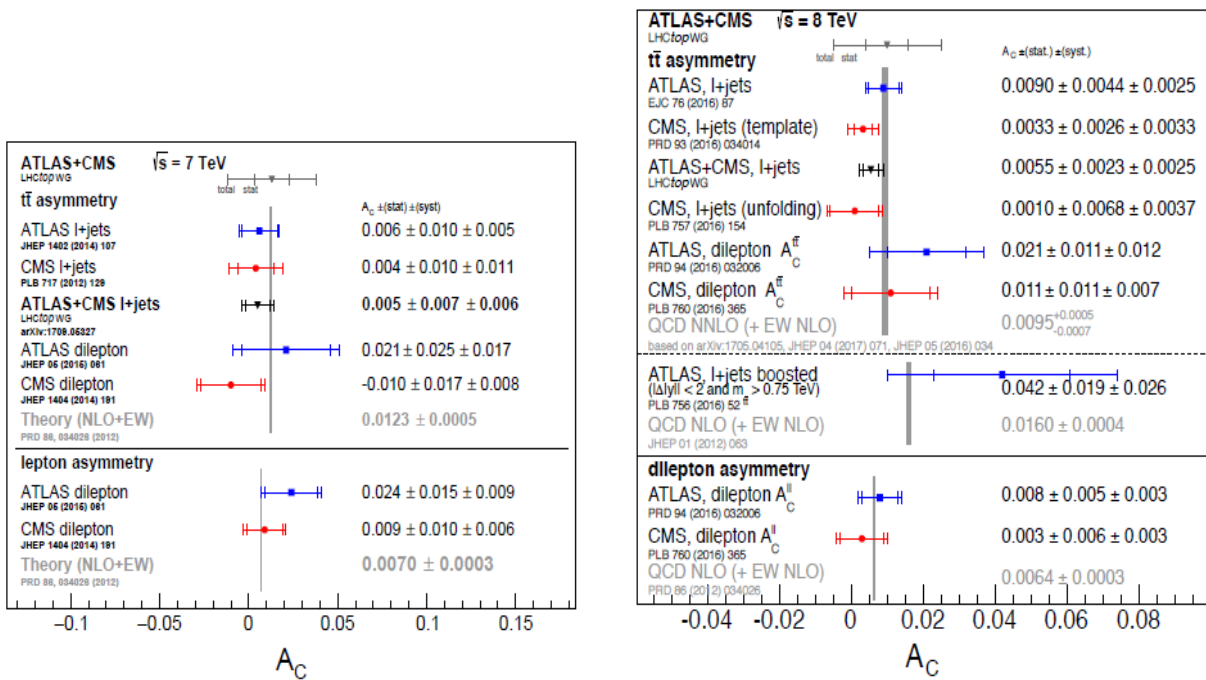
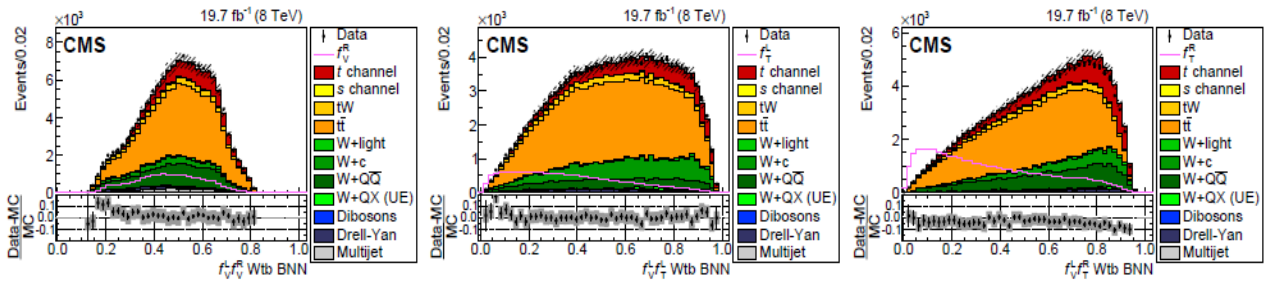


Figure 9 – The cross sections for a single  $t$ -quark production are given, measured in the CMS and ATLAS experiments in various channels of electroweak  $t$ -quark production at different energies. The cross sections calculated in the framework of the Standard Model are shown, with the corresponding error marked with a colored region [16]





**Figure 11** – The measured and predicted SM values of the asymmetry of  $t$  to  $\bar{t}$  quark production in various experiments and of the production channel. The values obtained for collision energies of 7 TeV (left figure) and 8 TeV (right figure) are given [16]



**Figure 12** – Output distributions of Bayesian neural networks for CMS experimental data (points) and simulated processes that contribute to the investigated final state (contribution of exact process corresponds to the area marked with the corresponding color). The lines show the distributions of events for possible effects of New Physics corresponding to the contribution of the right vector (left figure), left tensor (middle figure) and right tensor (right figure) currents. The shaded area shows the full systematic uncertainty of the simulation. The vertical line shown together with the data distribution points corresponds to the value of the statistical uncertainty of the measurement [26]

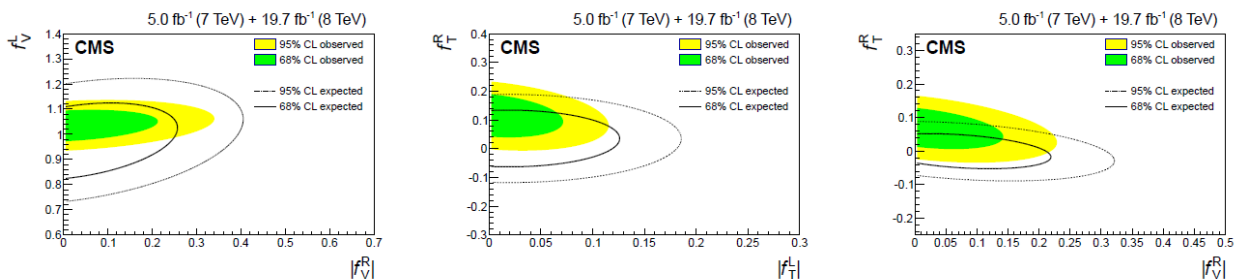


**Figure 13** – The contours of the upper bounds on the parameters obtained which characterize the possible effects of New Physics in the  $tWb$  vertex. It is shown the expected (lines) and observed (colored areas) limitations with the statistical confidence of 68% and 95% [26]

The similar analysis was carried out at ATLAS experiment [27] on the basis of studying the asymmetry of the kinematic characteristic which presents the correlation of spin states in the production and decay of the  $t$ -quark. The asymmetry is a consequence of the exchange of the left charged current in the  $tWb$  vertex and is sensitive to the possible contributions of other currents. In addition to direct search for anomalous currents in the  $tWb$  interaction, the limits on the

contribution of such anomalous currents are established by the help of measurement of the chiral states of the  $W$  boson. The contours of the upper limitations obtained in the ATLAS experiment [28] are shown in Figure 14. These limitations are on the parameters characterizing the possible contributions of left tensor ( $g_L = f_T^L$ ), right vector ( $V_R = f_V^R$ ) and right tensor ( $g_R = f_T^R$ ) currents normalized to the contribution of left vector currents  $V_L = f_V^L$ .

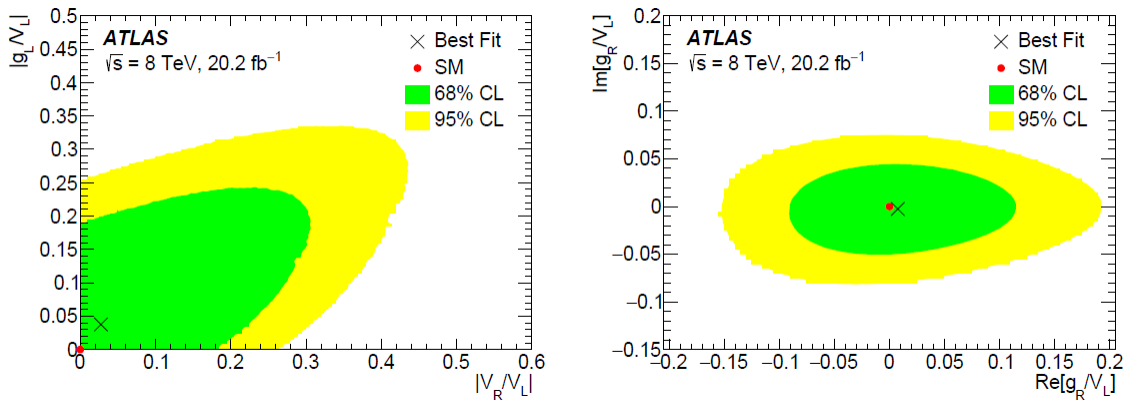


**Figure 14** – The contours of the upper bounds on the parameters obtained in the ATLAS experiment, which characterize the possible effects of New physics in the  $tWb$  vertex. Restrictions on the possible contributions of the left tensor  $g_L \equiv f_T^L$ , right vector: ( $V_R$ ) and right tensor  $g_R \equiv f_T^R$  currents are given, normalized to the contribution of left vector currents  $V_R \equiv f_V^R$  present in the SM [28]

#### 4.2 Investigations of rare processes with top quarks

The processes with the flavor changing neutral currents (FCNC) are strongly suppressed within the Standard Model. But the probability of such processes can be increased by the extensions of the SM. As well as an experimental searches was done for  $t$ -quark interactions with FCNC by the exchange of gluons,  $Z$  boson, photon, or Higgs boson. A number of production

or decay processes of a  $t$ -quark with FCNC were investigated.

Figure 15 shows the results of CMS and ATLAS experiments [16]. Predictions of the SM labeled by the black line. The points label the upper limits on the probabilities of rare decays obtained in the CMS and ATLAS experiments. The dashed areas show theoretical predictions beyond the CM. The obtained restrictions on the FCNC interactions of top quarks [16] are given in Table 3.

**Table 3** – Limitations on the probability of  $t$ -quark decays [26, 29-33]

Decay	B(95% CL)	
	ATLAS	CMS
$t \rightarrow Hu$	$1.9 \times 10^{-3}$	$4.7 \times 10^{-3}$
$t \rightarrow Hc$	$1.9 \times 10^{-3}$	$1.9 \times 10^{-3}$
$t \rightarrow gu$	$4.0 \times 10^{-5}$	$2.0 \times 10^{-5}$
$t \rightarrow gc$	$20.0 \times 10^{-5}$	$41 \times 10^{-5}$
$t \rightarrow \gamma u$		$130 \times 10^{-5}$
$t \rightarrow \gamma c$		$170 \times 10^{-5}$
$t \rightarrow Zu$	$17 \times 10^{-5}$	$22 \times 10^{-5}$
$t \rightarrow Zc$	$24 \times 10^{-5}$	$44 \times 10^{-5}$

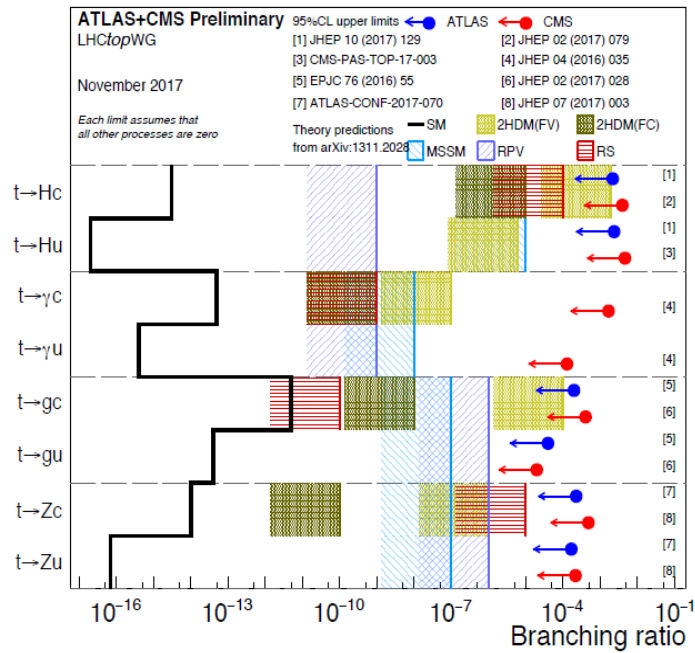


**Figure 15** – The generalized results of CMS and ATLAS experiments which was carried out for the searches of flavor changing neutral currents. The results are presented as limitations on the probabilities of rare  $t$ -quark decays involving the flavor changing neutral currents vertices. The SM predictions are labelled by the black line. The points show the upper limits of the probabilities of rare decays. The shaded areas represent the predictions of various theories beyond the SM [16]

### 5 Main projects of future accelerators

The  $t$ -quark has been observed at Tevatron and LHC accelerators in proton-antiproton and proton-proton collisions respectively. At an early date it is planned to study the  $t$ -quark at HL-LHC project [34, 35], which represents a significant modernization of the LHC. The main goal of this is to increase the luminosity of the accelerator by 10 times in comparison with LHC and to increase the total center-of-mass energy of the proton-proton collision ( $\sqrt{s_{pp}} = 14TeV$ ).

The project annual integrated luminosity of HL-LHC for the CMS and ATLAS installations is

$$L_{tot} = 300fb^{-1}$$

which means approximately 3 billion paired and 1 billion single  $t$ -quark production events over the full design life of the accelerator over ten years. For a comparison, during 2017 year an integrated luminosity of  $45fb^{-1}$  was obtained at the CMS facility.

The main characteristics of the LHC and future accelerators are listed in Table 4. The behavior of the cross sections for  $t\bar{t}$  production of a pair of quarks and single production of  $t$ -quarks are shown in Figure 16.

**Table 4.** Comparison of the main characteristics of LHC and future accelerators [34, 36, 37]. We listed the center of mass energy of colliding particles, the peak luminosity  $L$  and the integral luminosity  $\int L$ , the average number of accompanying interactions  $\langle \mu \rangle$  for a single intersection of bunches

Accelerator	$\sqrt{s}, TeV$	$L, cm^{-2} \cdot c^{-1}$	$\int L, ab^{-1}$	$\mu >$
LHC	7-13	$\approx 10^{34}$	0.3	10-40
HL-LHC	14	$10^{35}$	3	140-200
HE-LHC	27	$2.5 \times 10^{35}$	12	800
SppC	75	$1.2 \times 10^{35}$	15	400-500
FCC-hh	100	$3 \times 10^{35}$	30	500-1000

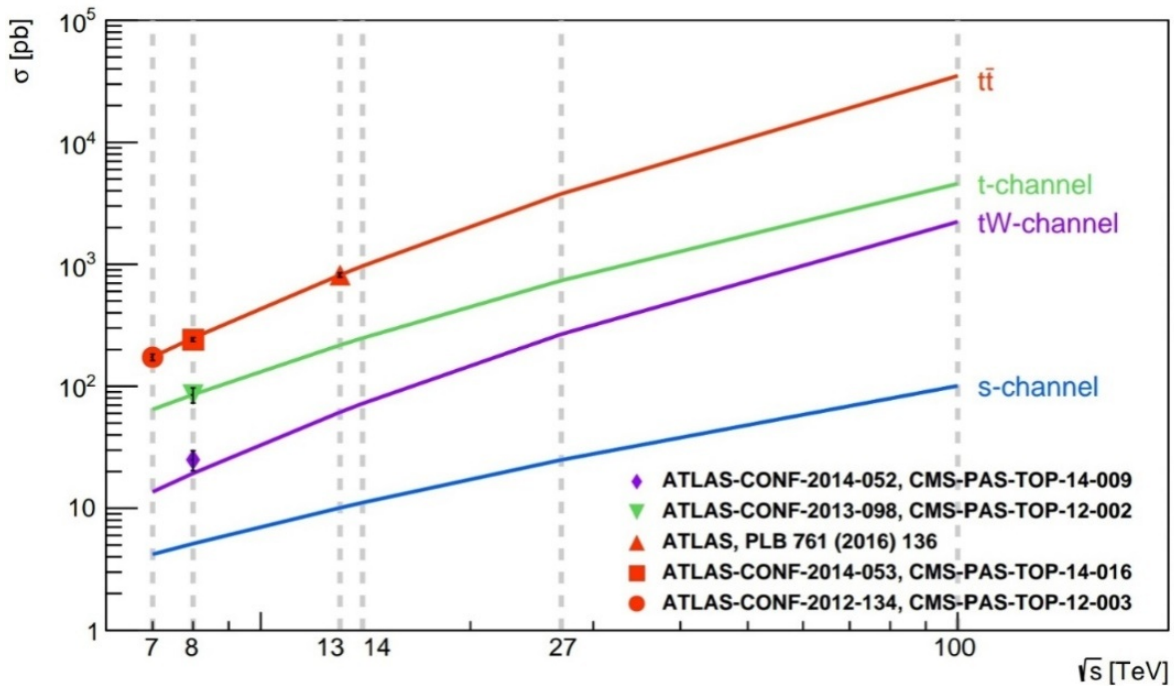


**Figure 16** – Plot of  $t$ -quark production cross section versus of the total energy of colliding protons in the system of centers of mass for the processes of paired and single production in the  $s$ -,  $t$ -,  $tW$  – channels according to NLO calculations in MCFM. The experimental data were taken from [38-45]

Another accelerator is the developing FCC-hh accelerator. The nearest possible launch date for this accelerator may be 2043 year.

The main goal of this project is to create a proton-proton collider capable of achieving a record value of collision energy in the center-of-mass system equal to 100 TeV. Also planned to create the electron-electron accelerator FCC- $ee$ , as an intermediate stage in the development of FCC- $hh$  and the accelerator HE-LHC. Proton-proton collider HE-LHC uses the existing LHC tunnel and obtains the energy of 27 TeV by using the technology of FCC-hh accelerator [36].

## Conclusion

The  $t$ -quark is the heaviest elementary particle in the Standard Model and plays a unique role in particle physics. Due to large mass of the  $t$ -quark and extremely short lifetime There are no hadrons consisting of a  $t$ -quark in nature. Lifetime of the  $t$ -quark is much shorter than the time required for the creation of quark-antiquark bound states from the vacuum and the formation of hadrons. So it gives the possibility to study the fundamental properties of a  $t$ -quark that are not masked by hadronization

effects. Predictions of the characteristics of various interactions involving the  $t$ -quark have high theoretical accuracy, as well as  $t$ -quark has large production cross section which makes it a unique laboratory for testing the Standard Model and beyond. In experiments at the LHC in the first and second sessions of operation, the  $t$ -quark mass, the cross sections for pair and single production, the mixing parameter  $V_{tb}$ , various distributions and spin correlations, and the cross sections for processes with a dominant contribution of virtual  $t$ -quarks have already been measured with a sufficiently high accuracy as the creation of the Higgs boson in a gluon-gluon fusion, the constants of the Yukawa interaction with the Higgs boson, and others. We determine the restrictions on the anomalous parameters of the interactions of the  $t$ -quark with gauge bosons, on the masses various resonances decaying into states containing an  $t$ -quark, into the parameters of theoretically possible interactions with violation of flavor.

The top quark is a key element in almost all SM extensions. We expect that the study of  $t$ -quarks will continue to be that portal that leads to new discoveries and will allow us to take a new step in understanding the structure of the depths of matter.

This will also mean a qualitatively new level in understanding the structure of the Universe, because in the first instant after its birth, various processes took place in the Universe, in particular, processes involving the  $t$ -quark.

The top quark is a key element in almost all CM extensions. We expect that the study of the  $t$ -quark will continue to be that portal which leads to new discoveries and will allow us to take a new step in understanding the structure of matter in depths. This will also mean a qualitatively new level in understanding the structure of the Universe, since in the first moment after its birth, various processes took place in the Universe, in particular, processes involving the  $t$ -quark.

### Acknowledgements

This work was supported by the Ministry of Education and Science of the Republic of Kazakhstan, Grant IRN AP09058640 “Physics beyond the Standard Model in processes involving the top quark and Higgs boson”.

### References

- 1 Beneke M., Altarelli G., Mangano M. L. “Top quark physics in Standard model physics (and more) at the LHC.” *arXiv:hep-ph/000303*, Vol.99 (2000): 110.
- 2 Abachi S. «Observation of the top quark.» *Phys.Rev.* Vol.74 (1995): 6.
- 3 Abe F. «Observation of top quark production in  $\bar{p}p$  collisions.» *Phys.Rev.* Vol.74 (1995): 26.
- 4 Boos E.E., Brandt O., Denisov D., Denisov S.P., Grannis P. «The top quark (20 years after the discovery)», *Phys.Usp.* Vol.58 (2015): 25.
- 5 Patrignani C. «Particle Data Group» *Chin.Phys.* Vol.40 (2016) and (2017) update.
- 6 Cabibbo N. «Unitary symmetry and leptonic decays» *Phys.Rev.* Vol.10 (1963): 531.
- 7 Kobayashi M., Maskawa T. «CP-violation in the renormalizable theory of weak interaction» *Prog.Theor.Phys.* Vol.49 (1973): 652.
- 8 Borodulin V.I., Rogalyov R.N., Slabospitskii S.R. CORE 3.1(Compendium of RELations, Version 3.1), arXiv:1702.08246 [hep-ph].
- 9 Buchmuller W., Wyler D. «Effective Lagrangian Analysis of New Interactions and Flavor Conservation», *Nucl.Phys.* Vol.268 (1986): 621.
- 10 Aguilar-Saavedra J.A. «A Minimal set of top anomalous couplings» *Nucl.Phys.* Vol.812 (2009): 181.
- 11 Grzadkowski B., Iskrzynski M., Misiak M., Rosiek J. «Dimension-Six Terms in the Standard Model Lagrangian» *JHEP* Vol.10 (2010): 085.
- 12 Aguilar-Saavedra J. A. «Interpreting top-quark LHC measurements in the standard-model effective field theory» *arXiv:1802.07237 [hep-ph]*.
- 13 Kane G.L., Ladinsky G.A., Yuan C.P. «Using the Top Quark for Testing Standard Model Polarization and CP Predictions» *Phys.Rev.* Vol.45 (1992): 124.
- 14 Hollik W., Illana J.I., Rigolin S., Schappacher C., Stockinger D. «Top dipole form-factors and loop induced CP violation in supersymmetry», *Nucl.Phys.* Vol.551 (1999): 3.
- 15 Boos E., Dudko L., Mandrik P., Slabospitskii S. «Top Quark: Results and Prospects», *Physics of Particles and Nuclei*, Vol.50 No.3 (2019): 27.
- 16 LHC Top Working Group <https://twiki.cern.ch/twiki/bin/view/LHCPhysics/LHCTopWGSUMMARYPlots>
- 17 Chatrchyan S. «Measurement of the mass difference between top quark and antiquark in pp collisions at  $\sqrt{s} = 8\text{TeV}$ », *Phys.Lett.* Vol.770 (2017): 50.
- 18 Aaboud M. «Direct top-quark decay width measurement in the  $t\bar{t}$  lepton+jets channel at  $\sqrt{s} = 8\text{TeV}$  with the ATLAS experiment», *Eur.Phys.* Vol.78, no.2(2018): 129.
- 19 Khachatryan V. «Measurement of the ratio  $B(t \rightarrow Wb)/B(t \rightarrow Wq)$  in pp collisions at  $\sqrt{s} = 8\text{TeV}$ » *Phys.Lett.* Vol.736 (2014): 33.
- 20 Baskakov A., Boos E., Dudko L. «Model independent top quark width measurement using a combination of resonant and nonresonant cross sections» *Phys.Rev.* Vol.10 (2018) no.11: 98.
- 21 Aaboud M. «Observation of Higgs boson production in association with a top quark pair at the LHC with the ATLAS detector», arXiv:1806.00425 [hep-ex].
- 22 Sirunyan A.M. «Observation of  $t\bar{t}H$  production», arXiv:1804.02610 [hep-ex].
- 23 CMS Summary Plots, <https://twiki.cern.ch/twiki/bin/view/CMSPublic/PhysicsResultsTOPSummaryFigures>
- 24 Aaltonen T. «Evidence for a Mass Dependent ForwardBackward Asymmetry in Top Quark Pair Production», *Phys.Rev.* Vol.83 (2011):34.
- 25 Aaltonen T.A. «Combined Forward-Backward Asymmetry Measurements in Top-

Antitop Quark Production at the Tevatron», *Phys.Rev.* Vol.120, no.4 (2018): 1709.

26 Khachatryan V. «Search for anomalous Wtb couplings and avour-changing neutral currents in t-channel single top quark production in pp collisions at  $\sqrt{s} = 7$  and 8TeV», *JHEP* Vol.1702 (2017): 28.

27 Aaboud M. «Probing the W tb vertex structure in t-channel single-top-quark production and decay in pp collisions at  $\sqrt{s} = 8$ TeV with the ATLAS detector», *JHEP* Vol.124 (2017): 83.

28 Aaboud M. «Analysis of the hWtbvertex from the measurement of triple-differential angular decay rates of single top quarks produced in the t-channel at  $\sqrt{s} = 8$ TeV with the ATLAS detector», *JHEP* Vol.17 (2017): 1712.

29 Khachatryan V. «Search for anomalous single top quark production in association with a photon in pp collisions at  $\sqrt{s} = 8$  TeV» *JHEP* Vol.35 (2016): 1604.

30 Aad G. «Search for single top-quark production via avour-changing neutral currents at 8 TeV with the ATLAS detector» *Eur.Phys.* Vol.76 (2016) no.2: 55.

31 Sirunyan A.M. «Search for associated production of a Z boson with a single top quark and for tZ avour-changing interactions in pp collisions at  $\sqrt{s} = 8$  TeV» *JHEP* Vol.3 (2017): 1707.

32 Aaboud M. «Search for avour-changing neutral current top-quark decays  $t \rightarrow qZ$  in proton-proton collisions at  $\sqrt{s} = 13$  TeV with the ATLAS detector», arXiv:1803.09923 [hep-ex].

33 Aaboud M. «Search for avor-changing neutral currents n top quark decays  $t \rightarrow Hc$  and  $t \rightarrow Hu$  in multilepton nal states in proton\_proton collisions at  $\sqrt{s} = 13$  TeV with the ATLAS detector», arXiv:1805.03483 [hep-ex].

34 Apollinari G., Alonso I. B., Br O., Lamont M., Rossi L. «High-Luminosity Large Hadron Collider (HL-LHC): Preliminary Design Report» Vol.5. (2015): 5170.

35 Alonso I. B. «The Phase-2 Upgrade of the CMS Tracker» Vol.9. (2017): 14.

36 Benedikt M., Zimmermann F. «Proton Colliders at the Energy Frontier» *Nucl.Instrum.Meth.* Vol.1016 (2018):21.

37 Tang J. «Concept for a Future Super Proton-Proton Collider», arXiv:1507.03224 [physics.acc-ph].

38 CMS Collaboration [CMS Collaboration], «Combination of cross-section measurements of associated production of a single top-quark and a W boson at  $\sqrt{s} = 8$  TeV with the ATLAS and CMS experiments», CMS-PAS-TOP-14-009.

39 The ATLAS collaboration [ATLAS Collaboration], «Combination of cross-section measurements for associated production of a single top-quark and a W boson at  $\sqrt{s} = 8$  TeV with the ATLAS and CMS experiments», ATLAS-CONF-2014-052.

40 ATLAS and CMS Collaborations [ATLAS and CMS Collaborations], «Combination of single top-quark cross-sections measurements in the t-channel at  $\sqrt{s} = 8$  TeV with the ATLAS and CMS experiments», CMS-PAS-TOP-12-002, ATLAS-CONF-2013-098.

41 CMS Collaboration [CMS Collaboration], «Combination of ATLAS and CMS top quark pair cross section measurements in the  $t\bar{t}$  state using proton-proton collisions at 8 TeV», CMS-PAS-TOP-14-016.

42 The ATLAS collaboration [ATLAS Collaboration], «Determination of the top-quark pole mass using  $t\bar{t} + 1$ -jet events collected with the ATLAS experiment in 7 TeV pp collisions», ATLAS-CONF-2014-053.

43 Aaboud M. et al. «Measurement of the  $t\bar{t}$  production cross section using e events with b-tagged jets in pp collisions at  $\sqrt{s} = 13$  TeV with the ATLAS detector», *Phys.Lett.* Vol.761 (2017): 136. Erratum:

44 CMS Collaboration [CMS Collaboration], «Combination of ATLAS and CMS top-quark pair cross section measurements using proton-proton collisions at  $\sqrt{s} = 7$  TeV», CMS-PAS-TOP-12-003.

45 ATLAS Collaboration «Combination of ATLAS and CMS top-quark pair cross section measurements using up to 1.1 fb<sup>-1</sup> of data at 7 TeV» ATLAS-CONF-2012-134.

Sh.R. Myrzakul<sup>1,2\*</sup> , Y.M. Myrzakulov<sup>1,2</sup> , R. Yechshanova<sup>1</sup> , M. Imankul<sup>2</sup> 

<sup>1</sup>L.N.Gumilyov Eurasian National University, Nur-Sultan, Kazakhstan

<sup>2</sup>«Ratbay Myrzakulov Eurasian International Centre for Theoretical Physics» LLP, Nur-Sultan, Kazakhstan

\*e-mail: [smyrzakul@gmail.com](mailto:smyrzakul@gmail.com)

## Inflation in modified quantum gravity with a fermion field

**Abstract.** Viable inflation of modified nonuniform isotropic  $F(R)$  gravity with a fermionic field of  $f$ -essence is investigated using the quantum approach. The action of which is  $S = \int d^4x \sqrt{-g} [F(R) + L_m]$ , where  $R$  is the curvature scalar, and  $L_m$  is the matter Lagrangian. In this case, we consider a non-minimally coupled fermionic field  $f$ -essence, the Lagrangian of which is denoted by  $K(Y, u)$  by a function depending on  $Y$ -kinetic and  $u$  potential arguments. The equations of motion of this model are obtained for the homogeneous and isotropic Friedman-Robertson-Walker space-time. As  $F(R)$  we consider the generalized Horava-Lifshitz quantum gravity function. In 2009, Horava proposed a new approach to studying membranes in the theory of quantum gravity, known as the Horava-Lifshitz gravity. The peculiarity of Horava-Lifshitz gravity is that it is renormalizable. Further, the particular case of  $K(Y, u) = \ln Y + u$  is investigated in detail. The parameters of describing the current accelerated expansion of the Universe are obtained and the explicit form of the connection of matter with space-time  $h(u)$  is determined. The inflationary period of the evolution of this model is also investigated. To describe the inflationary period, the form of the Hubble parameter and the slow roll-off parameter, as well as other inflationary parameters, were determined. The presented results are compared with the observation results. The analysis of the results coincides with the observation data at certain values of the integral constants in the solutions.

**Key words:**  $f$ -essence, inflation, Friedman-Robertson-Walker metric, Horava-Lifshitz gravity,  $F(R)$  gravity.

### Introduction

At present, from observations of type Ia supernova explosions [1,2], it became known about the accelerated expansion of the Universe. Scientists believe that the reason for this phenomenon is the strength of the alleged hypothetical "dark energy". After the birth or the so-called Big Bang, our Universe also expanded rapidly. Scientists called this era inflation. However, there is still no unified theory describing these periods of the evolution of the Universe. In an attempt to create such a theory, scientists have proposed various models. These models can be divided into two main classes: this is a modification of Einstein's theory of relativity or the introduction of a previously unknown substance of "dark energy"

In addition, due to the difficulties of constructing a general theory *взаимосвязь* that unifies the two fundamental theories of general relativity and quantum mechanics, it also led to a

modification of the theory of gravity. Meanwhile, it is assumed that matter fields (bosons and fermions) arise from superstructures (for example, Higgs bosons or superstrings), which, undergoing certain phase transitions, generate known particles. With that it is assumed that geometry (for example, the Ricci tensor or the Ricci scalar) interacts directly with the quantum fields of matter. This interaction necessarily modifies the standard theory of gravity, that is, the Lagrangian of gravity plus the effective fields are modified compared to the Einstein field.

Since 2009, the quantum theory of gravity by Horava-Lifshitz has established [3]. This approach is most likely manifested. Based on this approach the influence of communication in the dimension of space-time. This approach takes into account the influence of relationships when assessing spatial and temporal characteristics. One of the main characteristics of this formulation is to abstain from specific Lorentz invariance so that it can be recreated when considering low energies as an

approximate symmetry. Although this theory describing gravity is fundamental, some problems remain unanswered (for example [4-9]) related to detailed balance, with strong couplings, an extra spread degree of freedom of dissemination, the limit of general relativity (infrared), a relationship with alternative gravitational theories and other problems. Moreover, the investigation of Horava-Lifshitz gravity in the spatially flat Friedman-Robertson-Walker cosmology (FRW) determine that its describing cosmology [10] is analogical with ordinary general relativity. Although effective dark matter can act as a kind of integration constant in Horava-Lifshitz gravity. Consequently, there is no natural way (without additional fields) to obtain an accelerating Universe from Horava-Lifshitz gravity, let alone a unified description of early inflation with late time acceleration.

Inflation was proposed by Guth and Sato [11-13] several years ago to address the initial conditions of the Friedman universe, and today the idea is well accepted, according to which the Universe has undergone a period of strong accelerated expansion after the Big Bang. Although the arena of early acceleration models is quite large, the constraints that a theory must satisfy in order to reproduce the latest cosmological data [14,15] are rather restrictive (see [16-20] for a general overview of inflation).

Inflation occurs in Planck time ( $\sim 10^{-35/-36}$  seconds) and leads to thermalization of the observable Universe: as it accelerates expansion, the small initial velocities within the causal area become very large, and the horizon and flatness problems can be well explained. To cause acceleration, repulsive gravity is needed. All data indicate that

inflation was realized with the help of the (quasi) de Sitter solution, but for the restoration of a Universe dominated by radiation / matter, a mechanism for a quick exit from the acceleration regime is necessary.

In this paper, we investigate the inflation of modified quantum gravity with a fermionic field. The generalized  $F(R)$  Horava-Lifshitz gravity is considered as a modified quantum theory of gravity.

**Model.** Let's first examine the dynamics of the  $f$ -essence for the quantum model of  $F(R)$  gravity at FRW space-time

$$ds^2 = -c^2 dt^2 + a(t)^2 \sum_{i=1}^3 (dx^i)^2, \quad (1)$$

where  $a(t)$  is the scale factor.

The action for  $F(R)$  gravity is given as follows

$$S = \int d^4x e [F(R) + L_m], \quad (2)$$

here  $e = \det(e_\mu^i) = \sqrt{-g}$ ,  $R$  is the curvature scalar and  $L_m$  is the matter Lagrangian. The generalized Horava-Lifshitz curvature proposed in [21] is considered as the curvature of space-time:

$$R = 3(1 - 3\lambda + 4\mu) \frac{\dot{a}^2}{a^2} + 6\mu \frac{\ddot{a}}{a}, \quad (3)$$

where the dot means the time derivative.

According to [21], consider the action described above as a representation of a evaluation system in which  $a$  – scale factor and  $R$  – scalar curvature are executed as independent non-stationary variables. Thus, action (2) can be rewritten as

$$S = \int L(a, \dot{a}, R, \dot{R}) dt = \int \left\{ a^3 h(u) F(R) - \nu \left[ R - \left( 3(1 - 3\lambda + 4\mu) \frac{\dot{a}^2}{a^2} + 6\mu \frac{\ddot{a}}{a} \right) + 2K(Y, u) \right] \right\} dt \quad (4)$$

where  $K(Y, u)$  is the Lagrangian of the  $f$ -essence,  $u = \bar{\psi} \psi$ ,  $\psi = (\psi_0, \psi_1, \psi_2, \psi_3)^T$  is a function of the fermionic field, and  $\bar{\psi} = \psi^\dagger \gamma^0$  denotes its conjugate function,  $\nu = a^3 dF(R)/dR$  is the Lagrange multiplier and can be determined by changing the Lagrangian with respect to the scalar, which gives  $\nu = a^3 F'$ ; in what follows, the curvature derivative  $R$  will be denoted by a prime.

In addition, the kinetic part is determined by the following expression:

$$Y = \frac{1}{2} i \left[ \bar{\psi} \Gamma^\mu D_\mu \dot{\psi} - (D_\mu \bar{\psi}) \Gamma^\mu \dot{\psi} \right] \quad (5)$$

here the differential operator  $D_\mu$  is defined as the covariant derivative and  $\Gamma^\mu = e_i^\mu \gamma^i$ . Dirac matrices  $\Gamma^\mu$  of curved space-time:

$$\begin{aligned} \Gamma^0 &= \gamma^0, \\ \Gamma^j &= a^{-1}\gamma^j, \\ \Gamma^5 &= -i\sqrt{-g}\Gamma^0\Gamma^1\Gamma^2\Gamma^3 = \gamma^5, \\ \Gamma_0 &= \gamma^0, \\ \Gamma_j &= a\gamma^j, \quad (i=1,2,3), \end{aligned} \quad (6)$$

$$\begin{aligned} \dot{\bar{\psi}} + \frac{1}{2}\left(3H + \frac{\dot{K}_Y}{K_Y}\right)\bar{\psi} - i\frac{K_u}{K_Y}\bar{\psi}\gamma^0 - \\ - \frac{i}{2}\left[\frac{F}{F'} - R + 6(2H^2 + \dot{H})\right]\frac{Fh_u}{K_Y}\bar{\psi}\gamma^0 = 0, \end{aligned} \quad (11)$$

where the gamma matrices are of the form

$$\begin{aligned} \gamma^0 &= \begin{pmatrix} I & 0 \\ 0 & -I \end{pmatrix}, \quad \gamma^k = \begin{pmatrix} 0 & \sigma^k \\ -\sigma^k & 0 \end{pmatrix}, \\ \gamma^5 &= \begin{pmatrix} 0 & I \\ I & 0 \end{pmatrix}, \end{aligned} \quad (7)$$

where  $I = \text{diag}(1, 1)$  and  $\sigma^k$  are Pauli matrices, defined as

$$\begin{aligned} \sigma^1 &= \begin{pmatrix} 0 & 1 \\ 1 & 0 \end{pmatrix}, \quad \sigma^2 = \begin{pmatrix} 0 & -i \\ i & 0 \end{pmatrix}, \\ \sigma^3 &= \begin{pmatrix} 1 & 0 \\ 0 & -1 \end{pmatrix}. \end{aligned} \quad (8)$$

Then the kinetic part for the FRW metric takes the form

$$Y = \frac{1}{2}i(\bar{\psi}\gamma^0\dot{\psi} - \dot{\bar{\psi}}\gamma^0\psi). \quad (9)$$

Finally, the effective Lagrangian from action (4) has the form

$$\begin{aligned} L &= a^3 hF + hF'a^3 R - 3(1-3\lambda)\dot{a}^2 ahF' + \\ &+ 6\mu\dot{a}^2 h_u \dot{u}F' + 6\mu\dot{a}^2 hF''\dot{R} + 2a^3 K, \end{aligned} \quad (10)$$

subscripts denote derivatives with respect to the given parameters.

Using the Euler-Lagrange method to (10), we obtain the equations of motion for the spinor field and the complex field conjugate to

$$\begin{aligned} \dot{\psi} + \frac{1}{2}\left(3H + \frac{\dot{K}_Y}{K_Y}\right)\psi + i\frac{K_u}{K_Y}\gamma^0\psi + \\ + \frac{i}{2}\left[\frac{F}{F'} - R + 6(2H^2 + \dot{H})\right]\frac{Fh_u}{K_Y}\gamma^0\psi = 0, \end{aligned} \quad (12)$$

where  $H = \frac{\dot{a}}{a}$  Hubble parameter.

Next, we obtain the FRW equations for pressure

$$-(2\dot{H} + 3H^2) = p_f, \quad (13)$$

$$3(1-3\lambda+6\mu)\frac{\dot{a}^2}{a^2}H^2 + 6\mu\dot{H} = R. \quad (14)$$

From the conservation of energy

$$E_L = \frac{\partial L}{\partial \dot{a}}\dot{a} + \frac{\partial L}{\partial \dot{\bar{\psi}}}\dot{\bar{\psi}} + \frac{\partial L}{\partial \dot{\psi}}\dot{\psi} - L = 0, \quad (15)$$

one can obtain the FRW equation for the energy density

$$3H^2 = \rho_f. \quad (16)$$

The expressions for the energy density  $\rho_f$  and the pressure  $p_f$  of the fermion field have the form

$$\begin{aligned} \rho_f &= \frac{1}{1-3\lambda}\frac{F}{F'} - \frac{1}{1-3\lambda}R + \frac{2}{1-3\lambda}\frac{1}{F'}\frac{K}{h} + \\ &+ \frac{6\mu}{1-3\lambda}H\left(\frac{F''}{F'}\dot{R} + \frac{\dot{h}}{h}\right) - \frac{2}{1-3\lambda}\frac{K_Y Y}{hF'}, \end{aligned} \quad (17)$$

$$\begin{aligned} p_f &= -\frac{1}{1-3\lambda}\frac{F}{F'} - \frac{2}{1-3\lambda}\frac{1}{F'}\frac{K}{h} - \frac{2\mu}{1-3\lambda} \times \\ &\times \left(\frac{F'''}{F'}\dot{R}^2 + \frac{F''}{F'}\ddot{R} + 2\frac{\dot{h}}{h}\frac{F''}{F'}\dot{R} + \frac{\ddot{h}}{h}\right) + 2H\left(\frac{F''}{F'}\dot{R} + \frac{\dot{h}}{h}\right). \end{aligned} \quad (18)$$

To solve the system of equations of motion, we first consider equations (11) and (12). We multiply equation (11) by  $\gamma^0 \psi$  and equation (12) by  $\gamma^0 \bar{\psi}$ , then summing these equations, we get the expression:

$$\frac{\dot{u}}{u} = -3H - \frac{\dot{K}}{K_Y}, \quad (19)$$

whose solution has the form

$$u = \frac{u_0}{a^3 K_Y}, \quad (20)$$

where  $u_0$  is the constant of integration. Next, we get differential equality with separated variables, which will be equal to the constant

$$\begin{aligned} & \frac{-2K_Y Y - 2K_u u}{h_u K_u} = \\ & = F' \left( \frac{F}{F'} - R + 3(1 - 3\lambda + 6\mu)H^2 + 6\mu\dot{H} \right) = C. \end{aligned} \quad (21)$$

Consider the  $f$ -essence Lagrangian in the form

$$K = \ln Y + u, \quad (22)$$

substituting into the left-hand side of equation (21), we obtain the connection of matter with space-time as

$$h = \frac{u}{C} + \frac{u^2}{2C} + C_1, \quad (23)$$

then dividing the variables on the right-hand side of the equation, we obtain the equality

$$\begin{aligned} F - RF' - \frac{C}{F'} &= -[3(1 - 3\lambda + 6\mu)H^2 + 6\mu\dot{H}] = \\ &= G = \text{const}, \end{aligned} \quad (24)$$

then the solution

$$H^2 = \frac{e^{-\frac{6(1-3\lambda+4\mu)}{6\mu}(t-t_0)} - G}{3(1-3\lambda+4\mu)}, \quad (25)$$

that is, the Hubble parameter changes exponentially as

$$H \sim e^{-\gamma(t-t_0)}, \quad (26)$$

where  $\gamma = \frac{3(1-3\lambda+4\mu)}{6\mu}$ , hence the scale factor will take the form

$$a = e^{\gamma(t-t_0)}, \quad (27)$$

also, from equation (24), the following dependence can be determined

$$F(R) \sim R + R_0. \quad (28)$$

**Inflation.** Consider an inflationary model with a minimum kinetic term, in which the behavior of the system is described by the FRU and Dirac equations. To describe evolution, it is convenient to introduce the functions of the Hubble flow, which are determined by the formula

$$\varepsilon_{n+1} \equiv -\frac{d \ln |\varepsilon_n|}{dN}, \quad n \geq 0, \quad (29)$$

where  $\varepsilon_0 \equiv H_{ini}/H$  is the slow roll parameter. By definition, inflation is a phase of accelerated expansion  $\ddot{a}/a > 0$  or  $\varepsilon_1 < 1$ , which is the same. The de Sitter quasi solution of inflation evolves with (positive) Hubble flow functions

$$\varepsilon_1 = -\frac{\dot{H}}{H^2}, \quad \varepsilon_2 = -\frac{2\dot{H}}{H^2} + \frac{\ddot{H}}{H\dot{H}} \equiv \frac{\dot{\varepsilon}_1}{H\varepsilon_1}, \quad (30)$$

which should remain small until the end of inflation, when the acceleration ends  $\varepsilon_1 \approx 1$  ( $\dot{H} < 0$ ), therefore, in the model under study, the parameters of the Hubble flow have the same form

$$\varepsilon_1 = \varepsilon_2 = e^{\gamma(t-t_0)}. \quad (31)$$

Also consider the number of  $e$ -folds remaining until the end of inflation

$$N = \ln \left[ \frac{a(t_f)}{a(t)} \right], \quad (32)$$

where  $a(t_i), a(t_f)$  80/5000 are scale factors at the beginning and at the end of inflation, respectively. The total number of inflation is determined as follows

$$N \equiv \ln \left( \frac{a_f(t_f)}{a_i(t_i)} \right) = \int_{t_i}^{t_f} H(t) dt, \quad (33)$$

and in order to have thermalization at the end of inflation, we must require, according to the CMB fluctuation spectrum,  $55 < N < 65$ . Thus, the spectral index  $n_s$  and the tensor-scalar relation  $r$  are derived from the expressions below

$$n_s = 1 - 2\varepsilon_1 - \varepsilon_2, \quad r = 16\varepsilon_1, \quad (34)$$

where  $\varepsilon_{1,2}$  are evaluated to  $N = N$ . The latest cosmological data from the Planck satellite [15] limit these indices as follows:  $n_s = 0.9603 \pm 0.0073(68\%CL)$  and  $r < 0.11(95\%CL)$ .

## Conclusion

This article discusses a complex gravity model within the framework of the Horava-Lifshitz theory for the f-entropy. Studies have shown that when considering the Lagrangian (22) f-essence, the scale factor of this model grows exponentially (27), which indicates an accelerated expansion of the Universe. Compared to de Sitter's standard solution, this gives the universe a much faster acceleration. A linear dependence of the function on the scalar was also found. The results obtained coincide with the data of current observations.

## Acknowledgement

The research work is supported by the grant project AP08052197 (2020-2022) from the Ministry of Science and Education of the Republic of Kazakhstan.

## References

1 Riess, A. G. et al. "Observational Evidence from Supernovae for an Accelerating Universe and a Cosmological Constant." *The Astrophysical Journal* 116, no 3. (1998): 1009-1038.

2 Perlmutter, S. et al. "Measurements of  $\Omega$  and  $\Lambda$  from 42 High-Redshift Supernovae." *The Astrophysical Journal* 517, no. 2. (1999): 565-586.

3 Horava, P. "Quantum gravity at a Lifshitz point." *Physical Review D* Vol.79, no. 8. (2009): 084008.

4 Capozziello, S., Cardone, V.F., and Troisi, A. "Dark energy and dark matter as curvature effects?." *Journal of Cosmology and Astroparticle Physics*, Vol.2006 (2006): 001.

5 Nojiri, S. and Odintsov, S.D. "Modified Gravity with  $\ln R$  Terms and Cosmic Acceleration." *General Relativity and Gravitation* Vol.36 (2004): 1765-1780.

6 Capozziello, S., Cardone V.F., and Troisi A. "Reconciling dark energy models with  $f(R)$  theories." *Physical Review D* Vol.71, no. 4. (2005): 043503.

7 Li, B. and Barrow, J.D. "Cosmology of  $f(R)$  gravity in the metric variational approach." *Physical Review D* Vol.75, no. 8. (2007): 084010.

8 Bean, R., Bernat, D., Pogossian, L., Silvestri, A., and Trodden, M. "Dynamics of linear perturbations in  $f(R)$  gravity." *Physical Review D*, Vol.75, no. 6. (2007): 064020.

9 Navarro, I. and Van Acoleyen, K. " $f(R)$  actions, cosmic acceleration and local tests of gravity." *Journal of Cosmology and Astroparticle Physics*, Vol.2007 (2007): 022.

10 Stelle, K.S. "Classical gravity with higher derivatives." *General Relativity and Gravitation* Vol.9. (1978): 353-371.

11 Sato, K., "First Order Phase Transition of a Vacuum and Expansion of the Universe." *Monthly Notices of the Royal Astronomical Society*, Vol.195 (1981): 467-479.

12 Sato, K., "Cosmological baryon-number domain structure and the first order phase transition of a vacuum." *Physics Letters B* Vol.99, no. 1 (1981): 6670.

13 Guth, A.H., "Inflationary universe: A possible solution to the horizon and flatness problems." *Physical Review D* Vol.23, no. 2. (1981): 347.

14 Ade, P.A.R. et al. "Planck 2013 results. XVI. Cosmological parameters." *Astronomy & Astrophysics* Vol.571 (2014): A16.

15 Komatsu, E. et al. "Five-Year Wilkinson Microwave Anisotropy Probe\* Observations: Cosmological Interpretation". *The Astrophysical Journal Supplement Series* Vol.180, no. 2 (2009): 330-376.

16 Myrzakul Sh., Myrzakulov K., Bekov S., Myrzakul T, Myrzakulov R. Starobinsky model with  $f$ -essence // [arXiv:1710.08413].

17 Jamil, M., Saridakis, E.N., and Setare M.R. "Holographic dark energy with varying gravitational constant." *Physics Letters B* Vol.679, no. 3. (2009): 172-176.

18 Mukohyama, Sh. "Dark matter as integration constant in Horava-Lifshitz gravity." *Physical Review D* Vol.80, no. 6 (2009): 064005.

19 Gorbunov, D.S. and Rubakov, V.A., *Introduction to the Theory of the Early Universe: Hot Big Bang Theory*. World Scientific, 2011.

20 Linde, A.D. "Inflationary Cosmology." *Lecture Notes in Physics* Vol.738 (2008): 1-54.

21 Chaichian M., Nojiri, S., Odintsov, S.D., Oksanen, M., and Tureanu A. "Modified  $F(R)$  Horava-Lifshitz gravity: a way to accelerating FRW cosmology." *Classical and Quantum Gravity* Vol. 27, no. 18 (2010): 185021.

A.S. Kussainov<sup>1\*</sup> , Y.V. White<sup>2,3</sup> , M.A. Em<sup>1</sup> ,  
E.T. Myrzabek<sup>1</sup> , E.T. Salavatova<sup>1</sup> , S.T. Zhaldybayev<sup>1</sup> 

<sup>1</sup>al-Farabi Kazakh National University,  
Almaty, Republic of Kazakhstan

<sup>2</sup>East Georgia State College, Swainsboro, USA

<sup>3</sup>University of Tennessee Space Institute, Tullahoma, USA

\*e-mail: arman.kussainov@gmail.com

## Transition to mammography in the regular computed tomography simulation and reconstruction software

**Abstract.** This paper presents a modification of the previously developed and maintained computed tomography simulation and reconstruction software for the mammography case. New additional modules are designed to process the mammography data. Mammography provides incomplete information about the subject taken from the limited number points of view but as a result has potentially minimized exposure to radiation for the biological tissue under study. We implement this method by providing new standalone independent mammography modules in our software package. These modules are responsible for creating the projections' set according to the operator's input of exposure angles, phantom's structure, and other multiple recording parameters. These additional modules reconstruct the data from these generated sets of projections or take the real medical data as input. Contrast and features' recognition are particularly important elements of the study due to the limited number of projections in set. Our software could be used in combination with any real commercial mammography scanner as well as for research purposes to train medical and physics personnel and study for novel methods of contrast and image enhancement.

**Key words:** Computed tomography, mammography, X-rays, FDK algorithm, backprojection, image reconstruction.

### Introduction

Computed tomography (CT) is essentially a medical diagnostic and screening procedure employing the soft part of the X-ray spectrum generated by a tube operated at about one hundred of kilovolts and less. The known modifications of this modality, suited for different parts of the human body, are projection radiographic imaging and X-ray mammography [1].

Due to an ionizing nature of X-ray radiation mammography is considered as recommended for the "women who place a higher value on the potential benefit than the potential harms" [2]. Screening and diagnostic mammography radiation doses may be as high as 36 mGy per person, see [3], [4], [5]. Thus, a great number of efforts are dedicated to make medical screening procedures safe. Localizing the area of exposure to the organ of interest is a part of these efforts. Human breasts are paired organs and

represent complex body parts rich in blood vessels and connective tissues with distinct particularities depending on the age and health group [6].

The question of good image contrast and resolution is of utmost importance due to the complex nature of the tissue under study. The imaging artifacts come in abundance due to the complexity of the tissue of interest but could be verified by other imaging modalities like magnetic resonance imaging, etc., see [7]. The rich physics of X-ray interaction with breast tissue [8] and imperfections in numerical reconstruction procedures are the other major sources of imaging artefacts. Besides this, the hardware itself, like the ever-increasing size of the flat detectors, causes the multiple artefacts like scatter artefacts in the study of Wei Zhao et al., [9].

The simulations of this particular imaging technique are of big interest and importance [10]. All these studies are strongly dependent on the phantom in use, see [11], [12]. In general, they are roughly

falling into two groups of digital and real physical anthropomorphic phantoms. Real physical phantoms require tedious systematic studies of the tissue's absorption properties complimented by studies of synthetic and biological materials used to mimic these tissues, see [13], [14]. Unique combination of the digital and real physical phantom has been demonstrated using a 3D printer [15]. Nowadays, the 3D printing material could be anything starting from plastic and ending with stem cells.

Ideal CT case assumes that the phantom is recorded from as many angles as possible, so the contrast variation at two adjacent points will be maximized by a contribution from as many projections as possible. The lack of this data, random and systematic variations in recording and

reconstruction conditions, as well as the imperfection of our computer model incapable of grasping the whole multitude of physical phenomena contributing to the case lead to numerous imaging artifacts [16].

Mammography, due to the limited range of exposure angles, needs additional efforts to preprocess and postprocess the images, plus the introduction of several filtering techniques, etc.

## Methods and materials

Mammography modules were built using the framework of the CT project developed in [17]. On the next Figure 1, the map of the project, including all main classes, input and output text, and graphical data are shown.

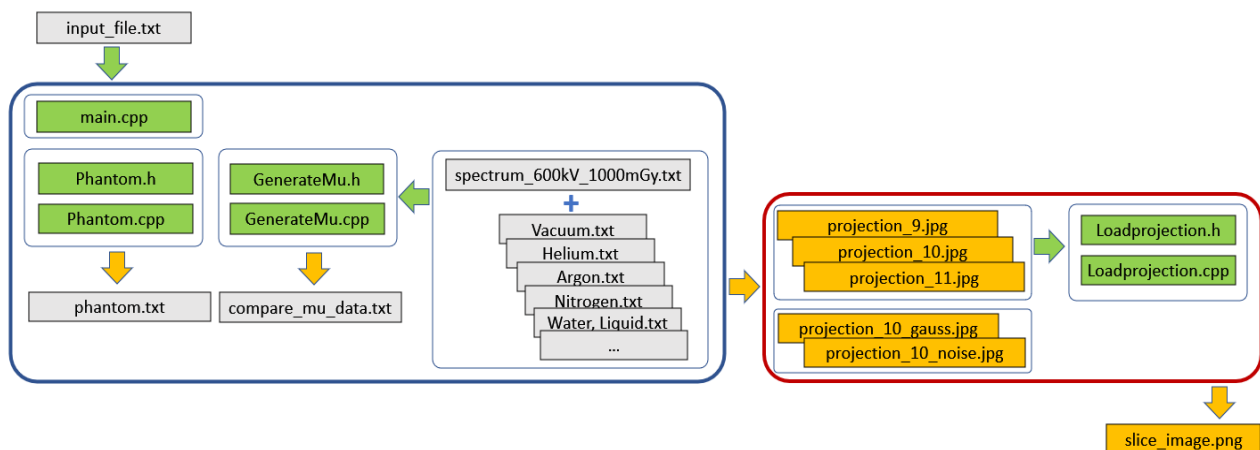


**Figure 1**– The map of the original CT project files and classes (shown as green) including the input files (shown as grey), generated text (shown as grey as well) and image outputs (orange rectangles). The independent X-ray projection generation and CT image reconstruction parts are shown separately, in blue and red rectangle areas correspondingly.

Two, to the great extent independent, modules for producing X-ray projections and reconstructing the CT image from them are shown separately, see enclosing blue and red rectangles.

Original data with information about the project directories and folders, selected recording and reconstruction regime, the elements and compounds used in simulation, the size and orientation of the reconstructed slices and digital phantom, Fourier space filtering techniques for images, the number of projections generated during recording stage and number of them used in reconstruction (not necessarily the same number) and complete description of the digital phantom are given in the input\_file.txt.

The digital phantom is generated by the Phantom.h/Phantom.cpp class according to the input data in input\_file.txt file. For the record and possible future modifications, the replica of the phantom is saved in phantom.txt file.

Another class GenerateMu.h/GenerateMu.cpp is responsible for mapping the data in the original absorption coefficients database files like Vacuum.txt, Helium.txt etc. files onto X-ray source spectrum energy grid given in the spectrum\_600kv\_1000mGy.txt file. As a result of this procedure, we have compare\_mu\_data.txt file containing information about the absorption coefficients for all elements used in this particular digital phantom mapped to the energy grid of the

source X-ray spectrum using the linear interpolation method. This file is also created just for the records and to verify the correctness of information kept in the memory and used for phantom tracing procedure.

The main.cpp part of the project coordinates the work of these two classes and using the object tracing functionality of the class Phantom.h/Phantom.cpp generates a series of X-ray projections projection\_9.png, projection\_10.png etc. shown in orange color on the same figure. The projections could be generated with additional Gauss blur and noise added to simulate the real conditions, see projection\_9\_gauss.png, projection\_10\_noise.png data.

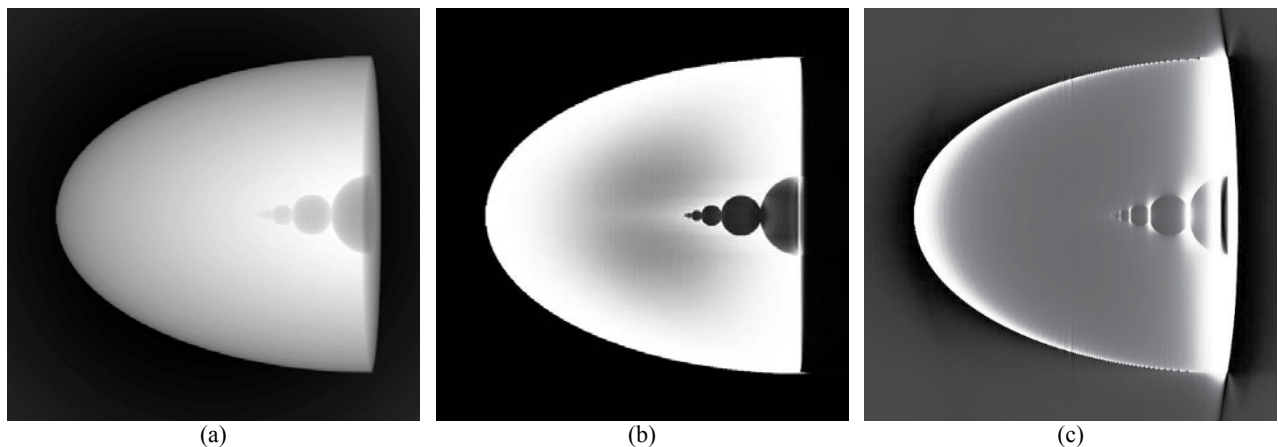
The data generated by this part of the project is used for further reconstruction procedure by Loadprojection.h/Loadprojection.cpp class to produce slice\_image.png CT image.

Figure 2 shows, from top to bottom, the original X-ray projection recorded from our digital phantom at zero rotation angle, the central slice of this

phantom reconstructed by a regular CT backprojection algorithm using our simulation and reconstruction software and the mammography slice taken at the same location using the modified software package. It takes 365 X-ray images to produce a single CT slice image (b) and 179 for the mammography scan slice (c). It takes 150 and 70 seconds to produce images (b) and (c).

The apparent nonuniform intensity distribution across the phantom is inherited by the mammography case and strongly exaggerated by the absence of approximately half of the projected data compared to the regular CT case.

Our digital phantom is constructed as a half of the ellipsoid squeezed along one of the axes to mimic the real mammography recording condition when the human breast is placed between two plates transparent to the X-ray radiation and designed to keep the object immobile. This procedure flattens the breast to some extent, decreasing the effective thickness of the breast tissue.



**Figure 2** – (a) The 1024x1024 pixel image of the X-ray projection taken at 0-degree angle of rotation during a regular CT scan; (b) The 675x675 pixel image of the CT slice reconstructed at the central plane; (c) The 675x675 pixels image of the mammography slice reconstructed at the same plane; Every slice in figures (b) and (c) is produced by summation of 11, one voxel thick, slices grouped around the target cross section at 338 voxel mark.

The ellipsoid is made of adipose tissue which is basically the fat or triglyceride [18]. The interaction with X-ray radiation is described through the regular absorption and dissipation mechanisms coded in our numerical tracing procedure. The absorption and dissipation are quantified in the database of the X-ray mass attenuation coefficients from the “NIST Standard Reference

Database 126” [19]. Compare to the widely used Monte-Carlo methods for simulation [20] of the

particles’ ensemble and the other statistical events with some probability distribution function, this type of simulation [21],[22] is much easier but still produces physically sound results. For the photons’ energy ranged from 1 and up to 2000 KeV, the mass attenuation coefficient  $\mu/\rho$ , where  $\rho=0.95 \text{ g/cm}^3$  is the density of the tissue, takes the values from  $2.628 \times 10^3 \text{ cm}^2/\text{g}$  down to  $1.698 \times 10^3 \text{ cm}^2/\text{g}$ . This absorption properties are mainly defined by the chemical composition of adipose tissue having

hydrogen (H), carbon (C), and oxygen (O) roughly in 1:5:2 ratio.

Figure 3 gives a comparison of the CT and mammography recording geometries. The top part (a) of Figure shows the sketch of the regular CT scan with the digital phantom aimed to resemble a human breast. The source and detector are moving around the phantom to produce multiple X-ray images taken at different angles of rotation. The middle picture,

part (b), shows the same CT geometry but from the top view, along the Z axis and the transformation needed to be taken to perform the mammography scan are shown at the bottom. In part (c), of the Figure 3, we move the detector plane in the immediate vicinity of the phantom and fix it there, which minimizes the movement artefact and radiation dosage to achieve the reasonable contrast and confine the source movement to the half of the ZY plane.

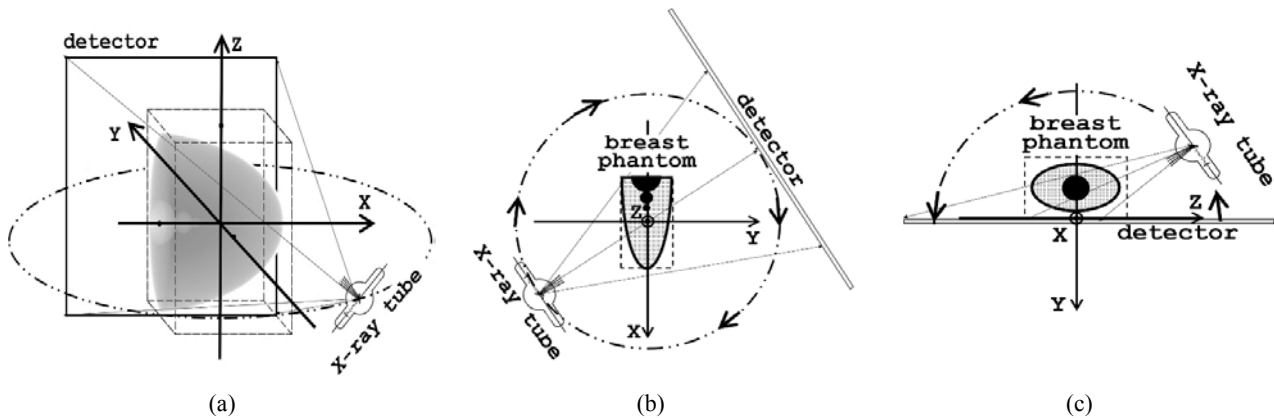


**Figure 3** – From top to bottom: (a) The 3D sketch of the regular CT scan of the phantom under consideration (not to scale); (b) Top view of the same scheme showing the position of the phantom relative to the fixed XYZ coordinate system; (c) The same setup transformed to the mammography case.

The other recording condition assumes that in both cases the exposition camera is filled with dried air. This was taken into account while tracing the X-ray outside the phantom. The principal axes of the ellipsoid are 1024, 512, and 256 voxels and the numerical simulation resolution of 72 voxels per centimeter translates it to 14x7x4 centimeters.

The actual size of the phantom simulation volume, available for filling it with an arbitrary combination of objects of various shapes and materials, is shown by the dashed line parallelepiped sized in 512x256x512 voxels. The size of the ellipsoid that does not fit into this volume is automatically being cut off from simulations. The distance from the center of the phantom to the center detector is 1040 voxels (14 cm) and the distance from the source to the phantom is 2000 voxels (28 cm). The detector's size is assumed to be 1024 by 1024 voxels. The size of the reconstructed slice images, see Figure 2, is controlled by the FOV (Field of View) parameter which is taken to be 675 by 675 voxels.

Besides the regular filtering techniques of the FDK method, there is the slice half thickness parameter, that is, how many 1 voxel thick slices times two plus one are added to one image to increase

SNR (signal to noise) ratio and overall contrast of the images.

Rather than building a complete numerical ductal network in the digital breast phantom [23], we wanted to qualitatively describe the methods' resolution, and so the phantom was filled with empty spheres of gradually decreasing size placed along the biggest axis of the ellipsoid. The diameters of the spheres are 128, 64, 32, 16, 8, and 4 voxels correspondingly, which makes them 1.78, 0.89, 0.44, 0.22, 0.11 and 0.06 cm small. Similar periodic structures of variable size to test resolution were used in [24]. In all cases, the central slice in ZX plane was reconstructed as an obvious choice to maximize the contrast and uniformity of illumination conditions.

The closer look at Figures 3 (b) and (c) tells us that the mathematical description of the backprojection algorithm stays precisely the same for the mammography case as long as we preserve the direct mapping from the projections onto the plane of the reconstructed slice. The addition of the imaginary plane to Figure 3 (c) placed perpendicular to the source's beam and following the source from left to the right in a circular path, staying behind the phantom makes this statement clear.

The X-ray spectrum was taken for the G-297 rotating anode X-Ray tube from the Varex Imaging data specification for 100 KeV with a maximum peak fluence of  $1.57 \times 10^7$  photons per  $\text{mm}^2$  at 8.5 KeV, see Figure 4.

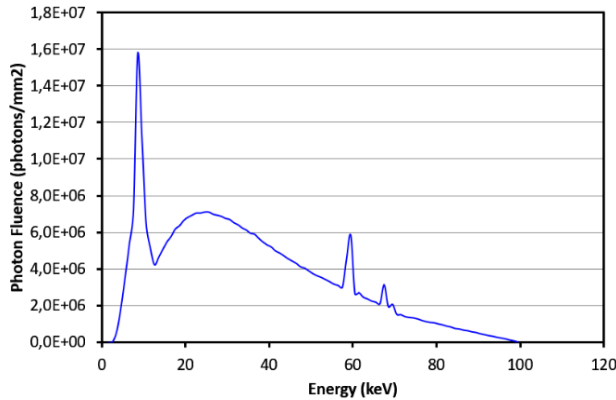


**Figure 4** – TASMICS [26] (tungsten anode spectral model using interpolating cubic splines) spectrum at specified air kerma

Total fluence is summed up to  $3.61 \times 10^8$  photons per  $\text{mm}^2$  and the average energy is 35 keV. HVL (Half Value Layer) for Al and Cu are 0.0634 and 0.0089 mm correspondingly. Specific air kerma was set for 100 mGy. This particular X-ray spectrum was used for numerical simulations of the phantoms described previously in the text.

The universal reconstruction method described by the well-known FDK algorithm named after Feldkamp, Davis, and Kress, see [25]. For finite number of projections, FDK algorithm could be described as a summation of the previously recorded projections back on the plane of interest, see next equation (1)

$$f(x, y) = \Delta B \sum_{i=1}^M \frac{1}{U^2(x, y, \beta_i)} \tilde{Q}_{\beta_i}, \quad (1)$$

where  $\tilde{Q}_{\beta_i}$  stands for projection selected from the series of the recorded ones and selected for backprojection,  $\beta_i$  is the rotation angle for the source-detector couple for this particular projection and  $\Delta B = 2\pi/M$ , where  $M$  is the total number of projections, in general recorded from 0 to  $2\pi$  value of  $\beta_i$ . Normalization factor  $U^2(x, y, \beta_i)$  have somewhat complex structure depending on the geometry of the source beam, its trajectory and other factors and has explicit dependence on  $x$  and  $y$ , in case of a simple

parallel beam geometry. In simple cases it is just a scaling factor. Tilda sign, which is used in  $\tilde{Q}_{\beta_i}$  projection's notation, expresses the fact that the original projection has been filtered in Fourier space by  $H(w)$  filter, see the next expression

$$H(w) = |w|b_w(w) \quad (2)$$

and  $b_w(w) = \begin{cases} 1, & |w| < W \\ 0, & |w| \geq W \end{cases}$

This partially solves the reconstructed image smearing caused by the presence of the projections' data in the areas otherwise containing no real image. The  $W$  value measures the size of the frequencies' window in Fourier space. The value of  $\tau$  is the sampling rate for the digital image of the projection and directly relates to the size of its pixels.

With the ability to reconstruct cross-section images from the sequence of real data taken from medical or experimental CT scanners, our software is now capable to produce the full-scale CT and mammography simulation of different digital phantoms of high resolution and complex, user-defined structures. The 8-core Intel Core i7-4790K desktop computer with 32 Gb RAM was used for simulations.

### Results and discussion

The input\_file.txt, if modified to work in the mammography case, requires a couple of yes flags on lines 4 and 5 to set the mammography case and specify that the generated projection will be stored locally on the hard drive and to the directory specified by the path on line 3. The value of source.to.phantom:2000 still needs to be defined explicitly on line 10, although the value of phantom.to.detector is irrelevant now and filled with arbitrary digits, because it will be recalculated in the code to move the object close to the detector:

```

1 path.mu.data:Attenuation coefficients\\NIST
  compounds\\
2 path.spectrum.data:100kV.txt
3 path.projection.data:C:\\CT_project\\mammography\\
4 mammography.yes
5 projections.yes
6 element.id:Vacuum.0
7 element.id:Air, Dry.1
8 element.id:Water, Liquid.2
9 element.id:Adipose Tissue.3
10 source.to.phantom:2000
11 source.elevation:0
12 phantom.to.detector:99999999
    
```

```

13 field.of.view:512
14 slice.plane:XY
15 target.cross.section:320
16 slice.half.thickness:0
17 zero.padding.factor:0
18 cut.background:0.0
19 tukey.window.alpha:0.0
20 detector.width:1024
21 detector.height:1024
22 start.angle:-89 // from a lesser number to bigger one
23 end.angle:89
24 projections.number:179
25 image.compression:9

```

The lines 13 through 19 define the orientation, size and graphics properties of the reconstructed mammography slice. Lines 20 through 25 give the size of the detected X-ray projection, and the start and end angle for the total number of 181 projections taken with 1 degree step.

The parsing of the input\_file.txt takes place in the main.cpp block, thus, historically, the loop initiating the recording of consecutive projections, that is the rotation of the source/ detector pair also resides in main.cpp. In order to initiate the recording of the sequence of mammographic projections, we need to go through the following steps:

```

1 float t_before = 0, t_after = 1.0;
2 int m_amo = 0;
3 //Phantom tracing and creating the projections
4 for(float d_egree=start_angle; d_egree<=end_angle;d_egree+=degree_step){
5     if (mammography_yes==0){
6         int shift_degree=int(d_egree)%90;
7         t_before=(float(source_to_phantom)-(float)sin((45.0f+shift_degree)/180.0f*pi)
8             *float(max_dim)/1.4142f)
9             /float(source_to_phantom+phantom_to_detector);
10        t_after=(float(source_to_phantom)+(float)sin((45.0f+shift_degree)/180.0f*pi)
11            *float(max_dim)/1.4142f)
12            /float(source_to_phantom+phantom_to_detector);
13        p_hantom.create_projection(-source_to_phantom,source_elevation,
14            phantom_to_detector,d_egree,detector_width,
15            detector_height,interpolated_mu_data,
16            muvalues.s_pectrum,interpolation_points,
17            elements_count,muvalues.total_hw,
18            image_compression,voxels_per_cm,t_before,t_after,
19            m_amo, projections_dir);
20    }
21    else{
22        m_amo = 1;
23        phantom_to_detector=static_cast<int>(depth/2.0f)+1;
24        cout << "\n\nThe phantom.to.detector value is set to 1/2 (half) of the
25        phantom.depth and equals to " << phantom_to_detector << "\n\n";
26        float source_to_detector_center=static_cast<float>(source_to_phantom
27            +phantom_to_detector);
28        int sourcetophantom=static_cast<int>(source_to_detector_center
29            *cos(d_egree*pi/180.0f))-phantom_to_detector;
30        int sourceelevation=static_cast<int>(source_to_detector_center
31            *sin(d_egree*pi / 180.0f));
32        t_before=(float(sourcetophantom)-float(depth)/2.0f)
33            /float(sourcetophantom+phantom_to_detector);
34        t_after=(float(sourcetophantom)+float(depth)/2.0f)
35            /float(sourcetophantom+phantom_to_detector);
36        p_hantom.create_projection(-sourcetophantom,sourceelevation,
37            phantom_to_detector, d_egree,detector_width,
38            detector_height,interpolated_mu_data,
39            muvalues.s_pectrum,interpolation_points,
40            elements_count,muvalues.total_hw,
41            image_compression,voxels_per_cm,t_before, t_after,
42            m_amo, projections_dir);
43        if ((end_angle==start_angle)(projections_number==1)){break;}
44    }
45 }

```

To compare to different recording strategies, CT and mammography, one should take a look, side by side, at lines 2-19 and 22-43.

Backprojecting part of the code is introduced into the Loadprojection.h/Loadprojection.cpp class. The snippet of the C/C++ code with the Open MP parallelization directives implemented by Microsoft in Visual Studio 2015 is listed below. As usual, the names of the variables have one to one correspondence with the physical parameters of the real setup.

The first piece of code is given for the ZX orientation of the reconstructed slice. The choice of data acquisition scheme “mammo” and target plane orientation, that is along “ZX” plane, are made at the first line. The next lines 2 through 6 move the

detector close to the phantom and define the trajectory of the source. Nested loops on lines 7, 10, and 14 define the location of the reconstructed slice in the fixed (Xt,Yt,Zt) laboratory frame of reference. The ci and ck variables defined on lines 12 and 16 refer to the coordinate system of the detector and map the data from projections taken from the phantom at different angles, back to the reconstructed slice (Xt,Yt,Zt). Multiple cores and threads supported in contemporary computers increase performance of the code by running OpenMP directives on line 9. The maximum performance is achieved by using this pragma only with one nested loop over Xt. Variable c\_onvolved refers to the projected data convolved with the high pass filter in Fourier space.

```

1  if((mammo == 1) && (a_ffix == "ZX")) {
2  float source_to_detector_center = static_cast<float>(-y_source + y_detector);
3  float sourcetophantom = source_to_detector_center*c_os
4  -static_cast<float>(y_detector);
5  float sourceelevation = source_to_detector_center*(-s_in);
6  float source_to_detector = source_to_detector_center*cos(view_angle);
7  for (int Yt = t_arget - d_elta; Yt <= t_arget + d_elta; Yt++) {
8  float Yp = static_cast<float>(Yt) - half_slice;
9  #pragma omp parallel for
10 for (int Xt = 0; Xt < slice_size; Xt++) {
11 float Xp = static_cast<float>(Xt) - half_slice;
12 int ci = static_cast<int>(Xp*source_to_detector / (sourcetophantom + Yp)
13 + static_cast<float>(w_detector) / 2.0);
14 for (int Zt = 0; Zt < slice_size; Zt++) {
15 float Zp = static_cast<float>(Zt) - half_slice;
16 int ck = static_cast<int>(sourceelevation - (sourceelevation - Zp)
17 *source_to_detector/(sourcetophantom + Yp)
18 +static_cast<float>(h_detector) / 2.0);
19 if ((ck >= 0) && (ck < h_detector) && (ci >= 0) && (ci < w_detector)) {
20 slice.at<float>(Zt,Xt)+=
21 c_onvolved.at<float>(h_detector - 1 - ck, w_detector - 1 - ci);
22 }
23 }
24 }
25 }
26 }
```

The float  $c_{os} = \cos(-view\_angle)$ ; and float  $s_{in} = \sin(-view\_angle)$ ; variables are introduced out of the multiple nested loops to speedup the calculations and to be calculated only once per rotation angle.

There are two other similar blocks responsible for reconstruction in XY and YZ planes correspondingly. To clarify the overall backprojecting geometry, they are listed below as well. See the next insert for the XY plane:

```

27 if((mammo == 1) && (a_ffix == "XY")) {
28 float source_to_detector_center = static_cast<float>(-y_source + y_detector);
29 float sourcetophantom = source_to_detector_center*c_os
30 -static_cast<float>(y_detector);
31 float sourceelevation = source_to_detector_center*(-s_in);
32 float source_to_detector = source_to_detector_center*cos(view_angle);
33 for (int Zt = t_arget - d_elta; Zt <= t_arget + d_elta; Zt++) {
```

```

34     float Zp = static_cast<float>(Zt - half_slice);
35     #pragma omp parallel for
36     for (int Xt = 0; Xt < slice_size; Xt++) {
37         float Xp = static_cast<float>(Xt) - half_slice;
38         for (int Yt = 0; Yt < slice_size; Yt++) {
39             float Yp = static_cast<float>(Yt) - half_slice;
40             int ci = static_cast<int>(Xp*source_to_detector / (sourcetophantom + Yp)
41                 + static_cast<float>(w_detector) / 2.0);
42             int ck = static_cast<int>(sourceelevation - (sourceelevation - Zp)
43                 * source_to_detector / (sourcetophantom + Yp)
44                 + static_cast<float>(h_detector) / 2.0);
45             if ((ck >= 0) && (ck < h_detector) && (ci >= 0) && (ci < w_detector)) {
46                 slice.at<float>(Xt, Yt) +=
47                 c_onvolved.at<float>(h_detector - 1 - ck, w_detector - 1 - ci);
48             }
49         }
50     }
51 }
52 // for XY slice the modified factor U2 could be taken out of all loops
53 slice = slice.mul(U2);
54 }

```

and for the YZ plane:

```

55     if ((mammo == 1) && (a_fix == "ZX")) {
56         float source_to_detector_center = static_cast<float>(-y_source + y_detector);
57         float sourcetophantom = source_to_detector_center*c_os
58             -static_cast<float>(y_detector);
59         float sourceelevation = source_to_detector_center*(-s_in);
60         float source_to_detector = source_to_detector_center*cos(view_angle);
61         for (int Xt = t_target - d_elta; Xt <= t_target + d_elta; Xt++) {
62             float Xp = static_cast<float>(Xt) - half_slice;
63             #pragma omp parallel for
64             for (int Yt = 0; Yt < slice_size; Yt++) {
65                 float Yp = static_cast<float>(Yt) - half_slice;
66                 int ci = static_cast<int>(Xp*source_to_detector / (sourcetophantom + Yp)
67                     + static_cast<float>(w_detector) / 2.0);
68                 for (int Zt = 0; Zt < slice_size; Zt++) {
69                     float Zp = static_cast<float>(Zt) - half_slice;
70                     int ck = static_cast<int>(sourceelevation - (sourceelevation - Zp)
71                         * source_to_detector / (sourcetophantom + Yp)
72                         + static_cast<float>(h_detector) / 2.0);
73                     if ((ck >= 0) && (ck < h_detector) && (ci >= 0) && (ci < w_detector)) {
74                         slice.at<float>(Zt, Yt) +=
75                         c_onvolved.at<float>(h_detector - 1 - ck, w_detector - 1 - ci);
76                     }
77                 }
78             }
79         }
80     }

```

The definition of the recording geometry variables takes place in all pieces of the code in the first five lines. The OpenMP `#pragma omp parallel for` directive is placed above the first loop over the current active plane. The rest of the code is about casting, backprojecting the scaled image from projections, onto the plane of interest, that is, the mammography image reconstruction plane. The image is scaled because the point-like X-ray source produces a divergent beam, expanding as it passes the

space between the source and the detector, otherwise there will be no scaling at all.

The sample mammography data for multiple slices in YZ plane are shown on the next Figure 5. One can see that the general shape and location of the main features of the phantom are preserved but represent the somewhat severe quality degradation. Additional filtering and tomosynthesis techniques are required to fully recover the data. As expected, the data on each

part of Figure 5 was undersampled due to the physical inability of the system to record the projections behind the detector when the phantom was placed before it. The structures that lay close

enough to the detector are still satisfactory resolved. A type of ghosting artefact is visible on the last part (d) of the Figure 5 for the part of the phantom far away from the central plane.

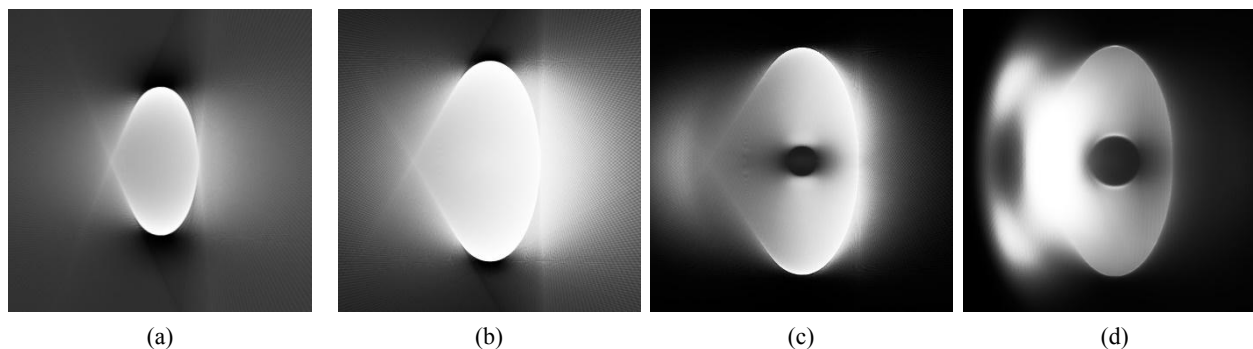


**Figure 5** – Multiple slices taken in mammography mode from a digital breast phantom.

Locations of the slices are at the 200, 338, 500, and 560 voxel mark. FOV size is 675 by 675 voxels.

Number of projections used in the reconstruction are 179 evenly spaced in one degree step from -89 to +89 angle values if counted from the negative direction of the Y axis. Reconstruction of each slice takes about 60-70 seconds.

## Conclusions

New additional modules transforming our computed tomography software package into fully functional mammography mode have been implemented. The reasonable quality data have been generated, although requiring further work on the contrast enhancement and artifact removal. The basic image processing has been done using the OpenCV image processing libraries compiled with the MS Visual Studio IDE compiler. The 3D reconstruction and data visualization from the set of backprojected slices are produced in Matlab. The software package could be used in combination with any real commercial mammography scanner, for the research purposes and to train medical and physics personnel.

The project is available for download at Github repository.

## Acknowledgements

This part of the research was supported by the Physics and Technology Department as well as by the National Nanotechnology Lab of Open Type at al-Farabi Kazakh National University, Almaty, Republic of Kazakhstan. Originally, the work on the project was started at Adani medical equipment production plant.

## References

- 1 Bushberg, Jerrold T., J. Anthony Seibert, Edwin M. Leidholdt and John M. Boone. *The essential physics of medical imaging*. Third Edition. Philadelphia: Lippincott, Williams & Wilkins, 2011.
- 2 United States Preventive Services Taskforce recommendation on breast cancer screening, at web-address: <https://www.uspreventiveservicestaskforce.org/uspstf/recommendation/breast-cancer-screening>, (accessed on February 10, 2021).
- 3 O'Connell, Avice M, and Daniel Kawakyu-O'Connor. "Dedicated Cone-beam Breast Computed Tomography and Diagnostic Mammography: Comparison of Radiation Dose, Patient Comfort, And Qualitative Review of Imaging Findings in BI-RADS 4 and 5." *Journal of Clinical Imaging Science* 2, no.1(2012):1-8.
- 4 He, Ni et al. "The utility of breast cone-beam computed tomography, ultrasound, and digital mammography for detecting malignant breast tumors: a prospective study with 212 patients." *European Journal of Radiology* 85, no.2 (2016): 392–403.
- 5 Hammerstein, Richard G. et al. "Absorbed radiation dose in mammography." *Radiology* 130, no.2 (1979): 485-91.

- 6 Wang, Tonghe et al. "Dosimetric study on learning-based cone-beam CT correction in adaptive radiation therapy." *Medical Dosimetry* 44, no.4 (2019): e71-e79.
- 7 Anthony, Marina-Portia et al. "Artifacts in Breast Magnetic Resonance Imaging." *Current Problems in Diagnostic Radiology* 45, no.4 (2015): 271-77.
- 8 Wienbeck, Susanne et al. "Artifacts Caused by Breast Tissue Markers in a Dedicated Cone-beam Breast CT in Comparison to Full-field Digital Mammography." *Academic Radiology* 24, no.7 (2016): 908-15.
- 9 Zhao, Wei et al. "A model-based scatter artifacts correction for cone beam CT." *Medical Physics* 43, no.4 (2016): 1736-53.
- 10 Walz-Flannigan, Alisa et al. "Artifacts in Digital Radiography." *American Journal of Roentgenology* 198, no.1 (2012): 156-61.
- 11 di Franco, Francesco et al. "GEANT4 Monte Carlo simulations for virtual clinical trials in breast X-ray imaging: Proof of concept." *Physica Medica* 74 (2020): 133-42.
- 12 Bliznakova, Kristina. "The advent of anthropomorphic three-dimensional breast phantoms for X-ray imaging." *Physica Medica* 79 (2020): 145-61.
- 13 McGarry, Conor K et al. "Tissue mimicking materials for imaging and therapy phantoms." *Physics in Medicine & Biology* 65 (2020): 23TR01.
- 14 Sechopoulos, Ioannis et al. "Characterization of the homogeneous tissue mixture approximation in breast imaging dosimetry." *Medical Physics* 39, no.8 (2012): 5050-9.
- 15 Glick, Stephen J, and Lynda C Ikejimba. "Advances in digital and physical anthropomorphic breast phantoms for x-ray imaging." *Medical Physics* 45, no.10 (2018): e870-e885.
- 16 Malliori, Anthi et al. "Development of Physical Breast Phantoms for X-ray Imaging Employing 3D Printing Techniques." *The Open Medical Imaging Journal* 12, no.1 (2020): 1-10.
- 17 Kussainov, Arman and Nurzhan Saduev. "Homemade computed tomography setup with FDK reconstruction software." *Journal of Physics: Conference Series* 1391 (2019): P.012086.
- 18 Nelson, David L., Michael M. Cox. *Lehninger Principles of Biochemistry*. Eight Edition. New York: Worth Publishing, 2021.
- 19 Seltzer, Stephen M. "Calculation of Photon Mass Energy-Transfer and Mass Energy-Absorption Coefficients." *Radiation Research* 136, no.2 (1993): 147-70.
- 20 Sarno, Antonio et al. "Homogeneous vs. patient specific breast models for Monte Carlo evaluation of mean glandular dose in mammography." *Physica Medica* 51 (2018): 56-63.
- 21 Mettievier, Giovanni et al. "Evaluation of the Breast Simulator software platform for breast tomography." *Physics in Medicine & Biology* 62, no.16 (2017): 6446-66.
- 22 Dance, David et al. "Breast dosimetry using high-resolution voxel phantoms." *Radiation Protection Dosimetry* 144, no.1-3 (2005):359-63.
- 23 Bakic, Predrag R et al. "Maidment Mammogram synthesis using a three-dimensional simulation. III. Modeling and evaluation of the breast ductal." *Medical Physics* 30, no.7 (2003): 1914-25.
- 24 Sarno, Antonio et al. "Imaging performance of phase-contrast breast computed tomography synchrotron radiation and a CdTe photon-counting detector." *Physics in Medicine & Biology* 32, no.5 (2016): 681-90.
- 25 Kak, Avinash C., Malcolm Slaney, *Principles of Computerized Tomographic Imaging*. New York: IEEE Press, 1999.
- 26 Punnoose, Jacob et al. "Technical Note: spektr 3.0-A computational tool for x-ray spectrum modeling and analysis." *Medical Physics* 43, no.8 (2016): 4711-17.

A.I. Kupchishin<sup>1</sup> , V.M. Lisitsyn<sup>2</sup> , M.N. Niyazov<sup>1</sup> , D.S. Utepova<sup>1\*</sup> 

<sup>1</sup>Abai Kazakh National Pedagogical University, Almaty, Kazakhstan

<sup>2</sup>Tomsk Polytechnic University, Tomsk, Russia

\*e-mail: utepova\_daniya@mail.ru

## Study of the mechanical properties of industrial plexiglas testing for flat straight bending

**Abstract.** The mechanical properties of industrial plexiglas (polymethylmethacrylate) of various sizes (lengths, widths) have been studied when tested for plane straight bending with one concentrated force in the middle of the sample. By a result of the experimental work, the relationship between deformation and stress was obtained. It is clearly shown in the work that the experimental curves substantially depend on the parameters of the starting materials and are satisfactorily described by a linear model. The slope of tangent ( $\alpha$ ) for the curves ranges from 0,32 to 0,62 %MPa<sup>-1</sup>. The dependence of  $\alpha$  on the length and width of the samples changes significantly. Moreover, the maximum deformation varies in the range of 50 – 60 %, which confirms the dependence of the deformation properties of the material on horizontal components, in particular, on the length of the sample. The tensile strength of the material also differs between specimens of different sizes.

**Key words:** plexiglas, stress, deformation, mechanical properties, bending, elongation, strength.

### Introduction

Polymer composite materials through to their unique mechanical properties are widely applied in various fields of industries and have a broad range of applications, particularly in every day life, construction, automotive and aerospace [1]. For example, the manufacture of parts using composite materials makes a significant contribution to reducing the weight of the final product, which undoubtedly affects its demand in the market. There is considerable of interest on the part of industrial industry and science lately in the research of composite materials for this reason. In tis important role played by the quality of the solids, of which products are manufactured. Before improving its parameters and becoming more attractive in today's competitive market, a significant number of companies conduct mechanical tests of materials to reveal their properties, as well as obtain new materials by mixing different components [2]. It is possible the find the interval of their use and prevent possible damage during use by examining the various characteristics of the products [3]. To study the mechanical properties of polymer composites are sundry kind of tests, including durability, tensile, compressive, tensile strength, elasticity, proportion-

nality, impact strength and elongation after fracture and etc. [4]. Among these influences, the flexural test method has some advantages, such as easy sample preparation (fabrication) and no gripping, compared to tensile testing. The most common of these is straight bend. Straight bending is a traditional test method, which is conducted with the shear effects and local deformation when applied on supports of the load. The bending test is based on the application of a bending force to the test materials [5]. Test calculates the tensile strength at maximum bending load. There are different methods of bending test materials, such as methods of a concentrated force that was set in the middle of the sample between the supports and the two forces applied parallel on supports. The method of loading a test specimen with a solid force applied uniformly along the specimen between the supports and forces, and other methods. The single concentrated force method is the simplest and most affordable method for testing. In addition, to a certain extent, the results depend on the shape loading conditions and dimensions of the samples. In this work, we investigated the dependence of the deformation on the stress of industrial plexiglas when tested for flat straight bending by a focused one force [6].

## Research methods

Industrial plexiglas was taken as the test material. The samples had thickness of 1 mm, respectively, a width of 10 mm and 5 mm and were cut to different working lengths. The thickness of the polymethyl methacrylate samples was measured along the entire perimeter with a micrometer. The depending on the size made by a special cutting device which can be adjusted both the width and length of the sample material. The final touch in preparing a sample for testing is its grinding and polishing, which are designed to eliminate irregularities and burrs that appear as a result of cutting [7].

Figure 1 illustrates a block diagram of the experimental setup that was used to investigate the

stress-strain relationship. The setup consists of the following parts: a force sensor (built-in voltage cap), strain sensor, the device for holding a sample (right and left supports, as well as cantilever clamps), an interface to output data. The components listed above are located on lower part of the BI – 50 machine, equipped with a mobile mechanism [8].

All experimental studies were carried out on attest setup providing a constant loading speed of 10 mm/min. the movement took place relative to the tip and supports, where the deflection was measured with an error of  $\pm 5\%$  and the load was  $\pm 3\%$ . The convergence of the tip and supports held at a uniform speed. Plexiglas samples were loaded in the center of the sample with one concentrated force between the supports [9].

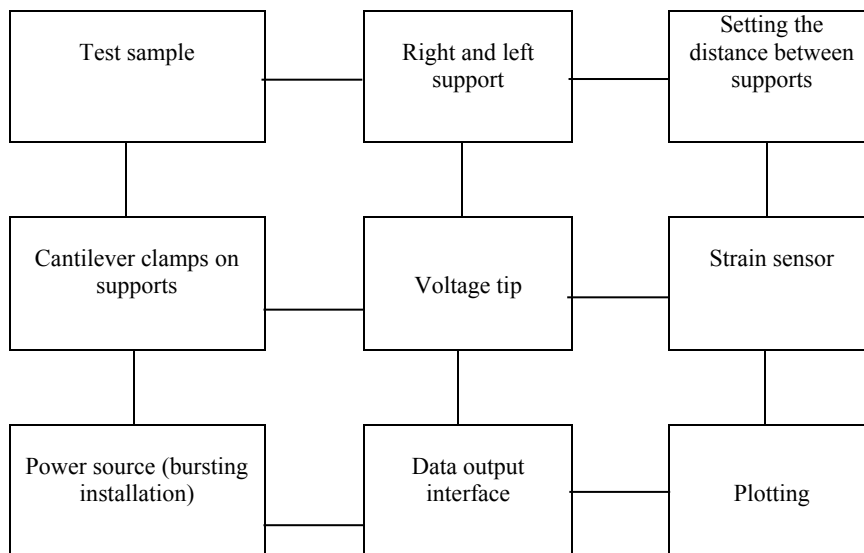


Figure 1 – Installation block diagram

The calculation of the dependence of  $\varepsilon_f$  on  $\sigma_f$  from the experimental data was performed by the following procedure. The flexural stress ( $\sigma_f$ ) at bending  $z$  is calculated by the formula below [10]. The stress ( $\sigma_f$ ) takes into account the contribution of the horizontal component of the bending moment,

$$\sigma_f = \frac{3FL}{2bh^2} \left( 1 + \frac{4z^2}{L^2} \right), \quad (1)$$

where  $b$  – width of the specimen (mm),  $L$  – working length, the distance between two support point

(mm),  $h$  – thickness of the specimen (mm),  $z$  represents the deflection of the material in the middle.

Elongation was calculated as the ratio of the deflection to the working length of the sample ( $\varepsilon = z/L$ ). Taking into account all values, we have [10]:

$$\varepsilon_f = \frac{1}{2} \sqrt{\frac{2\sigma_f b h^2}{3FL} - 1} \quad (2)$$

where  $F$  is bending force (N),  $b$  and  $h$  are sample's dimensions.

## Results and discussion

As a result of experimental studies on testing samples of industrial plexiglass of various sizes for flat straight bending, the dependences of deformation or strain on stress were obtained, which are shown in Figures 2 – 5. The figures mark the results of the experiment, and the lines mark the calculation data. The presentation of the physical and mechanical properties was carried out in the coordinates  $\varepsilon$ ,  $\sigma$ . The relationship between stress  $\sigma$  and strain  $\varepsilon$  has no physical meaning, here stress  $\sigma$  is an argument and strain  $\varepsilon$  represents a function. It can be seen from the figures that the dependence of stress on deformation is satisfactorily described by a linear model for all sizes:

$$\varepsilon = \alpha \sigma, \quad (3)$$

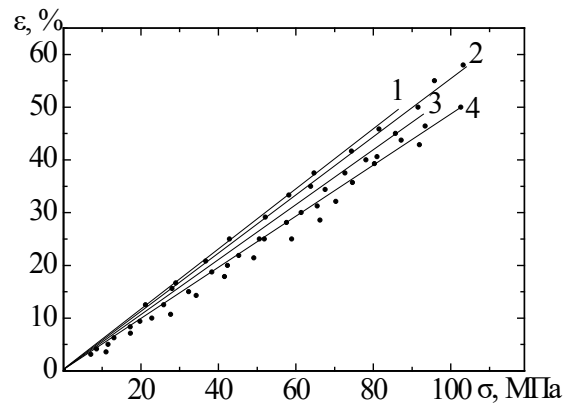
where  $\varepsilon$  is deformation (%),  $\sigma$  is stress (MPa),  $\alpha$  is the slope tangent of angle.

Figures 2 – 5 show the slope of tangent for the curves, which ranges from 0.32 to 0.62% \* MPa<sup>-1</sup>.

The dependence of  $\alpha$  on the length and width of the samples is shown in Table 1. It can be seen that with increasing length, the tangent of the angle increases for samples 10 mm wide. However, at a specimen length is 5 mm, a stepwise increase occurs, i.e. strain  $\alpha$  increases from 0.33 to 0.45% \* MPa<sup>-1</sup>, and then drops again to 0.32% \* MPa<sup>-1</sup> and starts to increase again. From which it can be concluded that a decrease in the width of the samples affects the regularity and applicability of the linear model. A possible reason is that, due to its base in the form of acrylic resins, plexiglas is capable of producing microcracks, which at that time affect the uniform distribution of force over the entire area of the specimen. It is logical that cutting samples contributes to the appearance of microcracks, especially in cases of small sizes. Moreover, the maximum deformation varies in the range of 50 – 60%, which confirms the dependence of the deformation properties of the material on its horizontal components, in particular, on the length of the sample. The tensile strength of the material also differs between specimens of different sizes.

**Table 1** – Dependence the tangent of the angle of slope on the length and width of the sample

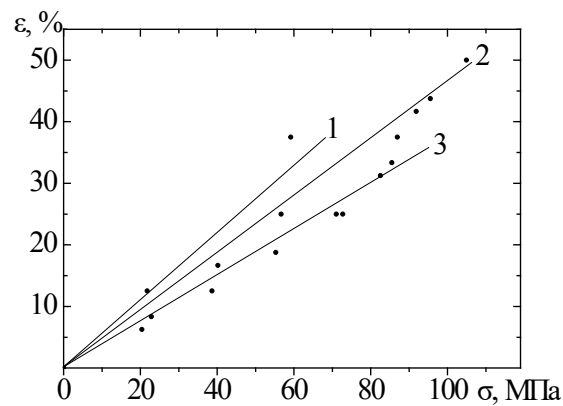
Width, mm	Length, mm	Tangent of the angle, %*MPa <sup>-1</sup>
5	20	0,33
5	30	0,41
5	40	0,45
5	50	0,32
5	60	0,35
5	70	0,40
5	80	0,46
10	20	0,37
10	30	0,41
10	40	0,48
10	50	0,50
10	60	0,55
10	70	0,57
10	80	0,62



1 – 80; 2 – 70; 3 – 60; 4 – 50 mm

*Calculation is represented by lines, experiment by figures;*

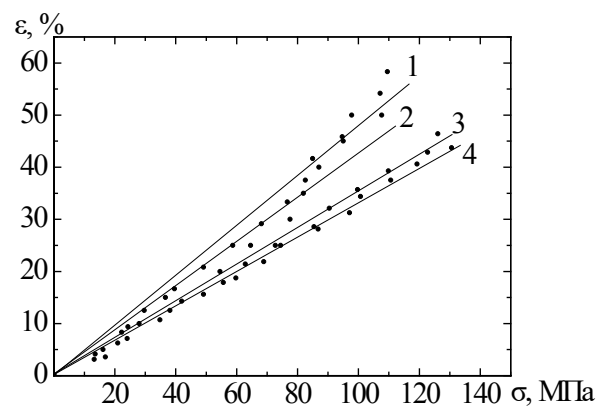
**Figure 2** – Represents the relationship between deformation and stress of an industrial plexiglas sample of various lengths and 10 mm width



1 – 40; 2 – 30; 3 – 20 mm

*Calculation is represented by lines, experiment by figures;*

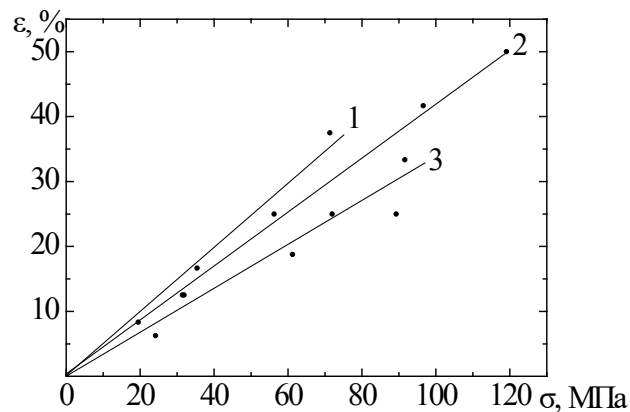
**Figure 3** – Represents the relationship between deformation and stress of an industrial plexiglas sample of various lengths and 10 mm width



1 – 80; 2 – 70; 3 – 60; 4 – 50 mm

*Calculation is represented by lines, experiment by figures;*

**Figure 4** – Represents the relationship between deformation and stress of an industrial plexiglas sample of various lengths and 5 mm width



1 – 40; 2 – 30; 3 – 20 mm

Calculation is represented by lines, experiment by figures;

**Figure 5** – Represents the relationship between deformation and stress of an industrial plexiglas sample of various lengths and 5 mm width

## Conclusions

In the experimental work when tested on a flat straight bending ratio was found between strain and stress for industrial Plexiglas sample. It was found that the maximum deformation of materials of various sizes varies in the range of 50 – 60 %, which confirms the dependence of the deformation properties of the material on horizontal components, in particular the length of the sample.

The curves obtained after the calculation describing the relationship between elongation ( $\varepsilon_f$ ) and flexural stress ( $\sigma_f$ ) are satisfactorily described by a linear model.

## References

- 1 Gunay A., Fank S., Gulmez T., Durakbasa N.M. "Calculation of measurement uncertainty for plastic (ABS) material in flexural testing." *International Journal of Metrology and Quality Engineering*, Vol.4, Issue 1 (2013): 29.
- 2 Strobl G., Berlin: Springer-Verlag Berlin Heidelberg (2007)
- 3 Batu T., Lemu H. G. "Investigation of mechanical properties of false banan/glass fiber reinforced hybrid composite materials." *Results in Materials*, Vol. 8(2020).
- 4 Scutaru, M. L., Itu, C., Marin, M., Grif, H.-Ștefan. "Bending tests used to determine the mechanical properties of the components of a composite sandwich used in civil engineering." *Procedia Manufacturing*, Vol. 32 (2019): 259.
- 5 Al-Mosawi A. I., Ammash H.K. and Salaman A.J. *Properties of Composite Materials Databook*, Germany: Lambert Academic Publishing LAP, 2012.
- 6 Miller, Tara, ed. *Introduction to Composites*, 4th Edition. New York: Composites Institute, Society of the Plastics Industry, 1998.
- 7 Kollar, L.P., Springer, G.S., *Mechanics of Composite Structures*. Cambridge: Cambridge U.P., 2003.
- 8 Cihan M. Sobey A., Blake J. "Mechanical and dynamic performance of woven flax/E-glass hybrid composites." *Composites Science and Technology*, Vol. 172 (2019): 36.
- 9 Abd El-baky M., Attia M., Abdelhaleem M., Hassan M. "Mechanical characterization of hybrid composites based on flax, basalt and glass fibers." *Journal of Composite Materials*, Vol. 54 (2020).
- 10 Voronova N.A, Kupchishin A.I, Niyazov M.N, Taipova BG, Abdukhairova A.T. "Research of electron irradiation effects upon plexiglas strain during bending test." *IOP Conf. Series: Materials Science and Engineering*, Vol.289 (2018):1.

---

## Contents

Editorial.....	3
Peyman Givi	
Computational turbulent combustion in the age of artificial intelligence and quantum information .....	4
S. Jayaraj , A. James, M. Srinivas and M. Mohanraj	
Energy-Efficient Operation of PV-T Solar Collectors with Heat Pump based Water Heaters Suitable for Domestic Applications .....	12
B. Elma, E. Misirli	
On the physical behaviours of the conformable fractional modified Camassa – Holm equation using two efficient methods.....	19
M.K. Dauylbayev, K.T. Konisbayeva, N.R. Tortbay	
Integral bvp for singularly perturbed system of differential equations.....	25
A.A. Issakhov , A.K. Manapova	
Numerical modeling of air flow inside the human nose cavity .....	34
S.D. Maussumbekova, A. Duysenali	
Numerical simulation of boiling liquid outflows process .....	40
M. Odsuren, G. Khuukhenkhuu, S. Davaa, K .Kato.	
Structure of resonance states in the simple schematic model.....	48
S. A. L. Maftunzada	
Definition of physical parameters of 8 x-class solar flares .....	52
E. Boos, V. Bunichev, G. Nurbakova, N. Habyl, S. Rustembayeva, D. Temirkhanova	
Top-quark physics in hadronic collisions.....	57
Sh.R. Myrzakul, Y.M. Myrzakulov, R. Yechshanova, M. Imankul	
Inflation in modified quantum gravity with a fermion field.....	72
A.S. Kussainov, Y.V. White, M.A. Em, E.T. Myrzabek, E.T. Salavatova, S.T. Zhaldybayev.	
Transition to mammography in the regular computed tomography simulation and reconstruction software .....	78
A.I. Kupchishin, V.M. Lisitsyn, M.N. Niyazov, D.S. Utepova.	
Study of the mechanical properties of industrial plexiglas testing for flat straight bending.....	88